Design, Fabrication, and Characterization of a Neural Probe for Deep Brain Stimulation and Recording

Rean Silke MUSA

Examination Committee:

Prof. Dr. Carmen Bartic	KU Leuven/imec	Chair
Prof. Dr. Gustaaf Borghs	KU Leuven/imec	Promoter
Prof. Dr. Bart Nuttin	KU Leuven	Promoter
Prof. Dr. Peter Lievens	KU Leuven	Assessor
Prof. Dr. Geert Callewaert	KUL Campus Kortrijk/imec	Assessor
Prof. Dr. Liesbet Lagae	KU Leuven/imec	
Prof. Dr. Michele Giugliano	Univ. of Antwerp	

In collaboration with:



Dissertation presented in
partial fulfillment of the
requirements for the degree of
Doctor in Physics

October 2011

© 2011 Katholieke Universiteit Leuven – Faculty of Science
Address, B-3001 Leuven (Belgium)

Alle rechten voorbehouden. Niets uit deze uitgave mag worden vermenigvuldigd en/of openbaar gemaakt worden door middel van druk, fotocopie, microfilm, elektronisch of op welke andere wijze ook zonder voorafgaande schriftelijke toestemming van de uitgever.

All rights reserved. No part of the publication may be reproduced in any form by print, photoprint, microfilm or any other means without written permission from the publisher.

Legal depot number: D/2011/10.705/64
ISBN 978-90-8649-446-0

Acknowledgements

I know, I should wear sackcloth and ashes for not mentioning everybody I had the pleasure to meet and work with the past 4.5 years. But I dearly hope, I'm able to do most of them the honor and pay tribute here.

First, I would like to thank my promoter Prof. Gustaaf Borghs and copromoter Prof. Bart Nuttin for giving me the opportunity to elaborate on such an interesting and outstanding topic and contribute to a highly progressive research field. I am equally indebted to Prof. Carmen Bartic who has been my supervisor at imec and helped me tackle many of the scientific and practical hurdles encountered along the way.

Device processing has been an essential part of this work, and it would not have been possible to deal with the daily cleanroom struggles - especially toward the end of this thesis - if it wasn't for Josine Loo who has become a dear friend over the years. I wish her all the best in her new group. It has furthermore been a great pleasure to work together with Marleen Welkenhuysen. Without her *in vivo* know-how and skills I would have missed out on many insightful and exciting experiments.

And how could I forget Danielle Rand, Dimiter Prodanov, and Alexandru Andrei, whose indispensable support with experiments, setups, processing, and availability for discussions has contributed considerably to the final outcome of this thesis. A big thanks especially to Danielle for proofreading my papers and thesis manuscript. I'd also like to express my gratitude to Wolfgang Eberle, group leader of the Bioelectronic Systems Group at imec, who has always been very eager to push forward the *in vivo* activity and spent much time helping with and solving technical problems. A special thanks to Daire Cott who kept me going with the CNT electrodes, although it was only a side project initially and took us almost two years to get some results. But in the end the neurons liked them and the collaboration has definitively gained momentum.

Once more, I must come back to the cleanroom and all those numerous people who have done a great deal of work to make the probes come true. I'm grateful to Lut Van Acker, Nina Tutunjyan, Geraldine Jamieson, Jurgen Hendrickx, Greet Verbinnen, John Slabbekoorn, Erwin Vandenplas, Danny Frederickx, Ludo Viaene, Johan Genyn, Patrick Laermans, and many, many more who have worked behind the scenes and kept everything going.

My dear friends and colleagues from the Bioelectronic Systems Group, Carolina Mora Lopez, Seon-Ah Chong, Dries Braeken, Roeland Huys, Iryna Benilova, Olga Krylychkina, Thoa Nguyen, Karen Van Keer, Danny Jans, Ashwin Sathyanarayanan, Evelien Micholt, Liesbeth Micholt, and Guillaume Mernier, I thank you all for offering so much of your knowledge and keeping my spirits high.

Looking at the extensive amount of papers I've accumulated over the years (digital, of course), I must not forget to appreciate the help of Karin Schoubben and Greet Vanhoof from the imec library. I can't remember a single time when they couldn't get me a copy.

I'd also like to thank Celso, Sven, Barun, Vasyl, and Gerd for their friendship and for being there for me even when not being there. And, as in every good drama, the great honors are reserved for the end credits, which deservedly go to my dear brother and parents. They are the best!

Silke Musa, Leuven, 19 September 2011.

Samenvatting

Het gebruik van invasieve technologieën om systematisch de elektrische hersenactiviteit te registreren en te moduleren heeft tot een significante vooruitgang in de fundamentele neurowetenschappen en klinische toepassingen geleid. In tegenstelling tot traditionele microwires, bieden microgefabriceerde implantaten (neurale probes) het voordeel van een grote design variatie mogelijkheid. Verder kunnen neurale probes gepersonaliseerd worden om aan specifieke toepassingsgerelateerde vereisten te voldoen met betrekking tot grootte, vorm, en functie. Er is echter nog een aanzienlijke vooruitgang nodig om op een betrouwbare manier zowel registratie- als stimulatiemogelijkheden op eenzelfde probe te realiseren. Daarbij zouden elektrodes met cellulaire of zelfs sub-cellulaire dimensies bidirectionele interactie moeten toelaten met de hersenen op verschillende niveau's van neurale organisatie. Verder zijn er nog substantiële experimentele inspanningen nodig om de factors te identificeren die de efficientie, betrouwbaarheid, en veiligheid bepalen van de implantaten gedurende acuut en chronisch gebruik.

In deze thesis werden twee generaties van Si-gebaseerde probes ontwikkeld met verschillende elektrode materialen (Au en Pt) elektrode configuraties (1D en 2D), en elektrode diameters (2–50 μm). Verder bevatten sommige probe designs ook een grote driehoekige tipelektrode voor stimulatie. De functionaliteit van de passieve probes werd succesvol gevalideerd in vivo in acute proof-of-concept experimenten met geanestheseerde ratten. Er konden betrouwbare registraties gemaakt worden in corticale en diepe hersenstructuren met Pt elektrodes van 50, 25, en 10 μm diameter. Ook stimulatie werd betrouwbaar gedemonstreerd in diepe hersenstructuren met de Pt driehoekige tipelektrode en de 50 μm diameter Pt elektrodes waarbij er een positieve correlatie was met het geobserveerde gedragseffect.

Voor de in vitro karakterisatie van deze probe werd een in vitro multi electrode array gefabriceerd dat diende als een testplatform. Verschillende elektrode materialen (Pt, TiN, IrO_x, en CNTs) en diameters (5–50 μm) werden gekarakteriseerd met betrekking tot hun registratie- en stimulatie-efficientie en onderliggende elektrochemische processen. Om neuronale signalen te kunnen registreren moet de elektochemische elektrodeimpedantie op 1 kHz zo klein mogelijk zijn. Deze vereiste interfereert echter met de vraag naar elektrode miniaturisatie. Met behulp van elektrochemische impedantie spectroscopie in fosfaat gebufferde saline (PBS) werd bepaald dat de CNT elektrodeimpedantie tot 3 grootteordes kleiner is vergeleken met die van Pt, TiN, en IrO_x elektrodes. De lage waardes voor de CNT 5 μm diameter elektrodes (4.8 ± 0.3 kOhm) geven zeer veel belovende vooruitzichten voor toekomstige neurale probes die gebaseerd zijn op subcellulaire of zelfs of submicron elektrode dimensies. Overigens werden de elektrodes ook gekarakteriseerd met cyclische voltammetrie om de charge-storage capacity, wat een maat is voor de hoeveelheid lading dat elk materiaal kan leveren binnen de limieten van hydrolyse. Hier waren ook de CNTs superieur ten opzichte van de andere elektrode materialen

tot 2 grootteordes, waarbij waardes tot 6.6 $\pm$ 0.4 C/cm^2 behaald werden voor de 5 μm diameter elektrodes. Het uitstekende gedrag van CNT elektrodes wordt toegekend aan hun poreuze 3D oppervlak.

De veiligheidslimiet van neural stimulatie wordt gedefineerd als de ladingsdichtheid die kan gegeven worden tijdens stimulatie vooraleer er electrolyse van water optreedt. Er werden tot op heden nog geen geschikte methodes gerapporteerd om de limieten van gasevolutie te identificeren in vitro onder realistische stimulatie condities. In deze thesis hebben we reciprocal chronopotentiometrie gebruikt, wat en elektroanalytische techniek is die onderzoek van individuele elektrodeprocessen toelaat die optreden tijdens stimulatie, in combinatie met een nieuwe coulometrische aanpak om het begin van hydrolyse betrouwbaar te detecteren. Deze coulometrische RDC werd gebruikt bij Pt elektrodes in PBS om de kwalitatieve en kwantitatieve effecten van albumine adsorptie en opgelost zuurstof op de verschillende elektrodeprocessen en het begin van hydrolyse te bestuderen.

Abstract

The use of invasive technologies to systematically record and modulate the electrical brain activity has led to significant advances in basic neuroscience and of clinical applications. Unlike traditional microwires, microfabricated implants (neural probes) offer the advantage of a large design space and can readily be customized to meet application-related requirements in terms of size, shape, and function. Considerable progress is still necessary to reliably establish recording and stimulation functionalities on the same probe. In addition, electrodes of cellular (10–50 μm) and even sub-cellular (<10 μm) dimensions should allow bidirectional interaction with the brain at different levels of neural organization. Major experimental efforts are furthermore required to identify the factors that govern the efficiency, reliability, and safety of the implants during acute and chronic operation.

In this thesis, two Si-based probe generations have been developed with various electrode materials (Au and Pt), electrode configurations (1D and 2D), and electrode diameters (2–50 μm). In addition, some of the probe designs also included a large triangular tip electrode for stimulation. The performance of the passive devices was successfully validated *in vivo* in acute proof-of-concept experiments involving anaesthetized rats. Single-unit recordings of spontaneous activity in cortical and deep brain areas could be obtained with Pt electrodes of 50, 25, and 10 μm diameter. Reliable stimulation was demonstrated in deep brain areas using the Pt-based triangular tip electrode and 50 μm diameter Pt electrodes and was positively correlated to observed behavioral responses.

For *in vitro* electrode characterization purposes, a multi electrode array was fabricated serving as a test platform. Various electrode materials (Pt, TiN, IrO_x, and CNTs) and diameters (5–50 μm) were characterized in terms of their recording and stimulation efficacy and in terms of the underlying electrochemical processes. In order to effectively record the minute neural signals, the electrochemical electrode impedance at 1 kHz must be as small as possible. This requirement, however, interferes with the demand for electrode miniaturization. By performing electrochemical impedance spectroscopy in phosphate buffered saline (PBS) it was determined that the CNT electrode impedance at 1 kHz is up to 3 orders of magnitude smaller compared to that of the Pt, TiN, and IrO_x electrodes. Values as low as 4.8 $\pm$ 0.3 kOhm for the 5 μm diameter CNT electrodes present highly promising prospects for future neural probes based on sub-cellular and possibly even sub-micron electrode dimensions.

The electrodes were furthermore characterized by cyclic voltammetry to determine the charge-storage capacity, which is a measure for the amount of charge an electrode can supply within the limits of hydrolysis. Also here, the CNTs outperformed the other electrode materials by up to 2 orders of magnitude, reaching values as high as

$6.6 \pm 0.4\,\mathrm{C/cm^2}$ for the $5\,\mu$m diameter electrodes. The outstanding charge-storage capability of the CNT electrodes was attributed to their highly distributed surface area and hence double-layer capacitance and the presence of electroactive functional groups.

The safe operational limit of neural stimulation is defined as the charge density that can be applied during stimulation before the onset of water electrolysis. Appropriate *in situ* experimental techniques to specifically detect the occurrence of gas evolution under realistic stimulation conditions are not available to date. In this thesis, a new promising electrochemical approach has been developed. It is based on the combination of reciprocal derivative chronopotentiometry (RDC), an analytical tool that provides qualitative information about the individual electrode processes occurring under stimulation, with a new coulometric approach allowing the reliable detection of gas evolution. This new method termed *coulometric RDC* was applied to Pt electrodes in PBS to study the qualitative and quantitative effects of albumin adsorption and dissolved O_2 on the different electrode processes and on the onset of hydrolysis.

Publication List - Journal & Conference Papers

Silke Musa, Daniele R. Rand, Carmen Bartic, Wolfgang Eberle, Bart Nuttin, Gustaaf Borghs. Coulometric detection of irreversible electrochemical reactions occurring at Pt microelectrodes used for neural stimulation. 2011. *Anal. Chem.*, **83**, 4012–4022.

Silke Musa, Daire, Cott, Josine Loo, Daniele R. Rand, Carmen Bartic, Wolfgang Eberle, Bart Nuttin, Gustaaf Borghs. Carbon nanotube electrodes of subcellular dimensions with Parylene C encasement for implantable neural microsystems. 2011. *ACS Nano*, (revision submitted).

Silke Musa, Dimiter Prodanov, Josine Loo, Wolfgang Eberle, Carmen Bartic, Bart Nuttin, Gustaaf Borghs. Using reciprocal derivative chronopotentiometry as a technique to determine safe charge injection limits of electrodes used for neural stimulation. 2010. *Proc. IEEE EMBS*, 2943–6. (Presented at the Int. Conf. IEEE EMBS, Buenos Aires, Argentina).

Silke Musa, Marleen Welkenhuysen, Dimiter Prodanov , Wolfgang Eberle, Carmen Bartic, Bart Nuttin, Gustaaf Borghs. In vitro and in vivo electrochemical characterization of a microfabricated neural probe. 2009. *Proc. IEEE EMBS*, 7143–6. (Presented at the Int. Conf. IEEE EMBS, Minneapolis, USA).

Silke Musa, Marleen Welkenhuysen, Roeland Huys, Wolfgang Eberle, Kris van Kuyck, Carmen Bartic, Bart Nuttin, Gustaaf Borghs. Planar 2D-array neural probe for deep brain stimulation and recording (DBSR). 2008. *Proc. IFMBE*, **22**, 2421–5. (Presented at the Int. Conf. IFMBE, Munich, Germany).

Carolina M. Lopez, **Silke Musa**, Carmen Bartic, Robert Puers, George Gielen, Wolfgang Eberle. Systematic design of a programmable low-noise CMOS neural interface for cell activity recording. 2011. *Proc. DATE*, 1–6.

Willyan Hasenkamp Carreira, **Silke Musa**, Andrei Alexandru, Wolfgang Eberle, Carmen Bartic. Electrodeposition and characterization of iridium oxide as electrode material for neural recording and stimulation. 2009. *Proc. IFMBE*, **25**, 472–5. (Presented at the Int. Conf. IFMBE, Munich, Germany).

Dimiter Prodanov, **Silke Musa**, Marleen Welkenhuysen, Wolfgang Eberle, Carmen Bartic, Gustaaf Borghs, Bart Nuttin. Evaluation of planar micro-fabricated multi-electrode arrays for neuronal recording in vivo. 2009. *Proc. IFMBE*, **25**, 239–24.

Meng Deng, Xi Yang, **Silke Musa**, Weiming Qiu, Mingsheng Xiu, Gustaaf Borghs, Hongzheng Chen. Electrochemical deposition of polypyrrole/graphene oxide composite on microelectrodes towards tuning the electrochemical properties of neural probes. 2011. *Sens. Act. B*, **158**, 176–184.

Thoa Nguyen, Dries Braeken, **Silke Musa**, Olga Krylychkina, Carmen Bartic,

George Gielen, Wolfgang Eberle. Towards a closed-loop system for stimulation and recording: an in vitro approach with embryonic cardiomyocytes. 2010. *Proc. IEEE EMBS*, 2735–8.(Presented at the Int. Conf. IEEE EMBC, Buenos Aires, Argentina)

Wolfgang Eberle, Ashwin Sathyanarayanan Mecheri, **Silke Musa**, George Gielen, Gustaaf Borghs, Carmen Bartic. FEM-based investigation of spatial stimulation properties of a multi-electrode probe with micrometer-size electrodes for cortical and DBS applications. 2009. *Proc. IFMBE*, **25**, 154–7.

Ivan Gligorijevic, Marleen Welkenhuysen, Dimiter Prodanov, **Silke Musa**, Bart Nuttin, Wólfgang Eberle, Carmen Bartic, Sabine Van Huffel. Neural signal analysis and artifact removal in single and multi-channel in vivo deep brain recordings. 2009. *Proc. IEEE EMBS Benelux*, 79–82.

Conference Contributions - Abstracts & Posters

Danielle R. Rand, **Silke Musa**, Wolfgang Eberle. Electrodeposited iridium oxide electrodes for the detection of glutamate in vitro. 2011. *MRS Spring Meeting*, San Francisco, CA USA.

Marleen Welkenhuysen, **Silke Musa**, Roeland Huys, Wolfgang Eberle, Carmen Bartic, Gustaaf Borghs, Bart Nuttin. Planar 2D-array neural probe for deep brain stimulation and single-cell recording: in vivo proof of concept. 2008. *Congr. Europ. Soc. Stereotactic Funct. Neurosurg.*, Rimini, Italy.

Dimiter Prodanov, Marleen Welkenhuysen, **Silke Musa**, Uwe Himmelreich, Bart Nuttin, Gustaaf Borghs, Carmen Bartic. MRI compatibility of chronically implanted microfabricated neural probe:first results. 2009. *Belg. Neurol. Soc. Meeting*, Liège, Belgium.

Bart Nuttin, Carmen Bartic, Marleen Welkenhuysen, **Silke Musa**, Wolfgang Eberle, Kris van Kuyck, Laura Luyten, Dimiter Prodanov, Ivan Gligorijevic, Sabine Van Huffel, John Das, L. Gabriels, J. Kruth, Kris Verstreken, Gustaaf Borghs. Concept of bridging the lesion cavity wall with stimulating and recording devices in the central nervous system. 2010. *Congr. Europ. Soc. Stereotactic Funct. Neurosurg.*, Athens, Greece.

Contents

Contents ix

List of Figures xiii

List of Tables xix

Glossary xxi

List of Symbols xxv

1 Introduction 1

1.1 Motivation 1

1.2 Technologies for CNS Implants 3

1.2.1 Neural Probes 3

1.2.2 Deep-Brain Stimulation 4

1.2.3 Challenges 6

1.3 Overview of this Thesis 6

2 Physico-Chemical Aspects of Electrical Recording and Stimulation 9

2.1 Introduction 9

2.2 Extracellular Sensing of Neural Potentials 9

2.2.1 Thermodynamics of the Electrode-Electrolyte Interface . . 10

2.2.2 Models of the Electrochemical Double Layer 12
2.2.3 The Electrochemical Cell (I) 15
2.3 Electrochemistry of Stimulation 16
2.3.1 Faradaic Charge-Transfer 17
2.3.2 Reversible and Irreversible Reactions 19
2.3.3 The Electrochemical Cell (II) 22
2.3.4 Practical Aspects of Neural Stimulation 23
2.4 Selection Criteria for Electrode Materials 25
2.4.1 Biocompatibility 25
2.4.2 Recording Efficacy 27
2.4.3 Stimulation Efficacy 30
2.5 Summary 33

3 Design, Fabrication, and Packaging of Neural Probes and of an *In Vitro* Test Platform 35

3.1 Introduction 35
3.2 Design Aspects 36
3.2.1 First Generation Probe 36
3.2.2 Second Generation Probe 38
3.3 Fabrication 40
3.3.1 First Generation Probe 40
3.3.2 Second Generation Probe 41
3.3.3 *In Vitro* Test Chip 42
3.4 Probe Packaging 46
3.5 Summary 47

4 Electrochemical Characterization of Electrodes 49

4.1 Introduction 49
4.2 Cyclic Voltammetry 50

4.2.1 Background 50
4.2.2 Materials and Methods 51
4.2.3 Results and Discussion 52
4.2.4 Summary 60
4.3 Electrochemical Impedance Spectroscopy (EIS) 61
4.3.1 Background 61
4.3.2 Materials and Methods 64
4.3.3 Results and Discussion 64
4.3.4 Summary 70
4.4 Coulometric Reciprocal Derivative Chronopotentiometry (RDC) of Pt Electrodes 70
4.4.1 Background 70
4.4.2 Materials and Methods 75
4.4.3 Results 76
4.4.4 Applying RDC to other Electrode Materials 86
4.4.5 Summary 90

5 Acute *In Vivo* Performance of Neural Probes and Biocompatibility Aspects 93

5.1 Extracellular Neural Recording and Stimulation 93
5.1.1 Introduction 93
5.1.2 Materials and Methods 94
5.1.3 Results and Discussion 96
5.2 *In vivo* Electrochemical Characterization 99
5.2.1 Introduction 99
5.2.2 Materials and Methods 100
5.2.3 Results and Discussion 101
5.3 Biocompatibility Aspects 104
5.3.1 Introduction 104

5.3.2 Materials and Methods 105
5.3.3 Results and Discussion 105
5.4 Summary 106

Final Remarks & Outlook **109**

A Contact Angle and Fourier Transform Infrared Analysis of CNTs **113**

B Potentiodynamic Electrochemical Impedance Spectroscopy of IrO_x **117**

C Supporting Information to Section 4.4.3 **123**

D Lithography protocols **129**

Bibliography **131**

Curriculum Vitae **157**

List of Figures

1.1 (a) Multi-shank Si-probe (NeuroNexus, USA), (b) 3D assembly of a multi-shank probe with integrated CMOS, (c) multielectrode *Utah* array, (d, e) optrodes. 4

2.1 Stern model of the electrochemical double layer. 15

2.2 Magnitude of the exchange current density, i_0, for H_2 evolution at different metals 21

2.3 (a, b) Place-exchange mechanism of initially electrosorbed OH^- during anodic oxidation of Pt. (c) Hysteresis-like behavior of the kinetically irreversible formation and reduction of a Pt oxide film. 22

2.4 Schematic of the various chemically irreversible faradaic electrode processes that may damage the electrode and tissue during neural stimulation. 22

2.5 Equivalent circuit representation of a 3-electrode electrochemical cell comprising the working electrode (WE), reference electrode (RE), and counter electrode (CE). 23

2.6 Pulse shapes used for neural stimulation. 25

2.7 Toxicity results from *in vivo* corrosion experiments for various metals and for practical alloys. 27

2.8 (a) Literature survey of electrode impedances at 1 kHz vs. geometric electrode area for various materials. (b) Examples of electrode materials with a large surface roughness. 30

2.9 Basic principle of cyclic voltammetry. 31

3.1 Design layouts of the first generation probe. 37

3.2 Design layouts of the second generation probe. 39

3.3 Process flow of the first generation probe with Ni/Au electrodes. . 41

3.4 First generation probe after: (a) First Au lift-off, (b) electrode opening by reactive ion etching, (c) electroless Ni plating, (d) second Au lift-off, (e) wafer debonding. (f) Side view SEM of the probe tip. 41

3.5 Process flow of the second generation probe with Pt electrodes. . . 42

3.6 (a) Overview SEM image of a second generation probe with a total thickness of approx. 50 μm. (b–d) Close-up SEMs of the probe tip. 43

3.7 Process flow for the test chip containing Pt, TiN, and CNT electrodes. 44

3.8 Processed test chips with CNT electrodes. 45

3.9 AFM images of (a) as deposited TiN and (b) H_2SO_4-treated TiN. (c) Optical image of an electrode after IrO_x deposition (top-right). (d) SEM image of a TiN sample after IrO_x electrodeposition; the indicated layers are (from top to bottom): IrO_x (159 nm), TiN (353 nm), SiO_2 (250 nm). 46

3.10 Packaged first generation probe (right) and second generation probe (left). 47

4.1 serum albumin carrying a net negative charge at neutral pH. . . . 51

4.2 Typical cyclic voltammograms obtained with (a) 50 μm diameter Pt electrodes (test chip and probe), (b) a 50 μm diameter TiN electrode, (c) a 50 μm diameter IrO_x electrode immediately after the anodic deposition, and (d) with 5 μm diameter TiN and CNT electrodes. . 52

4.3 Crack formation in an anodically deposition IrO_x film stored for 3 months in a N_2 dry box and subjected to CV in PBS. 56

4.4 Dependence of the normalized charge densities, q_{csc}^{50} and q_{csc}^{25} (inset), on the geometric area of the Pt, TiN, and CNT electrodes, and theoretical behavior of a microelectrode. 58

4.5 Comparison of CVs measured with a 50 μm diameter Pt electrode in phosphate buffered saline (PBS) and PBS complemented with bovine serum albumin (PBS-BSA) at 0.1 V/s. 59

4.6 Comparison of CVs measured with 50 μm diameter Pt electrodes in phosphate buffered saline (PBS) at ambient conditions and in PBS deoxygenated by continuous N_2 purging (PBS_{deox}) at (a) 0.1 V/s and (b) 2 V/s. 60

4.7 Equivalent circuit representing the various interfacial processes contributing to the small-signal ac electrode polarization. 62

4.8 Average Bode plots showing the impedance magnitude, $|Z|$, and phase angle, θ, obtained for the Pt, TiN, IrO_x, and CNT electrodes of 50, 25, 10, and 5 μm diameter measured between 1–10^5 Hz in PBS. 65

4.9 Impedance magnitude, $|Z|$, at 1 kHz vs. the geometric electrode area for the Pt, TiN, IrO_x, and CNT electrodes of 50, 25, 10, and 5 μm diameter obtained in this work in comparison to values reported in literature. 66

4.10 Average Bode plots for Pt electrodes of 50 μm diameter measured between 1 – 10^5 Hz in PBS and PBS-BSA. 69

4.11 Theoretical $E(t)$ transients of a reversible redox system in response to (a) anodic (oxidation) and (b) cathodic (reduction) current densities of equal magnitude. 73

4.12 (a) Typical voltage transient, $E(t)$, of a Pt electrode measured in response to a biphasic, symmetric current pulse. (b) Corresponding reciprocal derivative of the voltage transient. 73

4.13 (a) Typical voltammogram of a 50 μm diameter Pt electrode measured in PBS at 0.1 V/s. Indicated are the corresponding cathodic (C) and anodic (A) states (CCAS). (b) $dt/dE(E)$ plot with CCAS obtained with a Pt electrode in response to a biphasic current pulse. (c) Corresponding voltage transient, $E(t)$, and current pulse, $i(t)$, with applied charge density, q_0. Indicated are the cathodic and anodic charge densities, q_C and q_A, respectively, consumed between the two CCAS. 75

4.14 Series of $dt/dE(E)$ plots obtained in response to constant pulse amplitude (CPA) stimulation of a 50 μm diameter Pt electrode in PBS and PBS-BSA. 77

4.15 Series of $dt/dE(E)$ plots obtained in response to constant pulse amplitude (CPA) stimulation of a 50 μm diameter Pt electrode in PBS and PBS_{deox}. 80

4.16 (a, c, e, g) Consumed charge densities, q_C and q_A, vs. applied charge density, q_0, for cathodic-first (CF) and anodic-first (AF) stimulation with a constant pulse width (CPW) and amplitude (CPA) in PBS and PBS-BSA. (b, d, f, h) Corresponding normalized charge densities, q_C^0 and q_A^0. 82

4.17 (a, c, e, g) Consumed charge densities, q_C and q_A, vs. applied charge density, q_0, for cathodic-first (CF) and anodic-first (AF) stimulation with a constant pulse width (CPW) and amplitude (CPA) in PBS and PBS_{deox}. (b, d, f, h) Corresponding normalized charge densities, q_C^0 and q_A^0. 83

4.18 Series of $dt/dE(E)$ plots obtained with a (a) 50 μm diameter TiN electrode and (b) 25 μm diameter CNT electrode in PBS with cathodic-first (CF) stimulation at a constant pulse width (CPW). . 87

4.19 Series of $E(t)$ transients recorded in PBS with a (a) 50 μm diameter TiN electrode and (b) 25 μm diameter CNT electrode in response to cathodic-first stimulation at a constant pulse width of 400 μs. . . . 87

4.20 Absolute cathodic and anodic electrode polarizations, E_{pol}^C and E_{pol}^A, respectively, for a (a) 50 μm diameter TiN and (c) 25 μm diameter CNT electrode obtained in response to cathodic-first stimulation of increasing charge density, q_0, with a constant pulse width of 400 μs in PBS. Series resistance, R_s, of the (b) 50 μm diameter TiN and (d) 25 μm diameter CNT electrode. 88

5.1 Examples of spontaneous neural activity recorded with 1G probes containing 50 μm diameter Au and Pt electrodes in the motor cortex, and with 2G probes containing Pt electrodes of 50, 25, and 10 μm diameter in the hippocampus. All data is shown as recorded. . . . 98

5.2 (a) Miniature reference electrode (μ-RE). (b) Front and (c) side view of an assembly consisting of a 2G probe with 3 μ-REs fixed to a probe holder. (d) Implanted probe-μRE assembly. 101

5.3 Comparison of CVs measured with 50 μm diameter Pt electrodes *in vivo* (2G probe), and in PBS and PBS-BSA (test chip; cf. Fig. 4.5) at 0.1 V/s. 102

5.4 Average Bode plots for Pt electrodes of 50 μm diameter measured between 1–10^5 Hz in PBS (test chip) and *in vivo* (2G probe). . . . 103

5.5 Series of $dt/dE(E)$ plots obtained with 50 μm diameter Pt electrodes *in vivo* (2G probe) and in PBS (test chip) with CF-CPW stimulation. (a) Cathodic phase, (b) anodic phase. Only a selection of all applied (absolute) charge densities, q_0, is shown. Graphs are stacked by a constant offset. Regions of Pt-specific reactivity (as identified in PBS) are indicated by horizontal arrows. Long vertical arrows point in the direction of increasing q_0. 104

5.6 Scanning electron micrographs of primary rat hippocampal neurons after 5 days *in vitro* on fabricated CNT substrates. 106

A.1 Basline-corrected transmittance infrared spectra of (a) as-grown CNTs, (b) SiO_2-coated CNTs after BHF treatment, and (c) CNTs after BHF treatment. The corresponding contact angles for the three substrates are shown on the right-hand side. 114

B.1 Potentiodynamic behavior of the equivalent circuit elements determined for an IrO_x electrode. 120

B.2 Mott-Schottky plot, $1/T_{CPE}^2$ vs. E, and voltammetric i vs. E response of an IrO_x electrode. 120

C.1 Series of $dt/dE(E)$ plots obtained in response to constant-pulse-width (CPW) stimulation of a 50 μm diameter Pt electrode in PBS and PBS-BSA. 124

C.2 Series of $dt/dE(E)$ plots obtained in response to constant-pulse-width (CPW) stimulation of a 50 μm diameter Pt electrode in PBS and PBS_{deox}. 125

C.3 Series of $dt/dE(E)$ plots obtained in response to anodic-first (AF) stimulation of 50 μm diameter Pt electrodes in PBS with 0.15 and 0.3 M NaCl. 126

C.4 Normalized charge densities for reciprocal derivative chronopotentiometry with anodic-first (AF) stimulation using either a constant pulse width (CPW) or amplitude (CPA) in PBS of (a) 0.15 M NaCl and (b) 0.30 M NaCl. 127

C.5 Absolute cathodic and anodic electrode polarizations, E_{pol}^C and E_{pol}^A, respectively, obtained in PBS and PBS-BSA for a range of applied charge densities, q_0, and stimulation conditions. 128

List of Tables

2.1 Classified *in vivo* neural biocompatibility of various implant materials. 26

2.2 Literature survey of charge-storage capacities, q_{csc}, and charge-injection capacities, q_{cic}, of different electrode materials. 32

3.1 Design specifications of the first and second generation neural probes. 38

4.1 Concentrations and isoelectric points of the three most common proteins in the human cerebrospinal fluid (CSF) and blood serum. 51

4.2 Average values for the cathodic q_{csc}, q_{csc}^{25}, q_{csc}^{50}, and water window for the Pt, TiN, IrOx, and CNT electrodes. 57

4.3 Average fitting parameters of the impedance spectra recorded with the Pt, TiN, IrOx, and CNT electrodes of 50, 25, 10, and 5 μm diameter. 67

4.4 Average fitting parameters of the impedance spectra recorded with 50 μm diameter Pt electrodes in PBS and PBS-BSA. 70

4.5 Average charge densities at the onset of chemically irreversible gas evolution. 85

5.1 Average stimulation thresholds determined with the second generation probes in 4 *in vivo* experiments. 97

5.2 Average fitting parameters (mean±sd) of the impedance spectra recorded *in vivo* using 2G probes with 50 μm diameter electrodes. . 103

Glossary

AF anodic-first

AO albumin oxidation

BHF buffered hydrofluoric acid

BSA bovine serum albumin

CCAS corresponding cathodic and anodic states

CDI capacitive deionization

CE counter electrode

CF cathodic-first

CNS central nervous system

CPA constant pulse amplitude

CPE constant phase element

CPW constant pulse width

CSF cerebrospinal fluid

CV cyclic voltammetry

CVD chemical vapor deposition

DBS deep brain stimulation

DRIE deep reactive ion etching

EDL electrochemical double layer

EEG electroencephalography

EF extracellular fluid

EIS electrochemical impedance spectroscopy

FIB focussed ion beam

fMRI functional magnetic resonance imaging

FTIR Fourier-transform infrared spectroscopy

H2E H_2 evolution

H2O H_2 oxidation

HA H adsorption

HD H desorption

IHP inner Helmholtz plane

ip intraperitoneally

IPA isopropyl alcohol

NLSF nonlinear least squares fitting

O2E O_2 evolution

O2R O_2 reduction

OCD obsessive compulsive disorder

OCP open-circuit potential

OHP outer Helmholtz plane

OR Pt oxide reduction

PBS phosphate buffered saline

PBS_{deox} deoxygenated phosphate buffered saline

PBS-BSA phosphate buffered saline supplemented with bovine serum albumin

PD Pt dissolution

PECVD plasma-enhanced chemical vapor deposition

PHD phosphate deprotonation

PHP phosphate protonation

PO Pt oxidation

R-PD redeposition of dissolved Pt

RDC reciprocal derivative chronopotentiometry

RE reference electrode

RIE reactive ion etching

rms root-mean-square

sc subcutaneously

SEM scanning electron microscopy

SHE standard hydrogen electrode

SNR signal-to-noise ratio

VTA ventral tegmental area

WE working electrode

List of Symbols

a thermodynamic activity (mol/l)

α exponent of the constant-phase element impedance

$\mathcal{A}$ electrode area (cm^2)

β transfer coefficient

C_H^0 Helmholtz capacitance (per unit area) (F/cm^2)

C_{dl}^0 double layer capacitance (per unit area) (F/cm^2)

C_{dl} double layer capacitance (F)

C_d^0 diffuse Gouy-Chapman capacitance (per unit area) (F/cm^2)

C_{sc}^0 space-charge capacitance (per unit area) (F/cm^2)

c^* bulk molar concentration (mol/l)

c molar concentration (mol/l)

D diffusion coefficient (cm^2/s)

e_0 elementary charge ($1.602 \cdot 10^{19}$ C)

E_{fb} flatband potential (V)

E_{pzc} potential of zero charge (V)

E relative electrode potential (V)

ϵ_0 permittivity in vacuum ($8.854{\cdot}10^{-12}$ F/m)

ϵ_∞ high-frequency limit of the relative permittivity

ϵ_r relative (static) permittivity

η overpotential (V)

F Faraday constant (96485 C/mol)

G specific (molar) Gibbs free energy (kJ/mol)

h electrode recess height (cm)

i_0 exchange current density (A/cm^2)

i_f faradaic current density (A/cm^2)

i_l diffusion-limited current density (A/cm^2)

j imaginary number

k_B Boltzmann constant ($1.381 \cdot 10^{23}$ J/K)

k_H Henry's (empirical) constant for gas solubility $(atm(mol/l)^{-1})$

κ Debye inverse length (cm^{-1})

λ_D Debye length (cm)

l pore length (cm)

μ chemical potential (kJ/mol)

$\tilde{\mu}$ electrochemical potential (kJ/mol)

μ_i^0 standard chemical potential (kJ/mol)

N^0 bulk ion concentration (cm^{-3})

N_D donor concentration (cm^{-3})

N_a anion concentration (cm^{-3})

N_c cation concentration (cm^{-3})

n_e number of measured electrodes

n_p number of pores

n number of moles (mol)

ω angular frequency (rad)

ϕ Galvani or inner potential (V)

p gas pressure (atm)

ψ Volta or outer potential (V)

q_{cic} charge injection capacity (C/cm^2)

q_{csc} charge storage capacity (C/cm^2)

R gas constant (8.314472 J/(mol K))

r_e electrode radius (cm)

r_p pore radius (cm)

R_{ct} charge-transfer resistance (Ohm)

R_s series resistance (Ohm)

ρ space-charge density (C/cm^3)

ϱ resistivity (Ω cm)

σ_W mass-transfer coefficient (cm/s)

σ surface charge density (C/cm^2)

χ surface potential (V)

T_{CPE} magnitude of the constant phase element impedance (Ohm)

T_W magnitude of the Warburg impedance (Ohm)

t time (s)

τ_0 mean (dielectric) relaxation time (s)

τ electrochemical transition time (s)

T absolute temperature (K)

θ phase angle (°)

Z'' imaginary part of the impedance (reactance) (Ohm)

$|Z|$ impedance modulus (Ohm)

Z' real part of the impedance (resistance) (Ohm)

Z complex impedance (Ohm)

z charge number

ζ zeta potential (V)

Chapter 1

Introduction

1.1 Motivation

The rationale behind developing new technologies to interact and interface with the central nervous system (CNS) has always been twofold: understanding the brain from a systems neuroscience point of view and developing therapeutic approaches to treat neurological disorders and deficits, which cause functional impairment of the sensory, motor, and cognitive system. Fundamental neuroscience requires interface technologies where the primary functionalities include the electrical and neurochemical monitoring of brain activity and/or stimulation of discrete neurons or neuronal populations at requisite spatial resolutions for a specific period of time. For clinical applications and translational research, additional demands for safety, long-term reliability and stability, patient acceptance, usability, and cost effectiveness must be met.

The advent and thrive of innovative device solutions has always been the consequence of synergies between application-driven requirements and technological advances. So was the first Si-based neural implant of Wise et al. [1] developed in the 1970s, a decade marked amongst others by Hoff's microprocessor and the first PCs. Rapid developments in the field of microelectronics prompted many scientists to develop novel research instruments to aid in the detection, processing, and interpretation of scientific data. Today, most neural implants still share many of the original ideas, but technological and scientific progress in terms of design, materials, components, and experimental approaches have greatly contributed to establish more efficient and customized neural interfaces.

Unlike traditional micromachined microwires, microfabricated electrode arrays (neural probes) can readily be customized to meet specific application-related

requirements in terms of size, shape, and function. Three principal function-design relations can be identified [2]: (1) the spatiotemporal resolution of recording (at the level of synaptic currents, single units, or field potentials) and stimulation (of discrete neurons or neuronal populations); here, the design space is determined by the electrode size, density, and configuration; (2) the invasiveness of the devices, which is a function of the device structure and geometry; (3) the functional lifetime of the device, which is again determined by its structure but also material composition.

The use of neural probes to reliably monitor electrical brain activity at different levels of neural organization over long periods of time has been a long standing goal in the field of neuroscience. Over the past three decades, the recording capability of neural probes implanted in animals has significantly improved. Various studies have reported recordings of field potentials as well as single and multi-unit activity from tens to hundreds of neurons simultaneously over several months using electrodes down to cellular dimensions (10–50 μm) [3–14]. Such remarkable results have been achieved due to scientific advances in the basic understanding of the electrode-tissue interface [15–18], due to technological advances in terms of probe architectures [19] and electrode materials [20–22], and due to new approaches to minimize tissue damage and chronic inflammatory tissue responses [23–25]. Considerable efforts are underway to further enhance the spatial resolution and capacity of neural recording by employing even smaller electrodes of sub-cellular dimensions ($< 10\,\mu$m) arranged in denser arrays. High-resolution mapping of brain activity may help decipher how the spatial organization and connectivity of populations of neurons encode sensory perception, memory, and behavior.

Similarly, neural stimulation with high-density electrode arrays is expected to improve the spatial confinement of neural activation/inhibition patterns. The latter is in particular desired for applications involving deep brain stimulation (DBS). Deep brain stimulation has shown remarkable therapeutic benefits for patients with otherwise medically refractory movement and psychiatric disorders, including essential tremor, Parkinson's disease, and obsessive compulsive disorder (OCD) [26,27]. In addition to its clinical benefit, DBS can also provide new insights into fundamental brain functions through direct manipulation of both local and distributed brain networks in various animal models [28,29]. Combining both recording and stimulation functionalities on one platform would offer the possibility to map spatiotemporal patterns of DBS-induced activity and thus help unravel the fundamental mechanisms of brain functions.

Unlike high-density neural recording, stimulation has not yet reliably been implemented in neural probes. The reason is that electrode materials currently employed for neural recording are incapable of delivering sufficient charge to safely activate neural tissue at a cellular or even sub-cellular scale. The electrodes would corrode instantaneously. One remedy to this shortcoming is either to abandon small electrode dimensions and employ electrodes that are large enough to sustain

the necessary stimulation currents, or to develop more efficient electrode materials, which can be used both for recording and stimulation. Clearly, the latter offers more opportunities for future probe technologies.

1.2 Technologies for CNS Implants

1.2.1 Neural Probes

Microfabricated neural probes are gradually becoming the workhorses of neurophysiology labs all around the world. Although not obsolete, traditional microwire electrodes having only one tip electrode are limited in their capability for multi-site recording and stimulation. Most neural probes are Si-based and follow similar design rules. The archetype, the *Michigan probe* or *array* based on thin-film technology, is displayed in Fig. 1.1a and b. Basically, interconnects, electrode sites, and bond-pads are patterned lithographically and insulated using appropriate dielectrics. The outline and thickness of the probes are defined using either a wet etch in combination with a diffused-boron etch-stop layer [30] or deep reactive ion etching (DRIE) of silicon-on-insulator wafers [31,32]. A multitude of variations of this design have been devised to address issues of minimal tissue damage [33], drug delivery [34,35], 3D microassembly [36,37], and CMOS integration [36,38]. A broad range of *Michigan* type probes is commercially available (Neuronexus, USA) for research purposes with shaft lengths ranging from 2–15 mm, a shaft thickness of 15 μm, Ir electrode sites of 100 μm^2 and larger, and 1–8 parallel shanks with at least 8 electrodes per shank.

Another original probe type is the so-called *Utah array* (Fig. 1.1c) (commercially distributed by Blackrock, USA) consisting of a 10×10 fakir bed-like array of needles each having a single recording site at the tip. For this device, a microsaw is used to cut checkerboard slices through a 4×4 mm^2 block of monocrystalline Si [39]. Additional processing steps involve etching, metallization, and insulation. The final array has a recording site at the tip of each 1.0–1.5 mm long shank with its interconnect running down the shank and through the back of the block, where the bond pads are located. This device configuration was the first Si-based multielectrode array to be implanted in the motor cortex of a tetraplegic human in 2006 allowing the control of a prosthetic hand based on neural feedback [40]. Such brain-computer interfaces may one day provide paralyzed patients with a means to fully interact with the outside world.

In recent years, optical stimulation of genetically modified neurons expressing light-sensitive ion-channels (channelrhodopsin ChR1, ChR2, or VChR1) has emerged as a new landmark approach to interact with neurons and promises to be one of the major developments in the field of systems neuroscience [41]. *In vivo* photomodulation

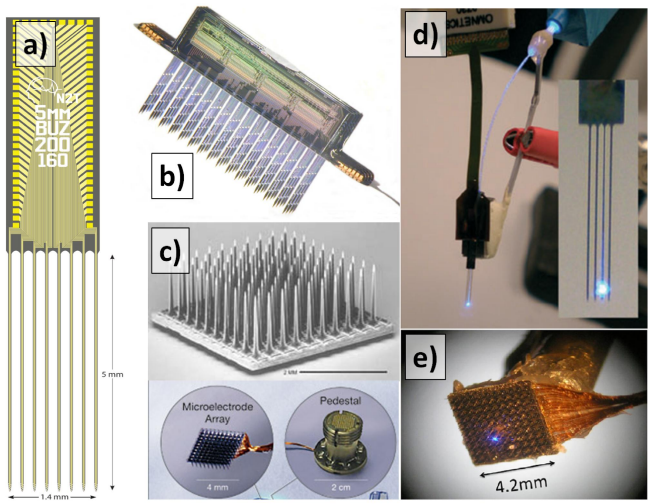

Fig. 1.1: (a) Multi-shank Si-probe (NeuroNexus, USA), (b) 3D assembly of a multi-shank probe with integrated CMOS, (c) multielectrode *Utah* array, (d, e) optrodes.

of behavior and neural activity in anaesthetized rats [?], freely moving mice [42], and awake non-human primates [43] were demonstrated using implanted optical fibres. Further efforts to improve the optical interface have resulted in so-called optrodes, which are ordinary *Michigan* or *Utah* type probes equipped with an optical fibre [44,45] (Fig. 1.1d, e) or integrated waveguides [46,47] enabling simultaneous optical stimulation and electrical recording.

1.2.2 Deep-Brain Stimulation

Clinical DBS has become a widespread treatment for various movement disorders, including Parkinson's disease, essential tremor, and dystonia and is also considered for several psychiatric conditions [26,27]. The electrical interface to the brain is established through four 1.5 mm wide annular contacts spaced 0.5 mm apart and wrapped around a polymeric lead 1.27 mm in diameter. The electrodes are connected via robust coiled wire extensions to a titanium-encased programmable, battery-operated pulse generator implanted in the patient's chest (or abdomen) (Medtronic, USA). By selecting individual electrodes, or electrode combinations, stimuli are delivered to target brain regions. However, only a very coarse and imprecise control of the electric field can be achieved with the given electrode configuration resulting in field shifts on the order of 2–3 mm along the lead's axis. Current spread outside intended target regions may occur due to imprecise electrode

placement inducing unwanted stimulation-related side-effects. Another system under regulatory consideration for clinical DBS employs similar electrodes, but the pulse generator is implanted in a skull pocket (NeuroPace, USA). This system is aimed at treating refractory epilepsy and also incorporates recording capabilities for feedback control. The system monitors electrocorticogram signals for evidence of epileptic seizures.

Due to size restrictions, both of these DBS systems are applicable only to humans or at the most non-human primates and allow only limited possibilities to study the cellular mechanisms underlying DBS. Investigating these mechanisms offers potentials beyond the obvious clinical benefit and may help identify the function of particular brain circuits and the relationship between activity in those circuits and behavior. Research that aims at answering such fundamental questions related to clinical applications is termed translational research or *from bench to bedside and back again* and relies on validated animal models. Because many of the general principles of neural processing are preserved across species, data from DBS studies in animals are equally relevant for unraveling the mechanisms of DBS in humans. In order to carry out such translational research, an appropriate (miniaturized) instrumental toolkit is required.

The large majority of DBS animal studies is performed in rodents ($> 90\%$ [29]) and employs custom-made systems consisting of traditional microwire electrodes. Generally, these studies evaluate the efficacy of DBS based on stimulation-induced changes of the physiological and motor performance of the animals. The simultaneous recording of correlated changes of neural activity during DBS is less frequently employed and also relies on microwire electrodes [48,49]. Such experimental setups often suffer from poor reliability and precision because of the limited accuracy in fabrication and surgical placement of the microwire electrodes. In addition, only a limited number of these microwires can be implanted at the same time.

Clearly, there exists a need for microfabricated implants combining both recording and stimulation modalities on one platform with large electrode arrays for a high spatial resolution. A DBS array for non-human primates combining stimulation and recording with 64 electrode sites has recently been introduced [50] (Sapiens, NL). Its design is strongly based on the state-of-the-art clinical DBS lead, but offers a larger electrode density. In contrast, comparable systems allowing simultaneous recording and stimulation in rodents are still lacking. Here, the gap between Si-probes with a proven high-resolution recording capability and traditional microwires enabling stimulation still has to be bridged technologically.

1.2.3 Challenges

The most pressing technical challenge that needs to be met in order to realize a platform for simultaneous DBS and recording in rodents relates to the reliability of the stimulating electrodes. Because high spatial selectivity requires the use of small electrodes, appropriate electrode materials must be employed that can sustain the large currents densities occurring during stimulation. In addition, improved experimental methodologies to accurately characterize electrode materials and advance the fundamental understanding of the electrode-tissue interface will help develop new strategies for longer-lasting electrodes and safe stimulation.

1.3 Overview of this Thesis

The main objectives of this thesis were to design and fabricate a neural probe capable of recording and stimulating deep brain structures in rat brains, to identify electrode materials suitable for the efficient recording and stimulation at cellular and even sub-cellular resolution using appropriate experimental approaches, and to validate the probe performance *in vivo*. The following Chapter 2 describes the physico-chemical basis of the electrode-electrolyte interface as a prerequisite to provide a better understanding of the failure (and success) modes of neural implants. Thermodynamic and kinetic aspects of electrochemical systems are introduced and discussed in the context of the mechanisms that govern neural recording and stimulation. This discussion broadens to more practical implications related to the biocompatibility and recording and stimulation efficacy of common electrode materials.

In Chapter 3, we describe details of the design, fabrication, and packaging of the two probe generations developed in this thesis in order to demonstrate the proof-of-concept of cortical and deep brain stimulation and recording. Additionally, the fabrication of an *in vitro* electrode array is described serving as a test platform for the characterization of various electrode materials and sizes. Chapter 4 is dedicated to the *in vitro* electrochemical characterization of the various electrode materials, Pt, TiN, IrO_x, and CNTs, using well-established methods, including cyclic voltammetry (CV) and electrochemical impedance spectroscopy (EIS), and a new coulometric approach able to reliably detect the onset of gas evolution under stimulation. The results are discussed in terms of the most/least efficacious electrode material and electrode size dependence. With the idea to provide more realistic *in vitro* models of the biochemical environment in the brain, the influence of albumin adsorption and dissolved O_2 on the performance of Pt electrodes is investigated using the aforementioned methods.

Chapter 5 focuses on the *in vivo* evaluation of the neural probes, including neural

recording and stimulation with the two device generations. A custom setup for the *in vivo* electrochemical characterization of the probes is presented. The results are discussed and compared against the *in vitro* data. Additionally, we also address aspects related to the biocompatibility of the probes and employed materials and provide details of the *in vitro* biocompatibility assessment of the microfabricated CNT electrodes. The thesis is concluded with a critical evaluation of the overall utility of the *in vivo* platforms and electrode materials developed herein and discusses future experimental strategies to identify the factors governing the efficacy, reliability, and safety of neural implants.

Chapter 2

Physico-Chemical Aspects of Electrical Recording and Stimulation

2.1 Introduction

This chapter introduces the physico-chemical basis of electrical recording and stimulation of neural tissue with an emphasis on the thermodynamic origin of the electrode-electrolyte interface and electrode potential, and the kinetic theory of charge-transfer. Physical models of the electrode-electrolyte interface are derived. Principles of electrochemical and chemical irreversibility of charge-transfer are presented and discussed in the context of tissue and electrode damage occurring during neural stimulation. General aspects of practical stimulation waveforms are mentioned. Finally, commonly used electrode materials are reviewed in terms of their safety and recording and stimulation efficacy.

2.2 Extracellular Sensing of Neural Potentials

Neural information is conveyed in the form of electr(ochem)ical signals called action potentials. At a single neuron level, action potentials are mediated by ionic fluxes resulting from concentration and potential gradients across neural membranes giving rise to measurable time-varying electric fields. These electric fields can be sensed extracellularly by placing appropriate electrodes into the ionic environment

of the brain. An electrochemical cell is formed, where the signal transduction across the electrode-tissue interface can be described in terms of the structural and electrical characteristics of the interface.

Practically any interface between two unequal phases is subject to polarization phenomena occurring due to anisotropic electrostatic forces operating near the phase boundary. The consequence is the build-up of a space-charge region with a net or excess charge on either side of the boundary. In the case of metals, which have a very high electric conductivity ($0.95 \cdot 10^5\,\mathrm{S/cm}$ for Pt) all electrons are restricted to a surface region about 1 Å thick. The large conductivity is caused both by a high electron concentration ($5.17 \cdot 10^{24}\,\mathrm{cm^{-3}}$ for Pt) and mobility. When immersed into an electrolyte, such as the extracellular fluid (EF) with an ion concentration of about $9.0 \cdot 10^{19}\,\mathrm{cm^{-3}}$ (0.15 mol/l) and a conductivity roughly six orders of magnitude lower than that in metals, two phenomena occur: water dipoles close to the metal surface become oriented, and, assuming the metal surface is negatively charged, the electrolyte close to the metal surface becomes depleted of negative ions (anions) leaving behind a cloud of positive ions (cations), which screen the electric field caused by the excess charge on the metal. The resulting charge distribution - two narrow regions of equal and opposite charge - is known as the electrochemical double layer (EDL). It can be viewed as a capacitor with an extremely small effective plate separation and therefore a very high capacitance. The voltage drop between the metal and the solution is typically on the order of 1 V. Since this potential drop extends over a very narrow region, it creates an extremely high field of up to $10^9\,\mathrm{V/m}$. Such a high field is one of the characteristics of electrochemical interfaces.[51]

2.2.1 Thermodynamics of the Electrode-Electrolyte Interface

The above mechanistic picture can also be described in a more formalistic way based on ordinary thermodynamics. Here, the chemical potential of an uncharged species i, μ_i, is the work required to add a mole of species i to a system at constant pressure, p, and temperature, T, and is defined as:

$$\mu_i \equiv \left(\frac{\partial G}{\partial n_i}\right)_{p,T} \tag{2.1}$$

where G is the Gibbs free energy of the phase under consideration and n_i is the number of moles of species i. For metals, the chemical potential of the electrons is identical to the value of the Fermi energy (relative to the ground state) at $T = 0\,\mathrm{K}$, since any electron added to the system must occupy the Fermi level. The chemical potential is related to the thermodynamic activity, a_i, of species i through:

$$\mu_i = \mu_i^0 + RT \ln a_i \tag{2.2}$$

where μ_i^0 is the standard chemical potential and R is the gas constant. If the particles of species i are charged, one speaks of an electrochemical potential, $\tilde{\mu}_i$, instead, and writes:

$$\tilde{\mu}_i = \mu_i + zF\phi \tag{2.3}$$

where z_i is the charge number of species i, F is the Faraday constant, and ϕ is the inner or Galvani potential of the phase under consideration. It is defined as the work required to bring a unit point charge from infinity to a point inside a phase and corresponds to the electrostatic potential, which is actually experienced by a charged particle inside a phase. In contrast, the so called outer or Volta potential, ψ, describes the work required to bring a unit point charge from infinity to a point just outside the surface of the phase. In practice, that means at a distance of about $10^{-5} - 10^{-3}$ cm from the surface.[51] The outer potential thus is determined purely by the charge residing on the phase. The inner and outer potentials differ by the surface potential, χ,

$$\chi = \phi - \psi \tag{2.4}$$

which is caused by a net preferential orientation of dipoles at the surface.

When two different phases, such as a metal (M) immersed into a solution (S), are in thermodynamic equilibrium with each other, i.e. the second law of thermodynamics applies, the difference in electrochemical potentials of the two phases becomes zero, $\Delta\widetilde{\mu}_{eq} = 0$. Hence, with Eq. 2.3 one obtains

$$\mu_M + z_i F\phi_M = \mu_S + zF\phi_S \tag{2.5}$$

and with $\phi_M - \phi_S = \Delta\phi_{eq}$ and $\mu_M - \mu_S = -\Delta\mu_{eq}$

$$\Delta\phi_{eq} = -\frac{1}{z_i F}\Delta\mu_{eq} \equiv \Delta\chi_{eq} + \Delta\psi_{eq} \tag{2.6}$$

which is nothing less than the expression for a potential difference. Thus, the potential difference at a contact between an electronic and ionic conductor originates from the different charge carrier concentrations on either side of the interface, described by $\Delta\psi_{eq}$, and from dipole layers between the two phases, described by $\Delta\chi_{eq}$. Electroneutrality across the interface requires that the charge on the metal is always equal and opposite to the total charge on the solution side of the interface. Because the ion concentration in solutions is orders of magnitude lower than the charge density in metals, a space-charge region forms on the solution side which entails an excess of (positive or negative) ions. This charge distribution, or EDL, is of key importance for the understanding of signal transduction across the electrode-tissue interface. The spatially confined ionic currents of activated neurons can transiently modify this charge distribution and hence induce measurable extracellular potential changes.

The potential difference, $\Delta\phi_{eq}$ (Eq. 2.6), can be related to the activity of the reacting species on either side of the interface according to Eq. 2.2. Considering the most general case of a reversible electrochemical reaction

$$\mathrm{R} \rightleftharpoons \mathrm{O} + \mathrm{ze}^- \tag{2.7}$$

where R and O are the reduced and oxidized species, respectively, and z is the number of exchanged electrons, thermodynamic equilibrium is described by:

$$\tilde{\mu}_R = \tilde{\mu}_O + \tilde{\mu}_{e^-} \tag{2.8}$$

By using Eqs. 2.3 and 2.2 we obtain

$$\mu_R^0 + RT \ln a_R + z_R F \phi_S = \mu_O^0 + RT \ln a_O + z_O F \phi_S + \mu_{e^-}^0 + RT \ln a_{e^-} + z_{e^-} F \phi_M \tag{2.9}$$

The electrons reside on the metal and are therefore in their standard state with an activity of $a_{e^-} = 1$. Their Galvani potential corresponds to that of the metal, ϕ_M; R and O are in the solution, hence their Galvani potential is ϕ_S. Furthermore, the following relation hold $z_R - z_O = z_{e^-} = -z$, where z is the number of exchanged electrons. After some rearrangements, we obtain the famous Nernst equation

$$\Delta\phi_{eq} = \phi_M - \phi_S = \phi_{eq}^0 + \frac{RT}{zF} \ln \frac{a_O}{a_R} \tag{2.10}$$

where $\phi_{eq}^0 = -(\mu_R^0 - \mu_O^0 - \mu_{e^-}^0)/zF$ is the standard potential difference for $a_O = a_R = 1$. For dilute solutions, the activities of O and R can be approximated by their molar concentrations, c.

2.2.2 Models of the Electrochemical Double Layer

From the above non-structural, thermodynamic considerations it does not become clear how the interfacial potential difference depends on the spatial charge distribution. In order to obtain such information, models have been conceived for the arrangement of charges in the EDL. The first such model arose from the work of Helmholtz [52] and consists of two rigid sheets of equal but opposite charge, one residing on the metal and the other in the solution at a distance d from the metal surface, comparable to a parallel-plate capacitor

$$C_H^0 = \epsilon_r \epsilon_0 / d \tag{2.11}$$

where C_H^0 denotes the Helmholtz capacitance (per unit area), and ϵ_r and ϵ_0 are the relative and vacuum permittivity, respectively. This EDL model predicts a linear potential drop across the interface.

Later, Georges Gouy [53] and David L. Chapman [54], combined the effects of the electrostatic forces and of the thermal motion of ions in the solution near the

electrode surface resulting in a diffuse rather than rigid distribution of the ionic space charge. The charge distribution in this diffuse layer is controlled by a combination of the Poisson equation (Eq. 2.12) and the Boltzmann distribution function (Eq. 2.13)

$$\frac{d^2\phi}{dx^2} = -\frac{\rho_S(x)}{\epsilon_r\epsilon_0} \tag{2.12}$$

$$\rho_S(x) = ze_0\left[N_c \exp -\frac{ze_0\phi(x)}{k_BT} - N_a \exp \frac{ze_0\phi(x)}{k_BT}\right] \tag{2.13}$$

where $\rho_S(x)$ is the space-charge density in the solution, e_0 is the elementary charge, N_c and N_a are the cation and anion concentrations, respectively, and k_B is the Boltzmann constant. For the case of a univalent electrolyte, where the bulk anion and cation concentrations have the same value, N^0, we write

$$\frac{d^2\phi}{dx^2} = -\frac{ze_0N^0}{\epsilon_r\epsilon_0}\left[\exp -\frac{ze_0\phi(x)}{k_BT} - \exp \frac{ze_0\phi(x)}{k_BT}\right] \tag{2.14}$$

which is a nonlinear differential equation for the inner potential $\phi(x)$. Considering only small potentials, so that $|\phi(x)| \ll k_BT/ze_0$, the exponentials can be linearized and one obtains the linear Poisson-Boltzmann equation:

$$\frac{d^2\phi}{dx^2} = \kappa^2\phi(x) \tag{2.15}$$

where κ corresponds to the reciprocal Debye length, $\kappa = 1/\lambda_D$

$$\kappa = \left(\frac{2(ze_0)^2N^0}{\epsilon_r\epsilon_0k_BT}\right)^{1/2} \tag{2.16}$$

The general solution of the linearized Poisson-Boltzmann equation has the form:

$$\phi(x) = A_1\exp(-\kappa x) + A_2\exp(\kappa x) \tag{2.17}$$

The constants A_1 and A_2 are defined by the boundary conditions, $\phi(0) = \phi_0$ with $x = 0$ corresponding to the electrode surface, and $\phi(x \to \infty) = 0$ leading directly to $A_2 = 0$. From the first boundary condition we obtain $A_1 = \phi_0$. Hence, the potential is given by

$$\phi(x) = \phi_0\exp(-\kappa x) \tag{2.18}$$

where ϕ_0, the potential on the electrode, is given by the electroneutrality condition and Poisson's equation (Eq. 2.12):

$$\begin{aligned} -\sigma_M &= \int_0^\infty \rho_S(x)\mathrm{d}x = \int_0^\infty \epsilon_r\epsilon_0\frac{\partial^2\phi(x)}{\partial x^2}\mathrm{d}x = -\epsilon_r\epsilon_0\left.\frac{\partial\phi(x)}{\partial x}\right|_{x=0} = \\ &= -\epsilon_r\epsilon_0\kappa\phi_0 \end{aligned} \tag{2.19}$$

where σ_M is the surface charge density on the metal. One then obtains

$$\phi(x) = \frac{\sigma_M}{\epsilon_r \epsilon_0 \kappa} \exp(-\kappa x) \tag{2.20}$$

for the potential and

$$\rho_S(x) = -\sigma_M \kappa \exp(-\kappa x) \tag{2.21}$$

for the space-charge density. Therefore, the excess charge on the metal is counterbalanced by a space charge, which decays exponentially in the solution. The charge separation in the diffuse double layer can be described in terms of a differential capacitance (per unit area):

$$C_d^0 = \partial \sigma_M / \partial \phi_0 = \epsilon_r \epsilon_0 \kappa \tag{2.22}$$

The diffuse layer capacitance is hence the same as that of a parallel-plate capacitor with the plate separation given by the Debye length, $\lambda_D = \kappa^{-1}$. In a physiological electrolyte solution with $\epsilon_r = 78$ and a concentration of 10^{-1} mol/l, one obtains $\lambda_D = 9.6 \cdot 10^{-8}$ cm and hence $C_d^0 = 71.9\,\mu\mathrm{F/cm^2}$.[51,55]

For higher electrode potentials, $|\phi(x)| \gg k_B T/ze_0$, the full one-dimensional Poisson-Boltzmann equation (Eq. 2.12) has to be solved and one obtains for the differential capacitance:

$$C_d^0 = \epsilon_r \epsilon_0 \kappa \cosh\left(\frac{ze_0\phi_0}{2k_B T}\right) \tag{2.23}$$

From this equation it becomes clear that the interfacial capacitance is not constant, but depends on the electrode potential, ϕ_0.

Otto Stern[56] suggested an improved version of the EDL, where the true size of the ions including their solvation sheath and the possibility of specific (nonelectrostatic) adsorption of ions are taken into account. By combining the ideas of Helmholtz and of Gouy and Chapman, Stern introduced the notion of a plane of closest approach of the ions to the metal surface, which divides the compact Helmholtz layer (sometimes also called Stern layer) from the diffuse part. The potential at this so-called outer Helmholtz plane (OHP) is defined as the zeta potential, ζ (Fig. 2.1). Specific or contact adsorption occurs with ions that do not have a primary hydration sheath when they are in the bulk of the solution. These are in general most anions, such as Cl^-, Br^-, and PO_4^{3-}, and some large cations. The locus of centers of these ions is known as the inner Helmholtz plane (IHP). Specific adsorption depends on the chemical nature of the ions rather than on their charge.[57,55]

In the Stern picture and in the absence of specific adsorption, the total capacitance (per unit area) of the EDL, C_{dl}^0, is the series combination of C_H^0 and C_d^0:

$$\frac{1}{C_{dl}^0} = \frac{1}{C_H^0} + \frac{1}{C_d^0} \tag{2.24}$$

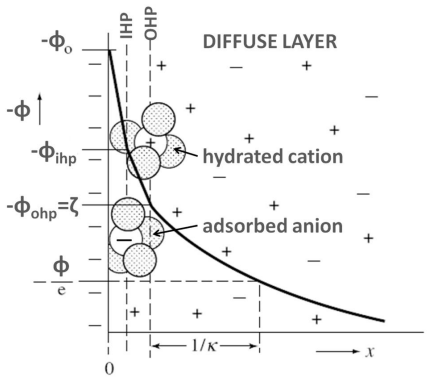

Fig. 2.1: Stern model (adapted [58]) of the electrochemical double layer indicating the inner Helmholtz plane (IHP) and corresponding potential, ϕ_{ihp}, and the outer Helmholtz plane (OHP). The corresponding potential, ϕ_{ohp}, is the so-called zeta potential, ζ. The thickness of the diffuse layer corresponds to the Debye length, $1/\kappa$.

It was shown earlier that for small electrode voltages, $C_d^0 = 71.9\,\mu\mathrm{F/cm^2}$. Experimental values for C_H^0 in aqueous solutions range between $20-30\,\mu\mathrm{F/cm^2}$.[59] For $d \approx 2.8 \cdot 10^{-8}\,\mathrm{cm}$ (the diameter of a water molecule), $C_H^0 \approx \epsilon_r \cdot 3.2\,\mu\mathrm{F/cm^2}$. The effective dielectric constant of the Helmholtz (or Stern) layer therefore has to be on the order of $6-9$. Such a low ϵ_r is caused by the strong polarization of the water dipoles in the high interfacial electric field. In comparison, the dielectric constant for water in the bulk electrolyte is about 78. The total capacitance per area amounts then to

$$C_{dl}^0 \approx 20\,\mu\mathrm{F/cm^2} \tag{2.25}$$

2.2.3 The Electrochemical Cell (I)

So far, the electrified interface has been described in terms of the difference between the Galvani potentials of the metal electrode and the solution, $\Delta\phi_{eq}$. In order to detect changes of this interfacial potential difference, e.g. caused by neural action potentials, the Galvani potential of the solution needs to be probed. By placing a second electrode in the solution, the measured overall potential difference would, however, also include the interfacial potential difference of this second electrode [60]1. By maintaining a constant interfacial potential at the second junction, any change in the measured potential difference may wholly be attributed to the first interface. One refers to the first electrode as the working electrode (WE) and to the second electrode as the reference electrode (RE). The interfacial potential difference of the RE can be fixed by keeping it in thermodynamic equilibrium. Recalling Eq. 2.6, we can consider $\Delta\phi_{eq}$ constant when $\Delta\psi_{eq}$ and $\Delta\chi_{eq}$ are constant. The latter describes the potential drop across the oriented dipole layers at the interface and

[1] In practice, additional interfacial potential differences arise, since any instrumental lead connected to the two electrodes creates a new interface unless the leads and all further instrumental interconnects are made of the same material as the electrodes.

the former represents the charge distribution at the interface. Both are constant in thermodynamic equilibrium, i.e. in the absence of an external field and at constant temperature and pressure. A system consisting of an electrode with unknown potential and a RE is termed an electrochemical cell, and the measured potential difference is a *relative* electrode potential, E. Eq. 2.10 may then be rewritten as:

$$E_{eq} = E^{\circ} + \frac{RT}{zF} \ln \frac{a_O}{a_R} \tag{2.26}$$

which is the more popular form of the Nernst equation. By standardizing the RE, a relative scale of electrode potentials can be determined, which by convention is the scale of the standard hydrogen electrode (SHE). The SHE operates through the equilibrium between H^+ and H_2 according to $2\,H^+ + 2\,e^- \rightleftharpoons H_2$. For neural recording, the SHE is obviously impracticable and one generally uses a simple Pt, stainless steel, or Ag|AgCl wire (or contact on the probe) instead that is placed in close proximity to the recording electrode in the tissue. Clearly, this configuration does not provide the most reliable RE in terms of a stable ionic environment. However, since one is not interested in the absolute value of E but rather its time dependence, drifts or fluctuations in the RE potential are in principle acceptable if they occur at a much slower time scale ($\gg$1 ms) or lower frequency ($\ll$1 kHz) than the neural action potentials. These unwanted low-frequency signals can easily be filtered out.

2.3 Electrochemistry of Stimulation

Electrical excitation of nervous tissue requires the application of either voltage or current pulses through an electrode placed close to the target brain area and a return electrode further away. Charge-transfer at the electrode-tissue interface is both electrical and chemical in nature: electrical because of the movement of electrical charges such as electrons and ions, and chemical because substances - the electrode itself and/or the host environment - may be modified. Electrical stimuli are accompanied by a change and redistribution of the ion concentration close to the electrode, which induces a transmembrane voltage in nearby neurons. For stimulation to occur, these concentration changes and hence transmembrane voltages have to reach a certain threshold level required to trigger an active cellular response.[61] Critical debates revolve around what strength and time duration of a stimulus pulse are required for the tissue to switch from an initial passive state to an active response.[62–67] The answer depends on a rather large number of variables, including the volume geometry of the tissue being stimulated, its electrical characteristics, and the location as well as geometry of the electrodes.

Any electric stimulus will impose a potential gradient across the electrode-tissue interface (in addition to the one already present, see Eq. 2.6). Part of the energy in

this external electric field is stored electrostatically in the double-layer capacitance and part is consumed (or stored) electrochemically by surface redox reactions of the general form given in Eq. 2.7. One speaks of non-faradaic electrode processes in the former and of faradaic or electron-transfer reactions in the latter case. Non-faradaic processes are purely electrostatic in nature and caused by the charging and discharging of the double-layer capacitance in response to an external electric field. Faradaic reactions, on the other hand, are characterized by an actual transfer of electrons between the electronic and ionic conductor and are described in terms of their reaction kinetics, i.e. the relationship between measured faradaic current and externally applied voltage.

2.3.1 Faradaic Charge-Transfer

The faradaic current density (or electrochemical reaction rate), i_f, for the reaction in Eq. 2.7 is the difference between the rates of oxidation (the anodic reaction), i_{ox}, and reduction (the cathodic reaction), i_{red}:

$$i_f = i_{ox} - i_{red} = \tag{2.27}$$

$$= i_0 \left[\exp \frac{\beta F \eta}{RT} - \exp \frac{(1-\beta) F \eta}{RT} \right] \tag{2.28}$$

where i_0 is the exchange current density, β is the so-called transfer coefficient, and $\eta = E - E_{eq}$ is the overpotential, i.e. the deviation of the (relative) electrode potential from its equilibrium value under an external voltage. The above expression known as the Butler-Volmer equation describes simple one-electron reactions ($z = 1$) in the absence of mass-transfer effects. [68,69]

Its physical interpretation is based on the *absolute rate theory* or *transition state theory*, which describes reaction rates in terms of an exponential probability of the reactants to overcome a potential energy barrier or energy of activation. For electrochemical reaction rates, the potential energy barrier in the interfacial region is assumed to be proportional to the overpotential. Hence, the overpotential associated with a given current provides the activation energy necessary to drive the reaction at the rate reflected by the current. [60] The transfer coefficient, β, is a measure of the symmetry of the energy barrier and for most systems lies between 0.3 and 0.7. At the equilibrium potential, i.e. $\eta = 0$, the anodic and cathodic currents have the same magnitude, i_0, thus canceling each other; no net current flow is observed. The exchange current density is a measure of the activation barrier height and hence of the kinetic feasibility of a redox reaction. A redox system with a large i_0 will attain equilibrium on a short time scale, while a small i_0 describes a sluggish system.

For small overpotentials in the range $|\eta| \ll RT/F \approx 25\,\mathrm{mV}$, Eq. 2.28 can be linearized by expanding the exponentials, and we obtain the linearized Butler-Volmer equation:

$$i_f = \frac{i_0 F \eta}{RT} \tag{2.29}$$

The quantity

$$R_{ct} = \frac{\eta}{i_f} = \frac{RT}{i_0 F} \tag{2.30}$$

is called the charge-transfer resistance and describes an electrode's resistance to faradaic current flow. It increases with decreasing i_0 and hence with slower reaction kinetics. One ought to bear in mind that for a given electrode material, i_0 and hence R_{ct} depend on the nature of the electrochemical reaction and are by no means global material properties. Each reaction has its own i_0 and R_{ct}.

Metal electrodes can provisionally be divided into two groups depending on the magnitude of R_{ct} for reactions involving their dissolution (corrosion) or deposition [?]. Electrodes with a large R_{ct} are termed polarizable, since a considerably large overpotential and hence electrode polarization is required to motivate a charge transfer and hence current flow. This overpotential is termed the *activation overpotential*, η_a. In contrast, non-polarizable electrodes have a small R_{ct} and hence facile charge-transfer kinetics allowing the current to pass freely across the electrode-electrolyte interface without the necessity to create a strong interfacial electric field. The charge distribution adjacent to the electrode thus remains undisturbed. [70] For neural stimulation, polarizable electrodes are preferred over non-polarizable ones because the current is largely electrostatic (capacitive) in nature. Non-polarizable electrodes, on the other hand, also rely on redox reactions, which may alter the chemical composition of the interface, an aspect that can raise problems in terms of material reliability and biocompatibility.

During neural stimulation, electrode overvoltages generally exceed the thermal voltage limit ($RT/F \approx 25\,\mathrm{mV}$). Under these conditions, the i_f vs. η relation is not determined by the reaction kinetics alone, but the reactant diffusion may come into play, which limits the current that can be supported by faradaic electrode processes. In this case, Eq. 2.28 must be modified to account for the time-dependent concentration profiles of reactants at the interface [60]

$$i_f = i_0 \left[\frac{c_O(0,t)}{c_O^*} \exp \frac{-\beta F \eta}{RT} - \frac{c_R(0,t)}{c_R^*} \exp \frac{(1-\beta) F \eta}{RT} \right] \tag{2.31}$$

where c_O^* and c_R^* are the bulk concentrations of the oxidized and reduced species, respectively, and $c_O(0,t)$ and $c_R(0,t)$ are the respective time-dependent concentrations at the electrode surface, which are themselves functions of η. For

the case of very fast charge-transfer, i.e. i_0 is very large, Eq. 2.31 simplifies to

$$\frac{c_O(0,t)}{c_R(0,t)} = \frac{c_O^*}{c_R^*} \exp \frac{F\eta}{RT} \tag{2.32}$$

Therefore, any variation in the surface concentrations, $c_R(0,t)$ and $c_O(0,t)$, gives rise to a change in overpotential called the *concentration overpotential*, η_c. This concentration polarization occurs in addition to the activation polarization. Consequently, for any given current, the observed overpotential is composed of at least two terms related to activation and diffusion:

$$\eta = \eta_c + \eta_a \tag{2.33}$$

For fast charge-transfer kinetics, the limiting factor for an infinitely growing exponential current is the maximum flux of reactants from and to the electrode. In this case, the current is diffusion-limited. In contrast, for kinetically hindered reactions, the system is under activation control. For diffusion-controlled electrode processes at a constant potential, the reaction rate will eventually reach a maximum when the reactant concentration at the electrode surface becomes zero, i.e. the concentration gradient becomes maximum. The diffusion-limited current density, i_l, depends on the electrode size and geometry, and for disc electrodes with a radius $r_e \leq 25\,\mu\text{m}$ [60], such as the ones employed in this work, it is described by:

$$i_l = \frac{4zFDc^*}{r_e\pi} \tag{2.34}$$

where r_e is the electrode radius, D is the diffusion coefficient, and c^* is the bulk concentration of the reacting species. [71,60]

2.3.2 Reversible and Irreversible Reactions

Ideally, a stimulation electrode should operate by non-faradaic mechanisms only and hence be perfectly polarizable with an interfacial capacitance as large as possible to electrostatically accommodate and displace sufficient charge for neural activation. In practice, however, no electrode material is perfectly polarizable. There are always faradaic leakage currents flowing due to redox reactions. Reactions that may damage an electrode or introduce potentially harmful compounds into the tissue should be avoided during stimulation and are often referred to as irreversible [72–81]. Thermodynamics provides a clear definition of reversible and irreversible reactions. In addition, there also exists the notion of chemical (ir)reversibility of redox reactions. In the context of neural stimulation, these differences have not always been pointed out with sufficient clarity.

By convention, a reaction is termed *thermodynamically* (or *electrochemically*, or *kinetically*) reversible when it obeys the Nernst equation, Eq. 2.26, i.e. when the

electrode potential is only a function of the surface reactant concentration and vice versa [60]. It can be shown that kinetically facile reactions behave reversible (or nernstian) and sluggish reaction kinetics leads to irreversible reactions. Following Eq. 2.32 for fast reaction kinetics and by substituting for c_O^*/c_R^* according to the Nernst equation (Eq. 2.26) one obtains

$$\begin{aligned} \frac{c_O(0,t)}{c_R(0,t)} &= \exp\left(\frac{zF(E_{eq}-E^\circ)}{RT}\right)\exp\left(\frac{zF(E-E_{eq})}{RT}\right) = \\ &= \exp\left(\frac{zF(E-E^\circ)}{RT}\right) \end{aligned} \tag{2.35}$$

and after rearrangement

$$E = E^\circ + \frac{RT}{zF}\ln\frac{c_O(0,t)}{c_R(0,t)} \tag{2.36}$$

This Nernst-like formalism is characteristic for kinetically facile reactions where a change of the electrode potential due to an external voltage leads to an instantaneous adjustment of the reactant surface concentration. A net faradaic current flows because the surface concentrations are not at equilibrium with the bulk, and diffusion causes a continuous flux of reactants to the surface. However, this reversible behavior is not absolute but depends on the time-scale of the experiment, which means that a reversible reaction may become irreversible if the speed at which the electrode potential is changed exceeds a critical value.

On the other hand, an electrochemical cell is *chemically* irreversible if reversing the current leads to different electrode reactions and new side products than originally present. Chemical irreversibility can be either quantitative or qualitative in nature: quantitative because part of the chemical species may simply diffuse away from the electrode prior to current reversal - the experimental time-scale plays again a critical factor - and qualitative because reaction pathways may change upon current reversal constituting other species than originally present at the interface, or because chemically instable species may react further and hence become unavailable for the reverse reaction.

The aspect of chemical irreversibility is more critical for neural stimulation than the kinetic irreversibility. For example, water electrolysis (cf. Section 4.2.3) is a highly undesirable process because gas formation and accompanying pH changes may damage the tissue. For Pt, which is a popular electrode material for neural stimulation, hydrogen gas evolution occurs at a very high exchange current density of $i_0 \approx 10^{-3}\,\mathrm{A/cm^2}$, which is one of the highest reported[2] (Fig. 2.2). The reaction practically requires no (activation) overpotential to proceed, but occurs at the

[2]This is also one of the reasons why Pt is an excellent electrocatalyst for fuel cell applications.

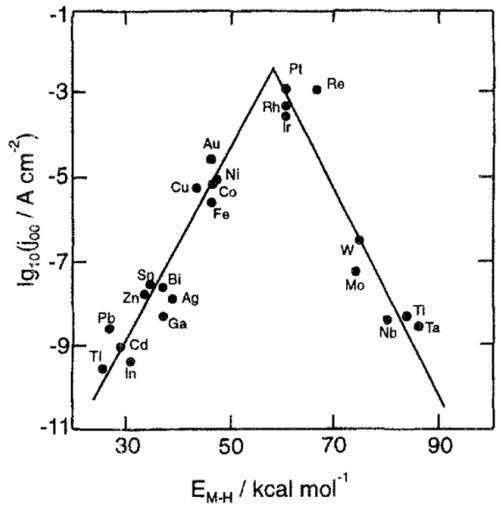

Fig. 2.2: Magnitude of the exchange current density, i_0, for H_2 evolution at different metals as a function of the adsorption strength between H atoms and the metal, E_{M-H} [82].

potential predicted by the Nernst equation (-0.61 V vs. Ag|AgCl at pH 7). Although the reaction is highly reversible from an electrochemical point of view, it is undesirable for stimulation because the chemical composition of the interface is changed and cannot entirely be reconstituted upon current reversal.

Another example of a chemically irreversible process is that of Pt oxide formation (and reduction). Unlike hydrogen evolution, this reaction is kinetically slow [83–85]. Fig. 2.3 displays the general mechanism. In the first step, OH^- ions are electrosorbed on the Pt surface (Fig. 2.3a), followed by a place-exchange between the metal surface atoms and the initially electrosorbed OH^- anions leading to a quasi 3D hydrous surface state (Fig. 2.3b). The thermodynamically irreversible nature of this mechanism causes a hysteresis-like behavior upon current reversal (Fig. 2.3c), i.e. the greater the extent of oxide formation (measured as a surface charge density) or the higher the potential at which it has been formed, the less positive (more cathodic) must the electrode potential be upon current reversal in order for it to become reduced [84]. This behavior is quite common for noble metals. It seems that due to the place-exchange mechanism, the reduction is not the reverse of the oxidation. If the surface structure of the Pt electrode cannot entirely be reconstituted, a gradually increasing surface roughness and oxide layer formation will occur under recurrent oxidation steps, which over time may corrode the electrode.

In general, chemical modifications of the interface are potentially harmful for both the electrode and the surrounding tissue and should be avoided during neural stimulation. While electrochemical corrosion can be considered the major failure mode of stimulating electrodes, several mechanisms have been proposed for stimulation-induced tissue damage. These include the formation of free radicals during oxygen reduction [86], the leaching of strongly oxidizing and hence toxic

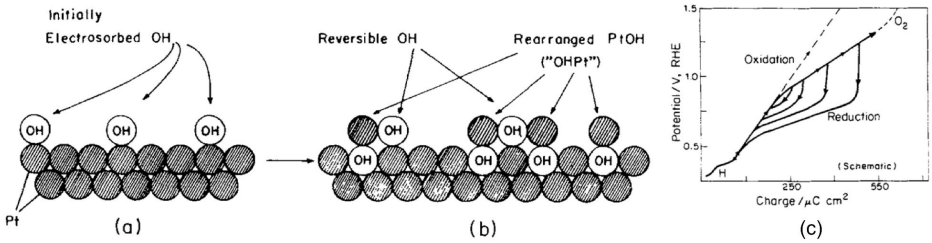

Fig. 2.3: (a, b) Place-exchange mechanism of initially electrosorbed OH^- during anodic oxidation of Pt. (c) Hysteresis-like behavior of the kinetically irreversible formation and reduction of a Pt oxide film (RHE: reversible hydrogen electrode). [84]

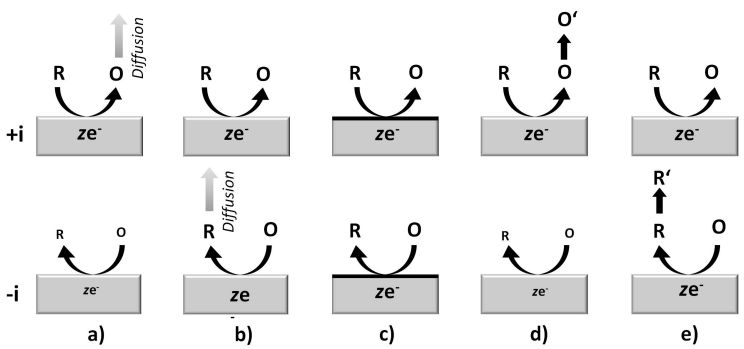

Fig. 2.4: Schematic of the various chemically irreversible faradaic electrode processes that may damage the electrode and tissue during neural stimulation. Shown is always the forward ($+i$) and reverse reaction ($-i$). (a, b) Diffusion of reactants from the electrode, (c) irreversible chemical modification of the electrode surface during the forward and/or reverse reaction, (d, e) irreversible chemical modification of the reactants.

corrosion compounds into the tissue [87], water electrolysis and accompanying local pH changes, and cellular hyperthermia. Fig. 2.4 schematically displays the possible reaction pathways that may interfere with the long-term tissue integrity and electrode viability.

2.3.3 The Electrochemical Cell (II)

In Section 2.2.3, the RE and WE have been introduced as the basic components of an electrochemical cell. In order to be able to drive a current through the WE, a third electrode is required, the counter electrode (CE). The current

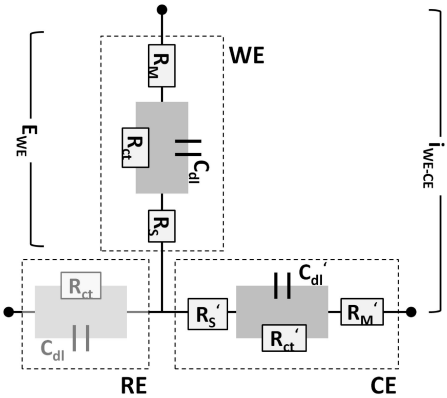

Fig. 2.5: Equivalent circuit representation of a 3-electrode electrochemical cell comprising the working electrode (WE), reference electrode (RE), and counter electrode (CE).

may never be applied between the WE and RE. As pointed out earlier, for an electrode to be able to function as an electrochemical reference, it must be kept at thermodynamic equilibrium, hence no (large) current may be drawn from it. The 3-electrode configuration consisting of WE, RE, and CE is standard for performing electrochemical studies. In order to have a visual representation of the voltage drops and current pathways that occur during an experiment, equivalent circuit models are often used to represent the physical quantities, such as the double layer capacitance, C_{dl}, the charge-transfer resistance, R_{ct} and other possible resistive and capacitive elements. These models are, however, only valid for the linear i_f vs. η response regime of R_{ct}, i.e. for low overpotentials (cf. Eq. 2.30). Fig. 2.5 shows the equivalent circuit representation of a 3-electrode electrochemical cell. Each electrode can be represented by a parallel $R_{ct}C_{dl}$ combination in series with the resistances, R_M and R_S, due to the metal interconnects and the solution, respectively. In practice, the RE does not contribute to the observed electrode potential because it draws only minimal currents. Hence, its equivalent circuit representation is only figurative.

2.3.4 Practical Aspects of Neural Stimulation

Neural stimulation is generally performed with trains of rectangular current or voltage pulses. Current pulses are frequently used in neurophysiology labs, while voltage pulses are common in clinical applications, such as DBS. Current-controlled stimulation has the advantage that the magnitude of the electric potential in the tissue is well-described and depends, in the simplistic view of a homogeneous and isotropic tissue volume, only on its conductivity. On the other hand, voltage stimulation leads to time-varying, nonlinear current responses (cf. Eq. 2.31) and hence electric potentials. Because neural excitation is linked to the potential field in

the tissue, current stimulation is more suitable to study the stimulation capabilities of an electrode system.

Stimulation pulses can be applied either in monophasic or biphasic mode (see Fig. 2.6). In 1955, John Lilly reported that tissue excitability with monophasic current pulses decreased with increasing pulse amplitude, while no such loss of excitability was observed with biphasic pulses [88]. It was later determined that monophasic pulses leading to the net buildup of potentially harmful electrochemical products are more prone to tissue damage than biphasic pulses where reaction products can be reversed. The primary current phase is designed to achieve neural excitation, while the subsequent secondary phase serves solely to achieve electrochemical reversibility. The primary phase must hence be applied according to the excitability of the neurons which may be different for cathodic or anodic currents. If the first phase of a biphasic current pulse is negative, stimulation is accordingly termed cathodic-first (CF) (Fig. 2.6d-f). The opposite is anodic-first (AF) stimulation.

Clinical neurostimulation including DBS uses cathodic-first voltage stimulation. This preference is probably related to early findings showing that activation thresholds of myelinated fibers are lower with cathodic current pulses than with anodic ones [89,90]. More recent studies, however, clearly point out that neural activation thresholds not only dependent on the stimulus polarity, but also the stimulus duration and location of the electrode relative to the neural structures [91–94]. Cathodic stimulation has been shown to be more efficient in activating neural elements parallel to the electrode surface, while anodic stimulation preferentially excites those elements perpendicular to the surface [95–98].

Further, pulses can either be symmetric (Fig. 2.6c, d, f) or asymmetric (Fig. 2.6e). Symmetric pulses are the most frequently used. Asymmetric pulses have been employed to study the efficacy of cochlear electrodes. [99] It was suggested that asymmetric pulses allow the application of higher charge densities, i.e. increase the limit of safe charge injection while maintaining electrochemical reversibility [15]. For CF pulsing, the immediate injection of a secondary anodic phase, which is necessarily hyperpolarizing the neural membrane, can annihilate the initiation of an action potential. To avoid this problem, either the stimulus strength of the primary phase must be increased relative to the first phase, i.e. by using asymmetric pulses, or a delay must be introduced between the primary and secondary phase [61] (Fig. 2.6f). It has been shown that the use of asymmetric pulse shapes combined with an interphase delay significantly reduce the stimulation threshold of cochlear implants [99]. The stimulation frequency or pulse repetition rate depends on the application, and for DBS, it can range from 50–185 Hz [100,29]. Possibly, also very high frequencies up to 10 kHz may prove effective as has been shown for spinal cord stimulation (Nevro, USA) (personal communication with Prof. Dr. Bart Nuttin). Finally, the phase width is equally application dependent, but several 10–100 μs are very common.

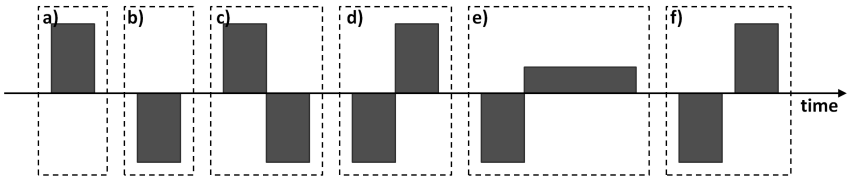

Fig. 2.6: Pulse shapes used for neural stimulation: (a) monophasic, anodic; (b) monophasic, cathodic; (c) biphasic, anodic-first, symmetric; (d) biphasic, cathodic-first, symmetric; (e) biphasic, cathodic-first, asymmetric; (f) biphasic, cathodic-first, symmetric with inter-phase delay.

2.4 Selection Criteria for Electrode Materials

This section provides an overview of the practical requirements that have to be met by electrode materials in order to safely and effectively interact with CNS. Aspects of biocompatibility are addressed and an overview of tested and classified implant materials is provided. The concepts of electrode impedance and charge storage/injection capacity is introduced as central criteria for selecting electrode materials for neural recording and stimulation. The discussion is accompanied by literature surveys of the most common electrode materials: Au, Pt, Ir, titanium nitride (TiN), iridium oxide (IrO_x), the conducting polymers polypyrrole (PPy) and poly(3,4-ethylenedioxythiophene) (PEDOT), and carbon nanotubes (CNTs).

2.4.1 Biocompatibility

Biocompatibility has been defined as the "*ability of a material to perform with an appropriate host response in a specific application*".[101] Considering this general definition, biocompatibility appears to be a rather intangible material property and may have to be uniquely defined for each application. In general, any implantation of a device or material is accompanied by tissue injury, which initiates an inflammatory immune response that leads to wound healing and eventually the formation of a fibrous capsule. The intensity and duration of the inflammatory and wound-healing responses depend on the degree of injury created by the implantation procedure, the persistence of mechanical stimuli over time due to, e.g. micromotions of the implant, and the chemical and physical properties of the implanted device or material. For the latter, it is crucial to recognize that any implanted material has specific bulk and surface properties, which can differ from each other and also change over time. Further, also effects of the host on the implant are important in mediating complications and device failure. These effects generally depend on the anatomical site involved and include corrosion, mechanical fatigue, and adsorption of tissue constituents[102].

Table 2.1: Classified *in vivo* neural biocompatibility of various implant materials.

	classification by Dymond [103]	classification by Stensas and Stensas [104]	other reference
Metals			
Al		non-reactive	
Co		toxic	
Cu		toxic	
Au	nontoxic	non-reactive	
Fe		toxic	
Pt	nontoxic	non-reactive	biocompatible [105,106]
PtIr	nontoxic		biocompatible [107]
Pt black	nontoxic		
Re	nontoxic		
Ag	toxic	toxic	
Stainless steel	nontoxic		
Ta		reactive	
Ti			biocompatible [106]
W		non-reactive	
Conducting Polymers			
Polypyrrole (PPy)			biocompatible [108]
Insulators			
Parylene C			biocompatible [109,110]
SiO_2 (Pyrex)		reactive	
TiO_2		reactive	
Semiconductors			
Si		non-reactive	biocompatible [111,112]

The biocompatibility of various materials has been validated in the brain of animals and categorized according to the extent of the induced inflammatory immuneresponse. Unfortunately, the classification terminology used in literature is not always consistent across different studies. Dymond [103] distinguished only between nontoxic and toxic materials, while Stensas and Stensas [104] employed three categories: non-reactive, reactive, and toxic. Table 2.1 provides an overview of materials that may be employed as electrode materials. Also listed are some semiconducting and insulating materials frequently employed for neural implants and toxic materials that may be present as traces. Materials that are considered safe for neural implants are termed either non-reactive, nontoxic, or biocompatible.

The observed toxicity or reactivity of certain metals in Table 2.1 can be related to their tendency for corrosion. Corrosion does not only affect the electrode material itself, but can also introduce new chemical species into the tissue which may become toxic when exceeding physiologically tolerable levels [113]. As discussed in Section 2.3.1, non-polarizable metals easily undergo dissolution and are characterized by a small charge transfer resistance, R_{ct}. In contrast, polarizable metals are inert and have a high R_{ct}. The correlation between polarization resistance

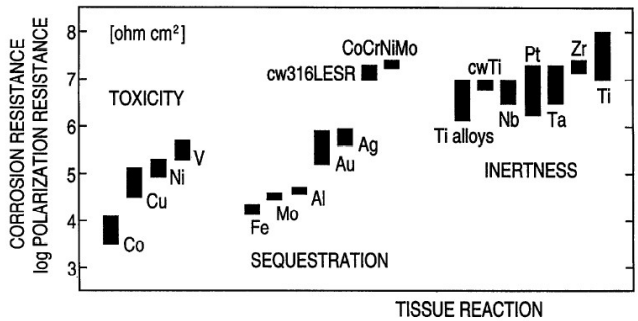

Fig. 2.7: Toxicity results from *in vivo* corrosion experiments (not brain) for various metals and alloys [114]. Tissue reaction is grouped according to: toxicity, sequestration (formation of stable chelates), and inertness. Corrosion resistance is roughly proportional to the measured polarization resistance ($=R_{ct}$).

($=R_{ct}$) and toxicity as determined from general *in vivo* data (not brain) is shown in Fig. 2.7. It can be seen that biocompatible materials, such as Pt, Ti, and Ti-based alloys also have the highest corrosion resistance, whereas toxic metals including Co, Cu, Fe and Ag have much lower corrosion resistances.

For other popular electrode materials including TiN and IrO_x, no *in vivo* biocompatibility studies (in the brain) are available, but they are commonly used in microsystems for *in vitro* neural applications [115–117]. The first use of CNTs as an electrode material has only recently been demonstrated [118]. The *in vitro* neural biocompatibility of plain CNT films synthesized by various methods is well-described [119–124], but only a few groups have demonstrated cultured neurons on microfabricated CNT electrodes [118,125].

2.4.2 Recording Efficacy

In Fig. 2.5, we have introduced a simple RC model of the electrode-electrolyte interface. Because the validity of this equivalent circuit is strictly limited to small overpotentials, it may only be a relevant model for the case of neural recording where extracellular signals are on the order of 10–10^2 μV. Stimulation voltages generally exceed the limit of linearity for R_{ct}. Depending on the RC characteristics of the interface, neural signals will be attenuated and distorted to some degree. One can fully describe the input-output behavior of the RC model and hence the recording efficacy of an electrode by analyzing its frequency-dependent impedance, $Z(j\omega)$, where j is the imaginary number and ω is the angular frequency. The

system impedance is generally represented using a complex notation [126]:

$$Z(j\omega) \equiv \hat{Z} = Z' + jZ'' = R_s + \frac{R_{ct}}{1 + (\omega R_{ct} C_{dl})^2} - j\frac{\omega R_{ct}^2 C_{dl}}{1 + (\omega R_{ct} C_{dl})^2} \tag{2.37}$$

where $R_s = R_S + R_M$ is the lumped series resistance (cf. Fig.2.5), and Z' and Z'' are the real (resistance) and imaginary (reactance) part of the impedance, respectively:

$$Z' = R_s + \frac{R_{ct}}{1 + (\omega R_{ct} C_{dl})^2} \tag{2.38}$$

$$Z'' = \frac{\omega R_{ct}^2 C_{dl}}{1 + (\omega R_{ct} C_{dl})^2} \tag{2.39}$$

Alternatively, the impedance is fully described by its modulus,

$$|Z|(\omega) = \sqrt{Z'^2 + Z''^2} \tag{2.40}$$

and phase angle,

$$\theta(\omega) = \arctan(Z''/Z') \tag{2.41}$$

For recording electrodes, the central figure of merit is the impedance magnitude at $\omega = 6283\,\text{rad}$, or equivalently $f = (\omega/2\pi)$=1 kHz. This is the characteristic frequency in the power spectrum of a neural action potential with a duration of 1 ms. For such a high frequency, Eq. 2.37 can be approximated by:

$$Z(i\omega) = R_s - i\frac{1}{\omega C_{dl}} \tag{2.42}$$

Since $R_s \ll (1/\omega C_{dl})$ in most cases, we obtain

$$|Z|(\omega) \approx \frac{1}{\omega C_{dl}} \tag{2.43}$$

One can therefore describe the underlying mechanism of recording electrodes as being largely capacitive in nature. For electrodes to reliably record extracellular neural signals, their impedance at 1 kHz should be as small as possible, preferably $\leq 1\,\text{MOhm}$. Considering that the impedance scales inversely with C_{dl} and hence the electrode area, miniaturizing the electrodes to enhance the recording resolution will inevitably deteriorate the impedance. Recalling Eq. 2.25, a flat disc electrode with a diameter of 10 μm results in $C_{dl} = 15.7\,\text{pF}$ and hence an impedance magnitude of $|Z|(1\,\text{kHz}) \approx 10\,\text{MOhm}$, which is considered too high to ensure reliable recording. Device engineers are therefore seeking to increase the effective surface area and hence capacitance of the electrodes by employing rough electrode materials or coatings.

Fig. 2.8a provides a literature survey of microelectrode impedances at 1 kHz vs. the geometric electrode area obtained with various electrode materials together with the theoretical behavior of a flat disc electrode (Eq. 2.43). The plot reveals two groups of materials. One group comprises the noble metals Au, Pt, and Ir and is well-described by the behavior of a flat disc electrode. The second group represents materials that have a much lower impedance. These materials are characterized by a high surface roughness and hence large specific surface area.

To our knowledge, the smallest microelectrodes that could successfully record neural signals *in vitro* were 64 μm^2 Au electrodes of 7 MOhm [127]. *In vivo* neural recording in the guinea pig auditory cortex could be demonstrated with 100 μm^2 Ir electrodes of 2 MOhm [36]. However, due to their high impedance, electrodes based on noble metals face serious limitations in terms of their potential for further miniaturization. To allow *in vivo* recording with functional electrodes of sub-cellular dimensions, it is essential to employ materials with a high surface roughness and hence capacitance.

Titanium nitride is an attractive electrode material because its microcolumnar morphology (Fig. 2.8b) gives rise to a large specific surface area. It is also a standard material in microfabrication technology. Among the materials with a high surface roughness, IrO_x (Fig. 2.8b) and the conducting polymers, PPy and PEDOT, occupy an exceptional position. In addition to a large C_{dl}, these materials are complemented by a so-called pseudocapacitance. It is related to chemisorption processes and redox reactions that take place at electrode surfaces of transition metal oxide films, such as IrO_x (cf. Section 4.2.3), but also occur with conducting polymers. Here, electrochemical redox reactions are associated with a sequential electron withdrawal and electron donation in response to charging and discharging cycles. The polymer molecules are thereby converted to multiply charged structures. Common to any pseudocapacitive behavior is, that the charge that is transferred in the underlying electrode processes is some function of the electrode potential, and as such resembles the behavior of a capacitance. Importantly, this kind of capacitance is faradaic in nature, rather than being associated with a potential-dependent accumulation of electrostatic charge, such as with the C_{dl}. The pseudocapacitance can be up to 3 orders of magnitude larger than the C_{dl} and thus significantly reduces the electrode impedance. [128,129]

The low impedance of the CNTs is largely determined by a very large C_{dl} due to the 3D distributed surface area (Fig. 2.8b). Upon appropriate treatment, the initially hydrophobic CNTs can be rendered hydrophilic, which gives rise to a very large interfacial capacitance when placed in physiological solutions. It has furthermore been recognized that that the interfacial capacitance of the CNTs can be enhanced by chemical modifications including surface functionalization with O-containing redox groups, electroactive transition metals and their oxides, and conducting polymers, which all rely on pseudocapacitive charging mechanisms similar to IrO_x [130].

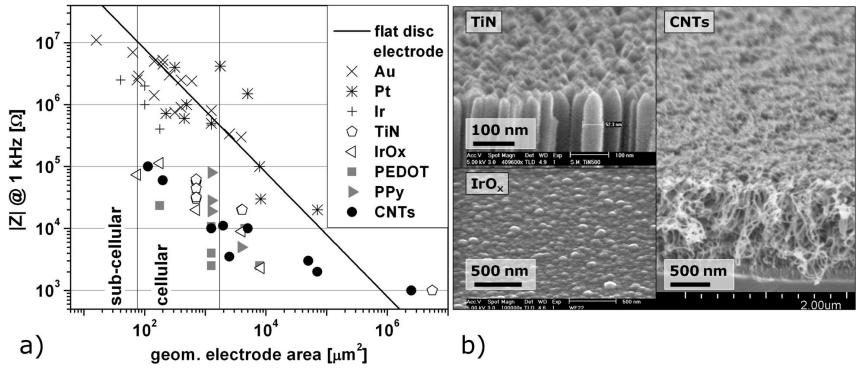

Fig. 2.8: Literature survey of electrode impedances at 1 kHz vs. geometric electrode area for various materials including Au [131–136,127,137,21,138], Pt [139–146,20], Ir [147,148,36,31,149], titanium nitride (TiN) [150,138,151,152], iridium oxide (IrO_x) [148,116,152,20], polypyrrole (PPy) [131,132,147], poly(3,4-ethylenedioxythiophene) (PEDOT) [153,131,147,148,146,154], and carbon nanotubes (CNTs) [139,155,133,156]. Measurements were performed in (buffered) saline solutions. Vertical lines divide the plot in sub-cellular, cellular (and supra-cellular) regime. (b) Examples of electrode materials with a large surface roughness: TiN, IrO_x, CNTs.

2.4.3 Stimulation Efficacy

Since Brummer [157] introduced electrochemical concepts to the field of neural stimulation in 1977, it has become common practice to define the safe operational limits of electrical stimulation as the electrode potential range between the onset of H_2 and O_2 evolution. Although it has been realized that potentially harmful reactions can commence prior to hydrolysis [72–81], this definition is widely used and helps to compare different electrode materials. The capability of a neural electrode to supply charge within the limits of hydrolysis is expressed in terms of a charge density and is the primary parameter in evaluating electrode materials for neural stimulation. Depending on the experimental conditions employed to determine this charge density, it is referred to either as the charge storage capacity, q_{csc}, or charge injection capacity, q_{cic}. The q_{csc} is determined experimentally by CV, an electrochemical technique where the electrode potential, E, is linearly (and slowly) varied between the (thermodynamic) limits of water hydrolysis (Fig. 2.9a). The measured current response, i, is the sum of faradaic (f) and double-layer (dl) contributions:

$$i = i_f + i_{dl} \tag{2.44}$$

with $i_{dl} = C_{dl}(dE/dt)$. The area under the resulting voltammetric i vs. E curve (Fig. 2.9b, c) is a measure for the amount of charge "stored" by the different electrode

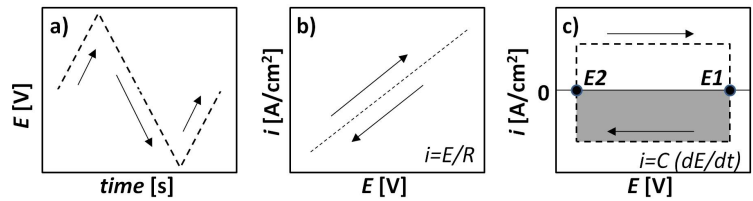

Fig. 2.9: Basic principle of cyclic voltammetry. (a) The electrode potential, E, is periodically ramped between two voltage limits. The resulting current response, i, is plotted over E. In the case of a pure resistive response (b), the voltammetric curve is a line, and in the case of an ideal capacitive response (c), the CV curve is rectangular. The shaded area under the CV curve is a measure for the cathodic charge density an electrode can "store" within the given potential limits.

processes. A purely resistive (linear) system (Fig. 2.9b) behaves dissipative and does not store any charge/energy, while a capacitive system stores charge electrostatically leading to a rectangular voltammetric response (Fig. 2.9c). The q_{csc} corresponds to the area under the CV curve divided by the voltage sweep rate, v. Mostly, only the cathodic branch of the CV curve is taken into consideration (shaded area in (Fig. 2.9c); cf. Section 2.3.4) and is determined according to:

$$q_{csc} = \frac{1}{v} \int_{E1}^{E2} i(E) dE \tag{2.45}$$

Using this cathodic q_{csc} rather than the total charge storage capacity as a qualitative measure is linked to the fact that most clinical neurostimulation therapies including DBS use cathodic-first stimulation. A shortcoming of the q_{csc} is that it is obtained by CV using waveforms, which are not realistic representations of the shapes (and time-scales) of the waveforms used for neural stimulation (see Section 2.3.4). Despite being neither a physiologically relevant nor a stimulation-specific measure, the cathodic q_{csc} remains a widely used figure of merit to compare the charge-storage capability of electrode materials under well-defined experimental conditions. Materials with a high q_{csc} are also expected to be more efficient for stimulation.

The q_{cic}, on the other hand, is determined under more realistic stimulation conditions using square-wave current pulses. The reported experimental and analytical approaches, however, suffer from various weaknesses and will be discussed in further detail in Chapter 4. Table 2.2 provides an overview of reported cathodic q_{csc} and q_{cic} values for various electrode materials. The values were obtained with different electrode sizes and under different conditions and cover therefore a rather broad range.

Charge density thresholds for eliciting functional responses in the CNS are not well-quantified, but values of at least 0.5 mC/cm^2 for pulse widths of less than 0.5 ms are expected for small microelectrodes ($r_e \leq 25\,\mu$m).[158–164] Comparing

Table 2.2: Literature survey of charge-storage capacities, q_{csc}, and charge-injection capacities, q_{cic}, available with different electrode materials.

	parameter	charge density [mC/cm^2]	references
Pt	q_{csc}	–	
	q_{cic}	0.05 – 0.35	[165,77,166]
TiN	q_{csc}	2.5	[152]
	q_{cic}	0.9 – 4.5	[152,167,168]
IrO_x	q_{csc}	11.0 – 100.0	[20,152,169–171,148]
	q_{cic}	1.0 – 9.6	[172,152,169–171]
PEDOT	q_{csc}	41.2 – 392.0	[148,22,147]
	q_{cic}	2.3 – 2.9	[146,154]
PPy	q_{csc}	160.0 – 186.0	[132,147]
	q_{cic}	–	
CNTs	q_{csc}	1.0	[173]
	q_{cic}	–	

with the values in Table 2.2, it becomes clear that Pt is the least efficient material for safe stimulation. Considering only the q_{cic} values, TiN, IrO_x, and PEDOT appear to be more suitable. Notably, their q_{csc} values are up to 3 orders of magnitude higher than their corresponding q_{cic} values, an aspect which underlines that CV is not an appropriate method to determine the stimulation efficacy of electrode materials because it strongly overestimates the applicable charge densities.

Despite considerable efforts to develop more efficient and safer electrode materials, the prevailing bottleneck of most materials is their insufficient long-term stability. *In vivo* pulsing for short durations with IrO_x electrodes has resulted in material degradation characterized by damaged IrO_x films and film fragments in the adjacent tissue [80]. Long-term *in vivo* stimulation studies caused mechanical damage to the IrO_x electrode-tissue interface, resulting in adverse tissue reactions [174]. Similarly, physical degradation, including cracks and delamination of PEDOT coatings, has been observed as the major failure mode in long-term stimulation [146], and PPy films have been reported to lose up to 95% of their electroactivity when subjected to prolonged polarisation [175]. An improved long-term performance of PPy films was achieved by creating composite polymers layered with multiwalled CNTs [176]. Increasing interest in CNTs as a material for neural electrodes mainly has been triggered by considerable progress in wafer-scale technologies for CNT synthesis in recent years [177]. However, there is only limited data available on the stimulation efficacy of CNTs. Much of what is known about the charge storage behavior of CNTs stems from research in the field of energy storage including supercapacitors, lithium batteries, and hydrogen storage [178,179].

2.5 Summary

The continuous trend towards smaller and denser electrode configurations for *in vivo* neural recording and stimulation exerts harsh demands on the electrode performance in terms of safety and efficacy. Identifying the bottlenecks of current electrode materials and possible remedies requires a thorough understanding of the physico-chemical mechanisms governing the electrode behavior. For this purpose, this chapter has provided an overview of the most important theoretical and practical considerations relevant to neural stimulation and recording, starting from basic thermodynamic and kinetic aspects of the electrode-electrolyte interface, over damaging factors related to electrical stimulation, to practical guidelines in terms of biocompatibility, and recording and stimulation efficacy of current and future electrode materials.

Chapter 3

Design, Fabrication, and Packaging of Neural Probes and of an *In Vitro* Test Platform

3.1 Introduction

Developing a functional neural probe is a process where initial design parameters are based on practical guidelines defined in literature, the combined know-how from neuroscientists and engineers, and the state-of-the-art of microfabrication technology. In this thesis, such initial design paradigms were realized with the first generation neural probe (1G probe), which was conceived to allow a first proof-of-concept validation of neural recording and stimulation in the cortex of rat brains. The insights gained in this "learning phase" were implemented in an improved second generation design (2G probe) aimed at demonstrating the overall thesis goal of deep brain recording and stimulation.

The probe design and fabrication specifications must comply with a set of requirements. First, materials employed for the substrate, electrodes, and insulation must be biocompatible and stable (cf. Section 2.4.1), at least for the period of a physiological experiment. Then, the probe dimensions are defined by the need for mechanical stability during implantation, minimal tissue damage, and the accommodation of a sufficiently large electrode array. Mechanical stability implies that the probe may not buckle or break during the insertion procedure, a requisite

that limits the minimal probe thickness.[180] The demand for minimal tissue damage is less tangible. An implanted probe will always induce tissue damage, and the extent of it may not always be related to the probe dimensions alone. It is a general rule that a probe's volume should be minimized in order to cause as little tissue trauma as possible. A recent study, however, points out the important aspect that the (acute) tissue damage depends on non-linear interaction effects between a probe's geometry including the shaft width, thickness, and tip angle and the speed at which the probe is implanted[181]. Such interaction effects have largely been overlooked in literature. Assuming the probe width has been determined based on the previous design considerations, the number of electrodes and interconnects that can be accommodated is only limited by technology. Finally, the electrode sizes must cover a range of meaningful values to allow experimentation at cellular (10–50 μm) and even sub-cellular scales ($< 10\,\mu$m).

In addition to the probes, an *in vitro* test platform was fabricated to allow straightforward electrode characterization independent of the probe fabrication and availability. The test chips were comprised of 1D and 2D electrode arrays with electrode diameters ranging from 5–50 μm diameter and electrode materials, including Pt, TiN, IrO_x, and CNTs. Particular attention was paid to the fabrication of the CNT electrodes in order to address concerns related to the safety and mechanical stability of such electrodes intended for *in vivo* applications. These issues and others related to the design, fabrication, and packaging of the probes and the *in vitro* test platform are described in further detail in the following sections.

3.2 Design Aspects

3.2.1 First Generation Probe

Fig. 3.1 shows CAD schematics of the 1G probes with metallization (light grey), passivation opening (black), and probe outline (dark grey). Table 3.1 summarizes the main design specifications. Electrodes with 50, 25, 10, and 2 μm diameter were realized. The length, L1, and width, W1, of the probe body (Fig. 3.1a) were 7.4 mm and 5 mm, respectively, and the dimensions of the insertable shaft were L2=2 mm and W2=240 μm for the probes with 50 μm diameter electrodes (Fig. 3.1b), and W2=200 μm for the designs with 25 μm (Fig. 3.1c), 10 μm (Fig. 3.1e), and 2 μm diameter electrodes. The shaft widths were tradeoffs between minimizing the probe dimensions as much as possible and accommodating a maximum amount of electrodes and metal interconnects with the given lithographic resolution. Metal lines had a width and spacing of 3 μm each in the tip region A (Fig. 3.1b), 5 μm each along the shaft area B (Fig. 3.1a). Along the probe body in region C, where the bond pads were located, the metal line width and spacing were 50 and 25 μm, respectively. The bond pads were $100 \times 100\,\mu m^2$ squares with a (center-to-center)

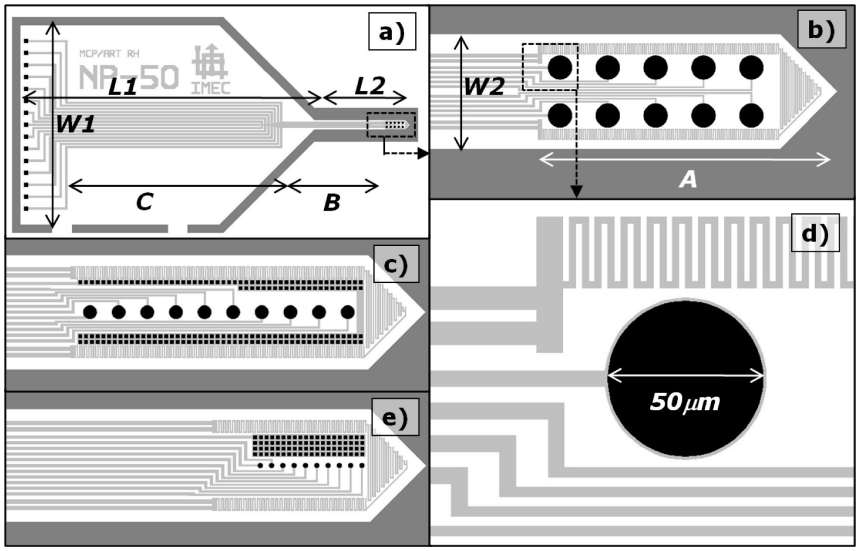

Fig. 3.1: Design layouts of the first generation probe: (a) Probe overview. (b, c, e) Close-ups of probe tips with 50, 25, and 10 μm diameter electrodes, respectively. (d) Close-up of a 50 μm diameter electrode with proximate metal interconnects and thermistor line.

pitch of 300 μm. A meander-like metal structure at the probe tip (Fig. 3.1d) was meant to serve as a thermistor to identify possible tissue heating effects occurring during electrical stimulation and/or MRI scans. This probe functionality was not evaluated because of setup restrictions and lack of effective stimulation data with the 1G probes. The thermistor lines had a width and spacing of 2 μm each and thus the smallest critical dimension in this design.

The 50 μm diameter electrodes were accommodated in a 2×5 array with a pitch of 100 μm in each dimension. All the other electrode configurations were linear 1×10 arrays with a pitch of 50, 20, and 6 μm for the 25, 10, and 2 μm diameter electrodes, respectively. The probe tip was chisel-shaped with an angle of 90°. Sharp tips were considered more damaging than blunt ones because they would act as blades transecting through the tissue and blood vessels during implantation. Blunt tips, on the other hand, were expected to displace rather then cut the tissue and hence cause less neuronal and vascular damage. Much controversy exists around this matter. It has been suggested that a probe with smooth surfaces and a sharp chisel-point tip is less likely to damage tissue when inserted [182]. It was argued, that a sharp tip cuts the intersected tissue across the full width of the shaft with minimal compression of the tissue under the blade edge. Separation of the tissue by the angled tip exerts lateral pressure on the tissue and thus helps

Table 3.1: Design specifications of the first and second generation neural probes.

specification	first generation	second generation
electrode Ø [μm]	2, 10, 25, 50	10, 25, 50
probe body width (W1) [mm]	5.0	5.6
probe body length (L1) [mm]	7.4	5.0
shaft width (W2) [μm]	200/240	200
shaft length (L2) [mm]	2 mm	10 mm
tip angle [°]	90	20

prevent microhemorrhage. On the other hand, Bjornsson et al.[24] observed that the tip geometry of silicon neural implants had little effect on vascular damage. In a recent study, combined effects of probe geometry and implantation speed were analyzed. The conclusion was that the least damaging probe tip design must be chosen in accordance to the insertion speed and vice versa.[181]

3.2.2 Second Generation Probe

For the 2G probe, the length, L1, of the probe body (Fig. 3.2a) was reduced to 5 mm in order to decrease the protrusion above the skull after implantation. The width, W1=5.6 mm, was slightly larger than on the 1G probe. The shaft dimensions were L2=10 mm (and 2 mm) in order to be able to reach deep brain and cortical regions and W2=200 μm (Fig. 3.2b). The tip angle was reduced to 20°. Combined with a slow insertion speed, this should minimize dimpling effects and penetration forces arising during probe insertion and hence tissue damage, at least in acute experiments.[183,181] Chronic tissue inflammation in response to implanted probes, on the other hand, was shown to be independent on probe size and shape[184], and also independent on the insertion speed[185]. In addition, a novel Si protection surrounding the probe shaft was implemented (Fig. 3.2a) to prevent damage to the sharp probe tip during handling and storage[186]. For improved mechanical stability, the neck of the probe was round-shaped unlike the angled neck of the 1G probe, which was prone to fracture during handling.

The thermistor structure was omitted in the 2G probe design. Electrodes had diameters of 50, 25, and 10 μm and were arranged in $2 \times 5 + 1$ 2D arrays (Fig. 3.2b) with a pitch of 100 μm in both dimensions for all electrode sizes. A large triangular tip electrode was included on each probe in reminiscence of tip wire electrodes, which are traditionally used for microstimulation[187]. The large area and close proximity of this electrode to the very tip of the probe was assumed to affect a larger volume of presumably undamaged tissue during neural stimulation as compared to the small disc electrodes, which are located on the side of the shaft and face a so-called kill zone[182], i.e. necrotic neural tissue populated by immune cells. The triangular electrode was designed with a geometric surface area of

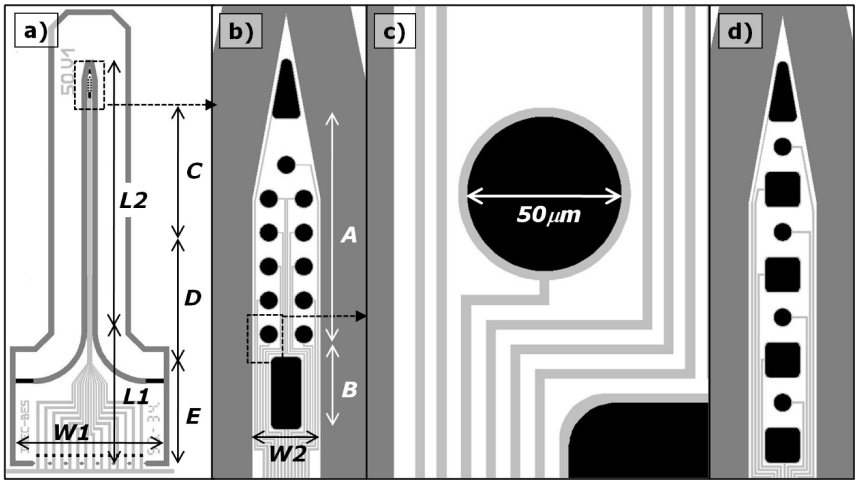

Fig. 3.2: Design layouts of the second generation probe.

9400 μm^2 and round corners of 12.5 μm radius to ensure a more homogeneous current density distribution across the electrode surface during stimulation. Sharp electrode corners should in general be avoided since they cause higher current densities and are thus more prone to corrosion. A similar electrode configuration combining a conical metal tip electrode and a polymer-based microfabricated electrode array has also been adopted for the AXIAL Deep Brain Array recently commercialized by NeuroNexus and FHC [188].

Our 2D arrays also comprised a large rectangular electrode intended to be used either as a reference electrode for neural recording or *in vivo* electrochemical characterization, or as a counter electrode during bipolar neural stimulation. Its geometric surface area is 18000 μm^2. Metal line widths and spacings were 3 and 4 μm, respectively, in the tip region A (Fig. 3.2b), 3 and 5 μm, respectively, next to the large rectangular electrode in region B, 5 μm each along the shaft segment C (Fig. 3.2a), 8 and 5 μm, respectively, along the shaft segment D, and, finally, up to 100 and 200 μm, respectively, along the probe body E. Bond pads were 100×100 μm^2 squares with a pitch of 300 μm.

Besides the 2D array, we also designed 1D arrays comprising 4 circular electrodes of either 10, 25, or 50 μm diameter alternating with 4 large square electrodes with round corners and a geometric surface area of 9858 μm^2. The center-to-center spacing between circular and square electrodes is 125 μm. This design resembles the clinical DBS electrodes and may thus similarly be used to study effects of neural stimulation in rodents. The circular electrodes would serve as recording electrodes. Alternatively, the large contacts may also be used for *in vivo* 4-point impedance measurements to study tissue properties in radial direction, i.e. parallel

to the shaft [189].

3.3 Fabrication

3.3.1 First Generation Probe

The 1G probes were realized with two different electrode materials: Ni/Au and Pt. The general process flow is outlined in Fig. 3.3. Probes with Ni/Au electrodes were fabricated on standard 6-in, 650 μm thick wafers, while the Pt-based probes were fabricated on 400 μm thick 8-in Si wafers (WaferNet, USA). In each case, 250 nm thermal SiO_2 were present on both the front and back sides. In the first step, metal lines, electrode areas, and bond pads were defined by lift-off (underlayer: LOR5A, Microchem, USA; photoresist: IX845, JSR-Micro, USA) of sputtered TiW/Au/Ti (30 nm/100 nm/30 nm) (A610 sputter system, Alcatel, USA) (Fig. 3.3a) or of sputtered Ti/Pt/Ti (20 nm/200 nm/20 nm) (Nimbus XP, Nexx Systems, USA). Lithography was performed on a MA6 mask aligner (Karl Suss, Germany). A 100 nm thick sputtered Ta_2O_5 layer (Nimbus 310, NEXX Systems, USA) served as an adhesion layer for the subsequent deposition of (nominally) 1 μm thick Parylene C (PDS 2010 Labcoater 2, SCS, USA).

Using a photoresist etch mask (IX845, JSR-Micro, USA), Parylene C and Ta_2O_5 were removed on top of the electrodes by means of reactive ion etching (RIE) ("3 chamber etcher", STS, UK) (Fig. 3.3b). Alignment accuracy was 1 μm. After removing the Ti from the Au contacts with a short dip in diluted hydrofluoric acid (HF), the electrode openings were filled with Ni by electroless plating (Fig. 3.3c). This additional plating step resulted in electrodes with a curved rather than planar surface (Fig. 3.4c), which should lead to a more homogeneous current density distribution during stimulation [190]. In another lift-off step, the Ni electrodes were covered with a stack of Ti/Au (30 nm/300 nm) (A610 sputter system, Alcatel, USA) for improved biocompatibility (Fig. 3.3d). Another RIE using a resist etch mask was performed to open the bondpads (Fig. 3.3e). For the probes with Pt electrodes, steps c and d in Fig. 3.3 were omitted, and steps b and e were merged.

Using a thick patterned resist on the wafer front side (AZ4562, Microchemicals, Germany), the probe outline and shaft thickness were defined by RIE of the Parylene C, Ta_2O_5, and SiO_2 and subsequent DRIE (STS ICP, UK) of 100 and 200 μm deep and 200 μm wide trenches (Fig. 3.3f). The same thick photoresist on the wafer back side patterned by back side alignment (AL 6-2, EVG, Austria) served as an etch mask for the through-wafer DRIE step (Fig. 3.3g). During this second DRIE step, the device wafer was temporarily bonded onto a carrier wafer using wax. The etched wafers were debonded in hot Microstrip and thoroughly rinsed in isopropyl alcohol (IPA) and distilled water. The final probes remained

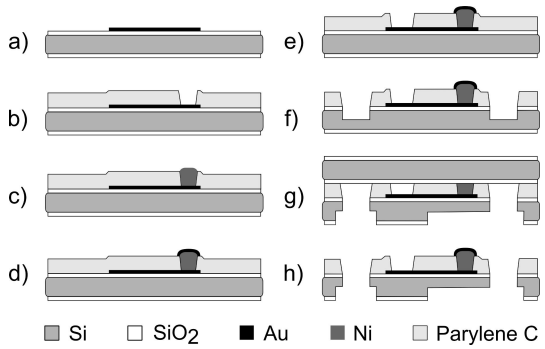

Fig. 3.3: Process flow of the first generation probes with Ni/Au electrodes. For probes with Pt electrodes, the Au metallization in step a was replaced by Pt, steps c and d were omitted, and steps b and e were merged.

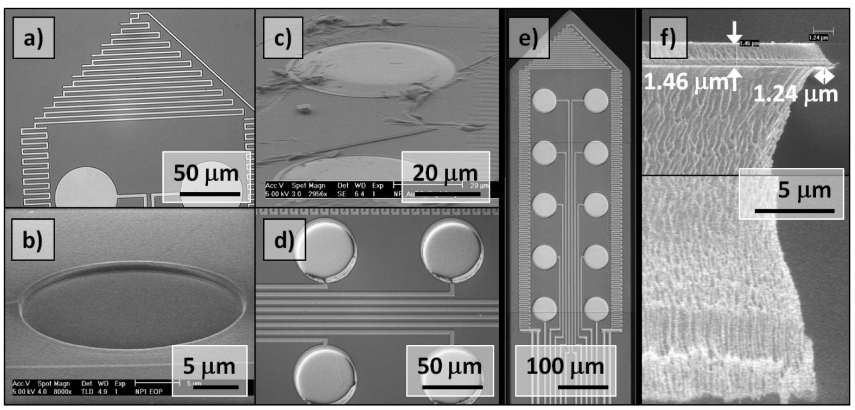

Fig. 3.4: First generation probe after: (a) Au lift-off, (b) electrode opening by reactive ion etching, (c) electroless Ni plating, (d) 2nd Au lift-off, (e) wafer debonding. (f) Side view SEM of the probe tip.

physically attached to the wafer through small struts. Fig. 3.4 shows optical and scanning electron microscopy (SEM) images of 1G probes after different processing steps. An underetch of up to 4 μm at the tip introduced by the DRIE (Fig. 3.4f) was considered acceptable.

3.3.2 Second Generation Probe

Unless otherwise stated, product and tool brands are the same as for the processing of the 1G probes. The process flow for the 2G probe is shown in Fig. 3.5. We used standard 750 μm thick 8-in Si wafers with 300 nm thermal SiO_2 on both the front and back sides and 200 nm PECVD SiN on the back side. Similar to the processing of the 1G probe, metal lines, electrode areas, and bond pads were defined by lift-off of sputtered Ti/Pt/Ti (20 nm/200 nm/20 nm) (Fig. 3.5a). Lithography was

performed on an IQ aligner (EVG, Austria). A 1 μm thick Parylene C layer was evaporated on the wafer frontside while protecting the back side with blue dicing tape. After removal of the dicing tape, openings on top of the electrodes and bond pads were etched by RIE (AMS 200 DSE, Alcatel, USA) using a photoresist etch mask (Fig. 3.5b). A thick photoresist (AZ10XT, AZ Electronic Materials, UK) served as an etch mask for the RIE of Parylene C and SiO_2 and the DRIE of 180 μm deep and 200 μm wide Si trenches (Fig. 3.5c). After cleaning in acetone, the wafers were temporarily bonded upside down on a Si carrier wafer using a spin-on polymer (HT-10.10, Brewer Science, USA) and thinned down to a final device thickness of 100 and 50 μm (DFG 850, Disco, JP) (Fig. 3.5d). For device singulation, the bonded wafers were diced along DRIE marks visible on the wafer back side. The resulting wafer pieces were placed into a glass beaker with debonder solution to dissolve the polymer glue and separate the probes from the carrier. The released probes were thoroughly cleaned in IPA. Optical and SEM (XL30, Philips, NL) images of final 2G probes are shown in Fig. 3.6. Nearly vertical sidewalls were obtained with very sharp tips.

3.3.3 *In Vitro* Test Chip

Test chips were fabricated with Pt, TiN, IrO_x, and CNT electrodes of 50, 25, 10, and 5 μm diameter. Processing was carried out on standard 8-in Si wafers with 300 nm thermal oxide on both the front and back sides. Metal interconnects, electrode areas, and bond pads were defined by lift-off of sputtered Ti/Pt/Ti (20 nm/200 nm/20 nm) (Fig. 3.7a). Lithography was performed on an IQ aligner (EVG, Austria). In a second lift-off step, TiN (100 nm; Nimbus XP, Nexx Systems, USA) was patterned on top of the electrodes (Fig. 3.7b) followed by RF sputtering of a thin, 2 nm thick (nominal) Ni layer (A610 sputter system, Alcatel, USA). Multiwalled CNTs were selectively grown on the electrode sites in a 200 mm microwave (2.45 GHz) plasma-enhanced chemical vapor deposition (PECVD) chamber (TEL, Japan) (Fig. 3.8a). The microwave plasma source was located remotely from the wafer surface to avoid excessive ion-bombardment favoring CNT formation over fiber-like structures. The CNT growth temperature was fixed at 425 °C. At this temperature, Ni is an effective catalyst for CNT growth because it is reduced to its catalytically active

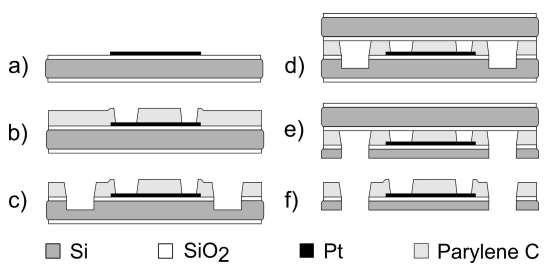

Fig. 3.5: Process flow of the second generation probe with Pt electrodes.

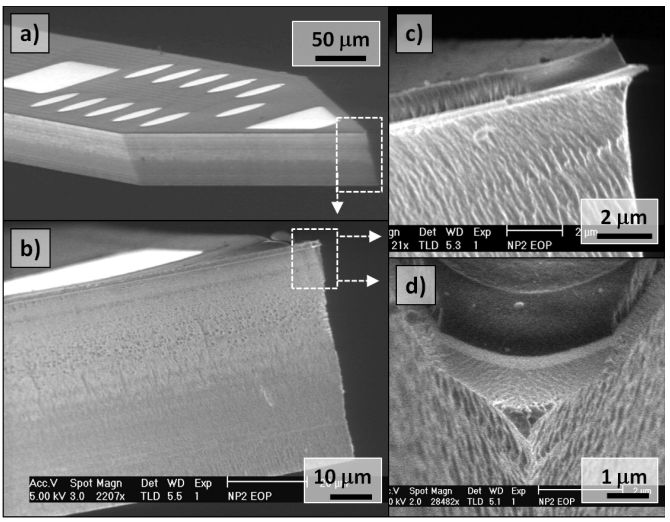

Fig. 3.6: (a) Overview SEM image of a second generation probe with a total thickness of 50 μm. (b–d) Close-up SEMs of the probe tip.

metallic state. In a typical CNT growth experiment, this Ni film was transformed into active metal nanoparticles in a NH_3 plasma for 5 min. The CNTs were then grown in a gas atmosphere of C_2H_4/H_2 at 3 Torr for 30 min resulting in a CNT density of $2 \cdot 10^{11}\,\mathrm{cm}^{-2}$, a height of 2 μm, and an average nanotube diameter of 34 nm (Fig. 3.7c and Fig. 3.8b).

Using vertically-aligned CNTs for implantable devices has raised concerns related to their mechanical stability during the insertion procedure where lateral abrasive forces may damage the CNTs[191]. In order to address these concerns, a novel approach is presented to encase and hence confine the vertical CNT electrodes. A coating stack comprising SiO_2 and Parylene C was employed with lithographically-defined electrode openings. In detail, a 300 nm thick SiO_2 layer deposited by chemical vapor deposition (CVD) at 150 °C (Plasmalab 80, Oxford Instruments, UK) served as a protection layer for the CNTs during subsequent fabrication steps (Fig. 3.7d and Fig. 3.8c, d). For insulation, 1 μm of Parylene C was evaporated (Fig. 3.7e). The bond pads were opened by RIE ("3 chamber etcher", STS, UK) of the Parylene C and SiO_2 using a resist etch mask (Fig. 3.7f). In a second RIE step, the Parylene C on top of the electrodes was etched (Fig. 3.7g). The etch time was adjusted to stop on the CVD SiO_2. Finally, the wafers were diced. The corresponding stack profiles for the TiN and Pt electrodes are shown in Fig. 3.7g' and g", respectively. The CVD SiO_2 covering the CNTs was removed in buffered hydrofluoric acid (BHF) only prior to electrochemical experimentation.

The SEM image in Fig. 3.8e displays an electrode after RIE of Parylene C and

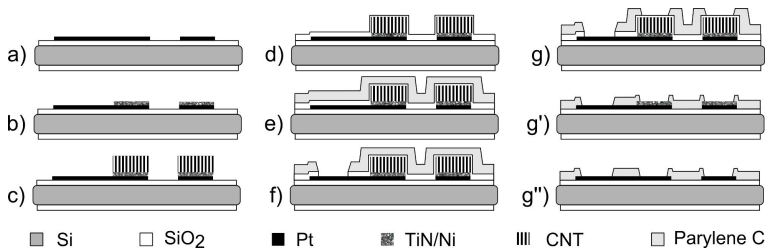

Fig. 3.7: Process flow for the test chip containing Pt, TiN, and CNT electrodes. For the fabrication of the TiN electrodes (g') steps c and d were omitted. For the fabrication of the Pt electrodes (g") steps b, c, and d were omitted.

etching of the CVD SiO_2 in BHF for 1.5 min. Due to this wet treatment and subsequent drying of the chips, capillary action caused a clustering of the CNTs, resulting in the formation of dense microbundles. A typical electrode edge partly encased in Parylene C is shown in the overview SEM image in Fig. 3.8f. It can clearly be seen that the Parylene C encasement is higher than the CNTs and should hence provide sufficient protection of the CNT electrodes from abrasive forces that may arise during implantation of prospective CNT-based neural probes. Focussed ion beam (FIB) combined with SEM was employed to analyze the details of the CNT-Parylene C interface of an electrode edge. A cross-sectional FIB/SEM image (Nova 600 Dual-Beam, FEI, USA) of the final electrode edge shows the CNT-Parylene C interface at the electrode opening (Fig. 3.8g). Dotted lines indicate the different layers, which are (from top to bottom): Parylene C, CNTs, TiN, Pt, and thermal SiO_2. Also clearly visible are large voids underneath the Parylene C stemming from the removal of the CVD SiO_2 by BHF. These voids are also discernible in the cross-sectional FIB/SEM image in Fig. 3.8h, which displays the CNT-Parylene C interface at the outermost electrode edge. Here, the indicated layers are (from top to bottom): CVD SiO_2 and thermal SiO_2.

Clearly, the BHF etch time was sufficient to remove the CVD SiO_2 on top of the CNTs and preserve the SiO_2 stack outside the perimeter of the electrode. This aspect is essential for maintaining an optimal insulation of the metal interconnects. From the FIB/SEM analysis it also becomes clear that the embedding and subsequent electrode opening did not visibly alter the CNT morphology. The influence of the different processing steps on the quality of the CNTs was investigated by contact angle measurements and Fourier-transform infrared spectroscopy (FTIR) analysis (cf. Appendix A, Fig. A.1). No difference between the spectra of the as-grown and BHF etched CVD SiO_2 coated CNTs was observed indicating that the different processing steps did not alter the chemical fingerprint of the CNTs. It was furthermore concluded, that the presence of the SiO_2 is essential for mediating the BHF into the CNT matrix and causing the formation of CNT microbundles, an effect which also increased the wettability of the CNTs. In contrast, no clustering

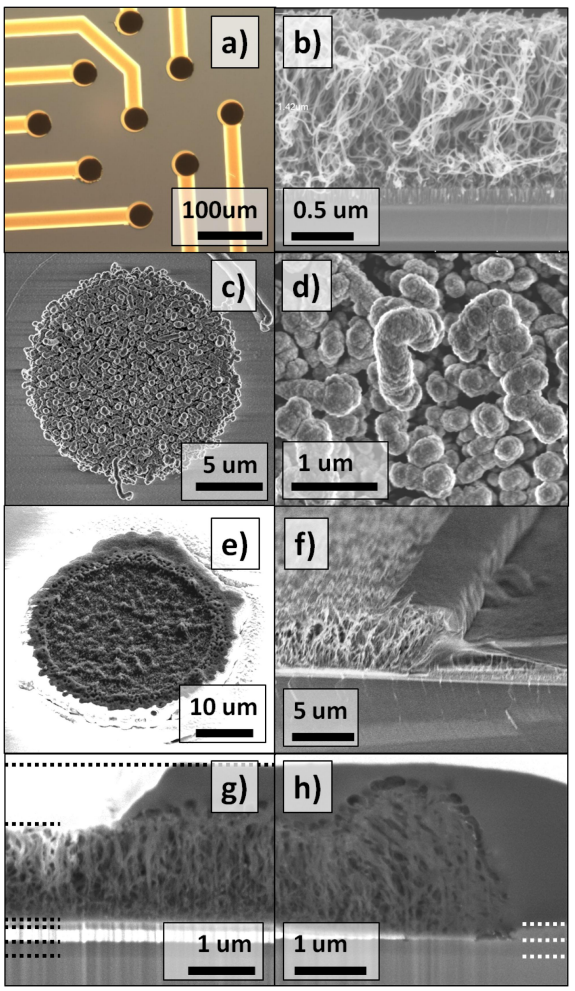

Fig. 3.8: (a) Optical micrograph of an electrode array after CNT growth on top of the electrodes. (b) Cross-sectional SEM image of the as-grown CNTs. (c) SEM image of an electrode and close-up (d) of the same after conformal CVD SiO_2 coating. (e) Overview SEM image of an electrode after etching of the Parylene C and removal of the CVD SiO_2 in buffered HF. (f) Overview SEM image of a typical electrode edge partially encased in Parylene C. (g) Combined FIB/SEM image showing details of the final CNT-Parylene C interface at an electrode opening. The layers indicated with dotted lines are (from top to bottom): Parylene C, CNTs, TiN, Pt, thermal SiO_2. (h) Combined FIB/SEM image showing details of the final CNT-Parylene C interface at the outermost electrode edge. The indicated layers are (from top to bottom): CVD SiO_2, thermal SiO_2.

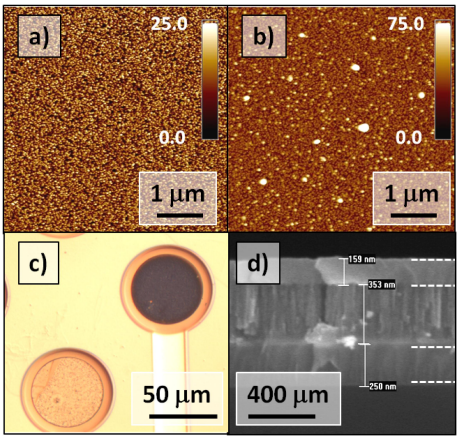

Fig. 3.9: AFM images of an (a) as deposited TiN and (b) H_2SO_4 treated TiN. (c) Optical image of a TiN electrode after IrO_x electrodeposition (top-right). (d) SEM image of a TiN sample after IrO_x deposition; the indicated layers are (from top to bottom): IrO_x (159 nm), TiN (353 nm), SiO_2 (250 nm).

and only a marginal wettability improvement was observed on as-grown CNTs immersed in BHF despite the largest IR signal increase due to hydrophilic O-containing functional groups.

The IrO_x electrodes were prepared by anodic electrochemical deposition. For the substrate, we used TiN electrodes fabricated as described above. The $IrCl_4$ (Wako Chemicals, Germany) solution was prepared and anodic electrodeposition was performed following previously reported procedures.[192,193] Iridium oxide was electrodeposited on TiN electrodes by submerging the electrodes in the $IrCl_4$ solution and applying a constant anodic voltage of 0.6 V for 10 min. Prior to IrO_x deposition, the TiN surface was electrochemically roughened by performing cyclic voltammetry in 0.5 M H_2SO_4 using the following settings: 40 cycles between -1.2 V and 1.1 V (vs. Ag|AgCl) at 0.5 V/s. For anodic deposition, we used a commercial potentiostat (Autolab PGSTAT302N, Ecochemie, NL). The root-mean-square (rms) roughness of the TiN increased from 4.37 to 7.82 after the H_2SO_4 treatment (Fig. 3.9a, b). Fig. 3.9c shows a final IrO_x electrode with the typical violet-black color. The IrO_x film thickness was ≈150 nm (Fig. 3.9d).

3.4 Probe Packaging

The fabricated 1G probes were gently extruded form the wafer frame and glued onto custom PCBs (Fig. 3.10, right-most device) using a biocompatible epoxy (353ND-T, EpoTek, USA). The PCBs had screw holes for fixture onto the stereotaxic frame during *in vivo* experimentation. After wirebonding, the same epoxy was used to hermetically seal the wires. For connectivity to experimental instrumentation, commercial 20-pin FPC connectors (XF2M, Omron, JP) were soldered on the PCB back side and used in combination with standard flexible flat cables (20-pin, axon',

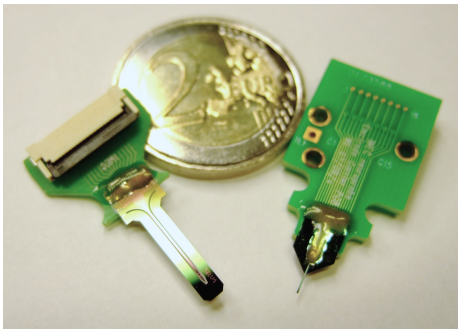

Fig. 3.10: Packaged first generation probe (right) and second generation probe (left).

France). Initially, the FPC connectors were not mounted on the PCB front side to allow face-to-face implantation of two probes. The weight of the packaged probes was 1.25 g. In order to further minimize the protrusion and weight of the packaged probe above the skull, the PCB design was modified for the 2G probes (Fig. 3.10, left-most device). The probes were again glued on the PCBs using epoxy, then wirebonded and sealed. The FPC connectors were soldered on the same side of the PCBs as the probes to facilitate handling during bonding. The packaged probes weighed only 0.49 g. The test chips were wirebonded on simple custom PCBs.

3.5 Summary

Two neural probe generations with Ni/Au and Pt electrodes were designed and fabricated for both cortical (1G) and deep brain (2G) applications in rat brains. Electrode diameters ranged from 2–50 μm for the 1G probes, and from 10–50 μm for the 2G probes. The probe tip angle was decreased from 90° (1G) to 20° (2G) in order to minimize dimpling effects during implantation. New to the 2G probes was a large triangular tip electrode intended for neural stimulation, and a large rectangular electrode, which may serve as a reference electrode during differential neural recording and *in vivo* electrochemical analysis, and also allows bipolar stimulation. Furthermore, the probe thickness was reduced from 200 μm (1G) to 50 μm (2G) in order to minimize tissue trauma during implantation. We also fabricated test chips with electrode diameters ranging from 5–50 μm and various electrode materials including Pt, TiN, IrO_x, and CNTs in order to study the size and material dependence of electrode properties. In the prospect of using CNTs for implantable probes, a novel fabrication approach was presented to partly encase the CNT electrodes and hence protect them from lateral abrasive forces that may damage the CNTs during implantation.

Chapter 4

Electrochemical Characterization of Electrodes

4.1 Introduction

One objective of this work was to develop neural electrodes that can function bidirectionally, i.e. both for recording and stimulation, and at the same time provide resolutions at a cellular and even sub-cellular scale. Basically, electrodes must have a low impedance, high charge-injection capacity, and be as small as possible. The experimental focus was two-fold: identify the best electrode material to meet the above requirements and provide an *in situ* electroanalytical approach to reliably determine safe stimulation ranges, i.e. the onset of harmful electrochemical reactions. The latter is by no means trivial. In the course of this work it became evident that reported approaches suffer from several methodological shortcomings.

Electroanalytical methods are by far the most appropriate to characterize electrodes for neural applications because they are non-destructive if applied well and can be carried out in an ionic environment, which resemble that of the EF in the brain. First order models of the EF account for the physiological concentrations of inorganic ions such as Na^+, Cl^-, K^+, the pH buffering capacity of the $H_2PO_4^-$, HPO_4^{2-}, and sometimes HCO_3^- anions, and finally the pH determined by the H^+ and OH^- ions. For most purposes it is sufficient to work in such buffer solutions. More realistic models, however, must also consider the presence of organic components, in particular proteins as these are redox-active, abundantly present in the EF and blood serum, and they readily adsorb on electrode surfaces.[194–199] Their influence on the electrode performance can be profound. Studies using spectrophotometric trace analysis demonstrated that stimulation-induced Pt dissolution is reduced *in*

vivo [76], and *in vitro* in the presence of albumin [200], which is the most abundant protein in the EF and blood serum (Table 4.1). This corrosion inhibition was attributed to the strong interaction between albumin and the Pt surface. While some attention has been devoted to stimulation-induced Pt dissolution in the presence of proteins, there is a lack of similar information regarding H_2 and O_2 evolution. This is mostly because the electroanalytical methods currently employed to characterize neural electrodes are neither specific nor sensitive enough to allow the *in situ* detection of individual electrode processes occurring under stimulation. Further, it has been suggested that the presence of dissolved O_2 in the brain can lead to harmful reactions during stimulation [78,81]. Realistic buffer solution must hence also account for the amount of dissolved O_2 in the brain.

In this work we have used various techniques to characterize the electrode behavior. CV was employed to identify the electrochemical fingerprint of each material and determine the cathodic q_{csc}. The electrode impedance was studied by EIS. Both CV and EIS are well-established techniques. In addition, a new method is presented to study electrodes subjected to current stimuli. It relies on reciprocal derivative chronopotentiometry (RDC), a known but rarely applied technique, in combination with a novel coulometric approach. We termed this method *coulometric RDC*. It allows the reliable detection of chemically irreversible reactions occurring during stimulation. All electrode materials, Pt, TiN, IrO_x, and CNTs, were characterized in inorganic buffer solutions. In addition, we also investigated the influence of albumin adsorption and dissolved O_2 on the performance of Pt electrodes.

The bulk of experimental data and conclusions presented in this chapter are almost entirely based on electrochemical measurements performed with test chips (cf. Section 3.3.3). Of course, the neural probes were themselves thoroughly characterized and compared against the test platform, but were primarily used for the *in vivo* validation. In order to demonstrate the equality of the test chips and neural probes, the presented results are always complemented with sample data obtained with actual probes.

4.2 Cyclic Voltammetry

4.2.1 Background

The basic principle of CV has already been introduced in Section 2.4.3 (Fig. 2.9). Here, we will only briefly review some of the main characteristics of albumin. Albumin is the most abundant protein in the EF (including interstitial fluid and cerebrospinal fluid (CSF)) and blood serum (Table 4.1). It is an acidic protein with a molecular weight of approx. 69 kDa and an ellipsoidal structure of 40×140 Å. At neutral pH it carries a net negative charge (Fig. 4.1). [201]

Table 4.1: Concentrations and isoelectric points of the three most common proteins in the human cerebrospinal fluid (CSF) and blood serum.

medium	protein [202]	concentration [% w/v]	pI
CSF	albumin	0.02 [202]	4.7 [202]
	β trace	2.6 E-3 [202]	7.6 [203]
	IgG	2.2 E-3 [202]	6.0 – 8.5 [202]
blood serum	albumin	3.4 – 5.4 [204]	4.7 [202]
	IgG	$\sim$ 0.65–1.85 [205]	6.0 – 8.5 [202]
	β lipoprotein	$\sim$ 0.1 [206]	$\sim$ 5.4 [207]

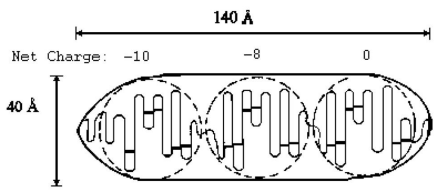

Fig. 4.1: Structure of serum albumin carrying a net negative charge at neutral pH. [201]

4.2.2 Materials and Methods

All electrode sizes and materials were characterized by CV. Measurements were performed in phosphate buffered saline (PBS) (0.150 M NaCl, 0.016 M Na_2HPO_4, 0.004 M KH_2PO_4, pH 7.4) at ambient conditions (25 °C, 1 atm). The experimental sequence consisted of an initial electrochemical cleaning step where the electrode potential was cycled at 2 V/s between the respective limits of gas evolution, also termed the *water window*, until a stable and reproducible response was observed (at least 50 cycles), followed by 10 slow-sweep CV cycles at 0.1 V/s. The cathodic q_{csc} was obtained from the 10th slow-sweep CV cycle. For the 50 μm diameter Pt electrodes, two additional buffer conditions were investigated: BPS supplemented with BSA (PBS-BSA) (1.5% w/v) and deoxygenated PBS (PBS_{deox}). For the former, 10 CV cycles at 0.1 V/s were performed without the electrochemical pre-cleaning step. The concentration of BSA was higher than that found in the CSF (Table 4.1) and slightly lower than that in blood serum to account for the unavoidable contact of neural implants with blood during surgery. Measurements in PBS-BSA were only performed after immersing the test chips in the buffer solution for at least 3 h. For measurements in PBS_deox, the PBS was purged with N_2 gas for at least 1 h prior to measurements. The gas bubbling was maintained throughout the experiments. Here, 10 CV cycles were applied at 0.1 V/s with an electrochemical pre-cleaning at 2 V/s. All chemicals were analytical grade and used as delivered (Sigma-Aldrich, USA).

Experiments were conducted in a glass beaker using a 3-electrode configuration

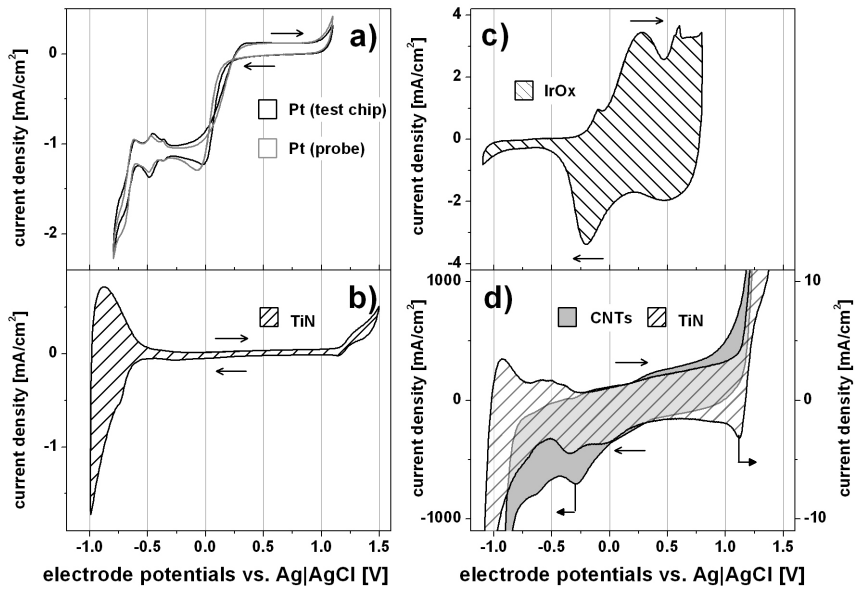

Fig. 4.2: Typical cyclic voltammograms obtained with (a) 50 μm diameter Pt electrodes (test chip and probe), (b) a 50 μm diameter TiN electrode, (c) a 50 μm diameter IrO_x electrode immediately after the anodic deposition, and (d) with 5 μm diameter TiN and CNT electrodes. Open horizontal arrows point in the scan direction.

placed inside a Faraday cage. A commercial double-junction Ag|AgCl (3 M KCl) reference electrode (Radiometer Analytical, France) was used together with a large-area Pt counter electrode. Measurements were made using an Autolab PSTAT302N potentiostat controlled by the NOVA software (Ecochemie, Netherlands). An additional low-current amplifier (ECD, Ecochemie, Netherlands) was used for low-current CV measurements with the 5 μm diameter electrodes. Data analysis was performed in OriginPro 8.5 (Originlab, USA).

4.2.3 Results and Discussion

Comparison of Different Electrode Materials

Fig. 4.2 shows typical CVs obtained with Pt, TiN, IrO_x, and CNT electrodes at 0.1 V/s in PBS. Except of the CNT and TiN curves in Fig. 4.2d, which were recorded with 5 μm diameter electrodes, all other measurements were performed with 50 μm diameter electrodes.

Platinum The CV curves in Fig. 4.2a recorded with the test chip and neural probe are basically identical, which confirms that the probe behavior can be well described by the test chip. The identified faradaic electrode processes can be assigned to the following redox reactions (Eqs. 4.1–4.6):

$$\text{reduction of dissolved } O_2: \quad O_2 + 4\,H^+ + 4\,e^- \longrightarrow 2\,H_2O \tag{4.1}$$

$$\text{H adsorption/desorption}: \quad Pt + H^+ + e^- \rightleftharpoons Pt{-}H_{ads} \tag{4.2}$$

$$H_2 \text{ evolution/oxidation}: \quad 2\,H_2O + 2\,e^- \rightleftharpoons H_2\uparrow + 2\,OH^- \tag{4.3}$$

$$\text{phosphate (de)protonation}: \quad 2\,H_2PO_4^- + 2\,e^- \rightleftharpoons H_2\uparrow + 2\,HPO_4^{2-} \tag{4.4}$$

$$\text{oxide formation/reduction}: \quad Pt + 2\,H_2O \rightleftharpoons PtO_2 + 4\,H^+ + 4\,e^- \tag{4.5}$$

$$O_2 \text{ evolution/reduction}: \quad 2\,H_2O \rightleftharpoons O_2\uparrow + 4\,H^+ + 4\,e^- \tag{4.6}$$

In the cathodic (negative) sweep, the large current step between 0–0.2 V is due to the reduction of dissolved O_2 (Eq. 4.1). As an intermediate step in this reaction, H_2O_2 may be produced according to Eq. 4.7. Peroxide is a very reactive chemical species and is considered a possible cause for tissue injury [78,81].

$$\text{peroxide formation:} \quad O_2 + 2\,H^+ + 2\,e^- \longrightarrow H_2O_2 \tag{4.7}$$

Cathodic adsorption and anodic desorption of H atoms (Eq. 4.2) occur between -0.3 and -0.6 V and are characterized by 2–3 distinguishable peaks related to different adsorption states on the polycrystalline Pt surface. Beginning at -0.6 V, the cathodic dissociation of water under H_2 gas evolution occurs (Eq. 4.3), which is accompanied by an increase in the local pH. The reduction shoulder at -0.7 V is related to the deprotonation of phosphate anions (4.4) [208,209]. The narrow region between -0.3 to -0.2 V is considered free of faradaic contributions and merely reflects the capacitive charging of the double layer. This region is therefore also called the *double layer region* of Pt.

In the anodic (positive) sweep, an ill-defined broad Pt oxidation region (Eq. 4.5) appears between 0.25–0.9 V with the corresponding cathodic Pt oxide reduction peak lying at approx. 0 V. The hysteresis-like behavior of this process is indicated by vertical arrows, which also mark the direction of the potential sweep. As already discussed in Section 2.3.2, the kinetically irreversible nature of Pt oxidation is responsible for this behavior where oxide reduction occurs at a lower potential than oxide formation. On the other hand, H adsorption and desorption give rise to a nearly symmetric CV response, which is typical for reversible processes. Generally, the anodic formation of oxide layers on platinum is retarded in electrolytes containing Cl^- ions, such as in PBS where the OH^- adsorption on Pt (cf. Fig. 2.3a) is competitively inhibited by the presence of Cl^- anions. [210–212] At electrode

potentials more positive than 1 V, O_2 evolution takes place (Eq. 4.6) and anodic dissolution of Pt can occur [209] according to

$$\text{Pt dissolution/redeposition:} \quad \mathrm{Pt} + 4\,\mathrm{Cl^-} \rightleftharpoons \mathrm{PtCl_4^{2-}} + 2\,\mathrm{e^-} \tag{4.8}$$

Excessive dissolution can not only degrade the electrode but may also lead to tissue damage when exceeding physiologically tolerable levels are exceeded.

Titanium Nitride Electrodes based on TiN (Figs. 4.2b and d) show a strong blocking behavior in the potential region -0.5–1.1 V where current flow is mostly capacitive in nature. This is typical for polarizable electrodes and possibly caused by the presence of a passivating surface oxide (oxynitride) introduced by RIE during processing (cf. Section 3.3.3) and/or air oxidation. In the anodic potential regime, the oxidative wave near 1.2 V can be attributed to the electrochemical oxidation of TiN to TiO_2 (Eq. 4.9), which proceeds through the formation of a mixed oxynitride/oxide phase [213? ?].

$$\text{Oxide formation/reduction:} \quad 2\,\mathrm{TiN} + 2\,\mathrm{H_2O} \rightleftharpoons 2\,\mathrm{TiO_2} + \mathrm{N_2} + 4\,\mathrm{H^+} + 4\,\mathrm{e^-} \tag{4.9}$$

Full oxidation of the TiN surface can occur at high anodic potentials resulting in the formation of a very stable oxide, which prevents further oxidation. The observed decrease of the anodic oxidation signal with an increasing number of cycles (data not shown) may be attributed to the formation of such an oxide layer. Evolution of O_2 gas (Eq. 4.6) presumably takes place for potentials higher than 1.1 V. Whether Cl^- ions also influence the anodic behavior of TiN similar to Pt (Eq. 4.8) was not determined. The steep increase of the cathodic current for potentials lower than -0.5 V is attributed to H adsorption and H_2 evolution (Eq. 4.3) [?]. The small cathodic shoulder at -0.7 V coincides with the signal observed with Pt, which was assigned to phosphate deprotonation. The TiN curve in Fig. 4.2d additionally reveals a reduction signal at 1.1 V in the cathodic sweep, which may be related to the reduction of O_2 evolved at the end of the preceding anodic scan. Two reductive shoulders at 0 and -0.25 V may be attributed to the reduction of the surface oxynitride and oxide layer. The overall tendency of the TiN surface to become oxidized and hence passivated may deteriorate the material's capability to supply charge during neural stimulation.

Iridium Oxide The interest in utilizing IrO_x, or more specifically the hydrous form of it, for neural electrodes is due to its pseudocapacitive character as already mentioned in Section 2.4.2. This property is related to the fact that hydrous iridium can shuttle between different oxidation states, Ir(I)-Ir(VI), depending on the applied electrode potential. The main redox pair consisting of the anodic peak

at 0.3 V and the cathodic peak at -0.2 V (Fig. 4.2c) is ascribed to the transition Ir(III) $\rightleftharpoons$ Ir(IV) [214,20,215]. The origin of the smaller oxidation peaks at -0.1 and 0.6 V is more controversial The transitions Ir(I) $\rightleftharpoons$ Ir(III) and Ir(III) $\rightleftharpoons$ Ir(IV) for the former, and Ir(IV) $\rightleftharpoons$ Ir(V/VI) for the latter have been proposed [214,216]. The general electrochemical reaction is described by [217]:

$$\text{Proton (de)intercalation:} \quad IrO_x(OH)_{3-x} + xH^+ + xe^- \rightleftharpoons Ir(OH)_3 \quad (4.10)$$

The pseudocapacitive behavior is based on successive electron transfer between Ir redox centers accompanied by changes in their coordination sphere. These changes are based on the inter-conversion between OH^- and O^{2-} sites. The overall electroneutrality of the bulk oxide is maintained by proton intercalation and deintercalation into the microporous oxide structure, which is an essential aspect of the mechanism of pseudocapacitative charging (and discharging) [218,219]. The phase transitions described by Eq. 4.10 involving injection and ejection of protons and electrons are accompanied by changes of the electrical and optical properties of the oxide, and by volumetric changes. The reduced form, $Ir(OH)_3$, is transparent and behaves like a semiconductor, while the oxidized form, $IrO_x(OH)_{3-x}$, is metallic and blue-black (cf. Fig.3.9), a phenomenon also known as electrochromism. Consequently, a significant increase in film resistance is expected upon switching from the metallic to the semiconducting phase (cf. Appendix B, Fig. B.1). [218,220]

A volume increase has been reported to occur upon immersion of IrO_x films in aqueous solutions and was attributed to the (re)hydration of the oxide film [221]. This volume change and accompanying internal stress may also explain why our IrO_x films consistently cracked upon re-immersing the chips in PBS and performing CV after 3 months storage in a N_2 dry box (Fig. 4.3). Other experiments in our lab [personal communication with Dr. D.R. Rand] have shown that annealing of the IrO_x film at 100 °C drastically reduced the overall voltammetric current response. This phenomenon is again related to the degree of oxide hydration, which deteriorates upon annealing at temperatures higher than 80°C [222,223]. The loss of hydration affects the ability of an IrO_x film to intercalate/deintercalate protons and hence store charge. Ensuring a certain degree of hydration of the IrO_x is clearly crucial for preserving the quality and stability of the material over a prolonged time.

Carbon Nanotubes The CNT electrodes (Fig. 4.2d) give rise to a strong capacitive response as evidenced by the large area under the CV curve and the lack of pronounced faradaic features. Besides a well-defined reductive peak at -0.25 V and a weaker shoulder at -0.6 V, only ill-defined broad oxidation bands can be discerned. The overall redox activity of the CNTs, including the reductive peak at -0.25 V, bears strong resemblance with the voltammetric response of the bare TiN electrode. This may indicate that the CNTs do not form a fully closed layer above the TiN and that the electrolyte is able to enter the CNT matrix and spread

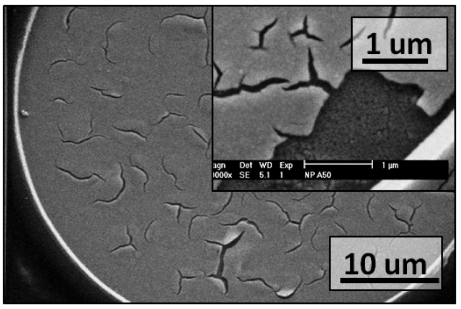

Fig. 4.3: Crack formation in an anodically deposition IrO_x film stored for 3 months in a N_2 dry box and subjected to CV in PBS.

over the TiN substrate. This would imply a good wettability of the CNT matrix, which is essential in order to provide a large accessible surface area and hence capacitance.

On the other hand, similar voltammetric features have also been reported for single-walled CNT sheets measured in aqueous solutions and were attributed to O-containing functional groups present on the CNT sidewalls [224]. These electroactive surface groups can easily undergo redox reactions (Eqs.4.11-4.13) causing a pseudocapacitive behavior similar to that described for IrO_x. Pseudocapacitance arises in addition to the double-layer capacitance and generally enhances the capability of a material to store charge. Unlike the double-layer capacitance, however, which relies on electrostatic charging, the pseudocapacitance is faradaic in nature. For CNTs, pseudocapacitance is associated to chemical modifications by functional redox groups and/or electroactive transition metals such as Ru, Ir, W, Mo, Mn, Co, Ni, and their respective oxides [225].

$$\text{hydroxyl oxidation/reduction}: \quad \mathrm{C{-}OH} \rightleftharpoons \mathrm{C{=}O} + \mathrm{H^+} + \mathrm{e^-} \tag{4.11}$$

$$\text{carboxyl oxidation/reduction}: \quad \mathrm{COOH} \rightleftharpoons \mathrm{COO} + \mathrm{H^+} + \mathrm{e^-} \tag{4.12}$$

$$\text{carbonyl reduction/oxidation}: \quad \mathrm{C{=}O} + \mathrm{e^-} \rightleftharpoons \mathrm{C{-}O^-} \tag{4.13}$$

By employing FTIR, we could identify the presence of O-containing functional groups in our CNTs (Appendix A, Fig. A.1). Furthermore, Ni may be present in trace amounts due to the catalytic CNT growth. Considering these aspects, it remains unclear for the moment, whether the observed redox activity of our CNTs is either due to chemical modifications or due to the TiN substrate (or due to both). In any case, only a small fraction of the overall current density available with the CNT electrodes is faradaic in nature, while the largest contribution stems from the non-faradaic electrostatic charging and discharging of the double-layer capacitance. This rather inert nature of the CNTs may prove beneficial in terms of minimal electrode degradation during prolonged stimulation.

Table 4.2: Average values for the cathodic q_{csc}, q_{csc}^{25}, q_{csc}^{50}, and water window for the Pt, TiN, IrOx, and CNT electrodes.

material	Ø [μm]	q_{csc} [mC cm^{-2}]	q_{csc}^{25} [a.u.]	q_{csc}^{50} [a.u.]	n_e	water window vs. Ag|AgCl [V]
Test Chip						
Pt	50	1.4 ± 0.0	–	1.0 ± 0.1	9	-0.60 – 1.00
	25	1.6 ± 0.2	1.0 ± 0.2	1.1 ± 0.1	6	
	10	3.5 ± 1.6	2.2 ± 1.3	2.5 ± 1.1	6	
	5	13.5 ± 3.0	8.6 ± 2.9	9.7 ± 2.2	8	
TiN	50	1.4 ± 0.2	–	1.0 ± 0.2	6	-0.75 – 1.10
	25	3.0 ± 1.3	1.0 ± 0.7	2.1 ± 0.6	8	
	10	5.4 ± 1.1	1.8 ± 1.4	3.9 ± 0.7	5	
	5	19.8 ± 1.7	6.7 ± 2.8	14.1 ± 1.7	6	
IrO_x	50	23.4 ± 5.3	–	–	6	-0.80 – 0.80
CNTs	25	513.9 ± 61.6	1.0 ± 0.2	–	12	-0.75 – 1.10
	10	2012.0 ± 208.2	3.9 ± 0.9	–	13	
	5	6612.1 ± 394.5	12.9 ± 2.3	–	12	
Neural Probe						
Pt	50	1.2 ± 0.3	–	–	10	-0.60 – 1.00

Cathodic Charge-Storage Capacity The magnitude of the voltammetric current response already indicates that the cathodic q_{csc} of the CNT electrodes must be orders of magnitude higher than that of the Pt, TiN, and IrO_x electrodes. Table 4.2 summarizes the average cathodic q_{csc} values for all investigated electrode sizes and materials obtained from n_e different electrodes. Also provided are the cathodic q_{csc} values normalized by the respective values of the 25 and 50 μm diameter electrodes, q_{csc}^{25} and q_{csc}^{50}, respectively. The voltage ranges of the water window are indicated.

The Pt and TiN electrodes give rise to almost identical q_{csc} values for all electrode sizes. Also, the Pt test chips and neural probe have comparable q_{csc} values. The presumably larger interfacial capacitance of the TiN electrodes due to the higher surface roughness can hence not compensate for the lack of faradaic electrode processes. An improvement of the q_{csc} by an order of magnitude compared to Pt and TiN is achieved for the 50 μm diameter IrO_x electrodes and is related to the pseudocapacitive effect described earlier. The q_{csc} of the CNT electrodes is almost 3 orders of magnitude larger than that of the Pt and TiN electrodes of the same size and also outperforms the IrO_x electrodes by almost 2 orders of magnitude. We may attribute this large charge-storage capability of the CNTs to the combined effects of a large C_{dl} and the pseudocapacitive behavior of functional redox groups and possibly also electroactive Ni or NiO.

It also appears that more charge per unit area is available with decreasing electrode area as indicated by the q_{csc}^{25} and q_{csc}^{50} values. Because of the low voltage sweep rate

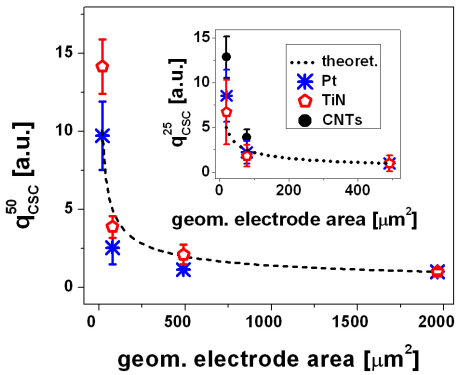

Fig. 4.4: Dependence of the normalized charge densities, q^{50}_{csc} and q^{25}_{csc} (inset), on the geometric area of the Pt, TiN, and CNT electrodes, and theoretical behavior of a microelectrode.

of 0.1 V/s, we can assume nearly steady-state (i.e. diffusion-controlled) conditions for our CV measurements. Hence, the voltammetric current density and also charge density scale inversely with the electrode radius (or $\sqrt{\mathcal{A}}$, where $\mathcal{A}$ is the electrode area) according to Eq. 2.34. The plots in Fig. 4.4 showing the relative charge densities, q^{25}_{csc} and q^{50}_{csc}, as functions of the electrode area are well-described by the theoretical behavior of a microelectrode under diffusion control. The deviation from the predicted behavior especially for the 5 μm diameter electrodes is most likely due to slight processing-related differences between the actual and nominal electrode area. Although these results are not unexpected, the possible implications for neural stimulation at a sub-cellular scale are unknown and deserve further investigation. Due to the obvious area dependence of the q_{csc}, a definitive benchmarking against the reported q_{csc} values in Table 2.2 is only possible to a certain extent. It can definitively be stated that the electrode materials investigated in this work do not underperform.

Influence of Albumin Adsorption on the Pt Behavior

Fig. 4.5 shows CVs obtained with 50 μm diameter Pt electrodes in PBS and PBS-BSA. The features of H adsorption and desorption (Eq. 4.2) are less well-defined in PBS-BSA [197]. In addition, phosphate deprotonation (Eq. 4.4) appears to be enhanced in PBS-BSA as compared to PBS. This may be related to the net negative charge of the adsorbed BSA, which promotes the deprotonation (=reduction) of the $H_2PO_4^-$ anions. Due to the adsorbed BSA film, surface electrochemical reactions including Pt oxidation and oxide reduction are inhibited in PBS-BSA [194]. This is evidenced by the consistent suppression of both the Pt oxidation shoulder at around 0.3 V and the oxide reduction peak at around 0 V. The voltammogram recorded in PBS-BSA shows an increased oxidative current in the anodic sweep from 0.5 V onwards, which is attributed to the adsorption and oxidation of amino acids [195,197,198]. It was suggested that the anodic adsorption and oxidation of proteins on Pt involves electron-transfer between acidic carboxylate groups on the

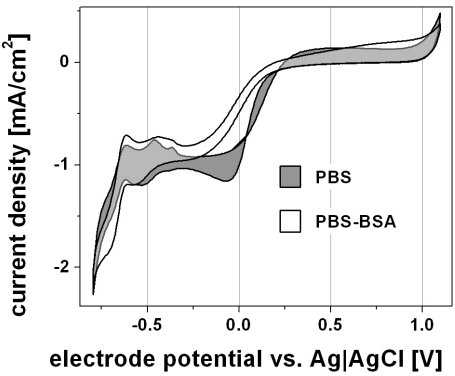

Fig. 4.5: Comparison of CVs measured with a 50 μm diameter Pt electrode in phosphate buffered saline (PBS) and PBS complemented with bovine serum albumin (PBS-BSA) at 0.1 V/s.

protein and the Pt surface[196,199]:

$$\text{protein adsorption}: \quad \mathrm{P} + \mathrm{zPt} \rightleftharpoons \mathrm{P(Pt)_z} + \mathrm{ze^-} \tag{4.14}$$

where P represents the protein and z is the number of carboxylate groups on the protein and hence the number of electrons transferred.

Influence of Dissolved Oxygen on the Pt Behavior

The effect of dissolved O_2 on the voltammetric behavior of 50 μm diameter Pt electrodes was investigated at two sweep rates, 0.1 V/s and 2 V/s. Based on RDC experiments discussed further below (Section 4.4.3), it was determined in retrospect that the higher sweep rate provides a better qualitative representation of the electrode behavior under real stimulation conditions. The lower sweep rate, on the other hand, represents the system at nearly steady-state and thus allows an estimation of the O_2 concentration based on the measured current density according to Eq. 2.34.

Fig. 4.6 shows the CVs measured at the two sweep rates in PBS and $\mathrm{PBS_{deox}}$. Increasing the sweep rate also increases the capacitive current due to the double-layer charging, which leads to a broadening of the voltammogram. At 0.1 V/s (Fig. 4.6a) we see that despite purging with N_2 gas there still remains a small current step at 0 V due to the reduction of dissolved O_2. From the change in current density indicated by the vertical arrow we can infer a reduction of dissolved O_2 by approximately 70%. The O_2 concentration in PBS can be estimated using Henry's law, $c = p/k_H$, relating the concentration, c, of a gas to its partial pressure, p, where k_H is an empirical constant (k_H=781 atm(mol/l)$^{-1}$ for O_2 dissolved in distilled water[?]). At ambient temperature (25 °C) and pressure (1 atm), the O_2 partial pressure is $p_{O_2} = 0.21$ atm, which also accounts for the partial fraction of O_2 in air. One therefore obtains $c_{O_2} = 269\,\mu$M. A reduction by 70% in $\mathrm{PBS_{deox}}$ hence corresponds to $c_{O_2} = 81\,\mu$M. The O_2 partial pressure in the rat's brain is

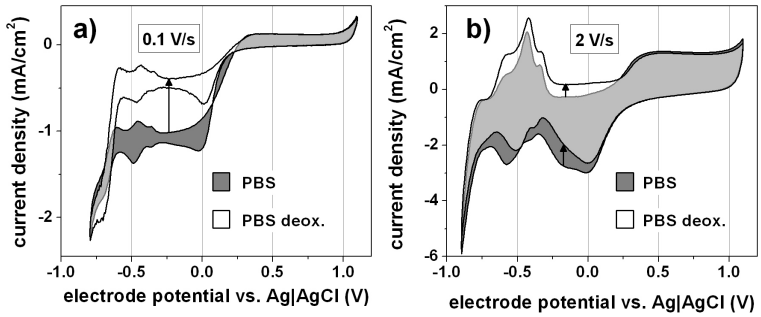

Fig. 4.6: Comparison of CVs measured with 50 μm diameter Pt electrodes in phosphate buffered saline (PBS) at ambient conditions and in PBS deoxygenated by continuous N_2 purging (PBS_{deox}) at (a) 0.1 V/s and (b) 2 V/s. The vertical arrows indicate the shift in current density due to the decrease of dissolved O_2.

very heterogenous and covers a range $4.6 \cdot 10^{-3}$–$72.4 \cdot 10^{-3}$ atm[226] resulting in O_2 concentrations between 5.9–93 μM. The straightforward experimental setup thus provides a good approximation of the O_2 concentration found in the brain.

The increased phosphate deprotonation signal (Eq. 4.4) in the cathodic scan can be ascribed to an enhanced mass transfer rate of phosphate ions to the electrode due to the agitation (convection) of the electrolyte. This enhanced phosphate deprotonation was not evident at a sweep rate of 2 V/s (Fig. 4.6b). In PBS_{deox}, the left half of the voltammogram is shifted upwards with respect to the curve in PBS similar to the case at 0.1 V/s. Except of a cathodic shoulder at -0.2 V, which was only observed in PBS and which can be assigned to O_2 reduction, the overall shape of the CVs was similar in both media.

4.2.4 Summary

Slow-sweep CV performed in PBS allowed the identification of the various faradaic processes occurring at the different electrode materials. The Pt and TiN electrodes resulted in the smallest q_{csc}, while an improvement of 1 and 3 orders of magnitude was achieved with the IrO_x and CNT electrodes, respectively. The large q_{csc} combined with a large water window and negligible faradaic contributions render the CNT electrodes by far the most suitable for stimulation. A good agreement between the performance of the Pt test chips and neural probe was demonstrated. The influence of BSA adsorption on Pt electrodes was investigated. It was shown that BSA adsorption kinetically inhibits the Pt oxide formation and reduction by blocking reactive sites on the Pt surface. An enhanced phosphate deprotonation was attributed to the net negative charge of the adsorbed BSA molecules. Oxidation of the BSA was detected at anodic potentials. Deoxygenating the PBS by purging

with N_2 gas decreased the extent of electrochemical O_2 reduction by 70% down to levels, which are also found in the brain thus presenting a realistic model system for studying the influence of O_2 reduction.

4.3 Electrochemical Impedance Spectroscopy (EIS)

4.3.1 Background

In Section 2.4.2, the electrochemical electrode impedance was briefly introduced as a central property determining the efficacy of recording electrodes. It was shown that an equivalent circuit model can be employed to describe the physical and chemical phenomena governing the i vs. E behavior of the interface. While allowing quite accurate predictions of the electrode impedance, the offered circuit model in Fig. 2.5 does not entirely reproduce the small-signal dynamic behavior of the electrode-electrolyte interface. Providing such an understanding may help elucidate, which material properties and form factors have to be optimized in order to result in more efficient electrodes and minimal electrode failure over time. In this section, the fundamentals of EIS are briefly reviewed with a primary focus on the various physical and chemical interfacial processes governing the electrode behavior and their corresponding equivalent circuit representations.

During EIS, a time-varying sinusoidal voltage signal, $E(\omega t) = E_0 \sin(\omega t)$ with E_0 being the signal amplitude is applied to the electrode under study (=WE), and the resulting current response, $I(\omega t) = I_0 \sin(\omega t+\theta)$ with I_0 being the current amplitude and θ the phase angle is monitored. Provided the electrochemical system behaves linearly, which is the case for small perturbation amplitudes ($E_0 \ll RT/F \approx 25\,\mathrm{mV}$), the dynamic system response in the frequency domain is fully described by its transfer function, or equivalently impedance, $Z(j\omega) = (E_0/I_0)\exp(j\omega)$. The complex notation of the impedance has already been introduced in Eq. 2.37. One way to graphically represent EIS data is in the form of a so-called Bode plot combining $|Z|$ vs. ω (cf. Eq.2.40) and θ vs. ω (cf. Eq. 2.41). An alternative and for neural electrodes less frequently employed representation is the Nyquist plot with Z'' vs. Z'.

The EIS provides direct information about the frequency-behavior of the electrochemical system and as such can be regarded analog to other types of spectroscopies relying on alternating electric fields. The relaxation phenomena one intends to discover with EIS are generally located in the lower frequency spectrum, 10^{-1}–$10^{6}\,\mathrm{Hz}$ depending on the application, and are hence related to the dynamic effects of bound and/or mobile charges in the bulk and interfacial region. In this regard one may speak of ionic/electric, space-charge, concentration (or diffusion), and kinetic (or charge-transfer) polarization phenomena. These

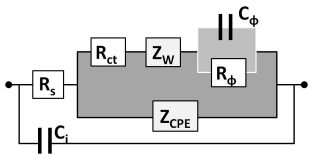

Fig. 4.7: Equivalent circuit representing the various interfacial processes contributing to the small-signal ac electrode polarization: R_s (series resistance), R_{ct} (charge-transfer resistance), Z_{CPE} (constant-phase element impedance), Z_W (Warburg diffusion impedance), C_ϕ (pseudocapacitance), R_ϕ (charge-transfer related to the pseudocapacitance), C_i (parasitic capacitance).

phenomena generally are spatially distributed and dependent on the species of charge present, the microstructure, and chemical nature of the interface. Each of these polarization phenomena has its own specific i vs. E characteristic leading to a specific circuit element representation. In the following, we discuss the circuit elements and underlying processes that have been of importance in this work. Fig. 4.7 shows a complete circuit model of the interface.

Electric and ionic polarizations of the metal and electrolyte, respectively, (indicated as R_M and R_S in Fig. 2.5) obey Ohm's law and as such can be represented by a single lumped series resistance, R_s in Fig. 4.7. Similar to the resistance of an ohmic metal-semiconductor contact, the solution resistance is often termed spreading resistance and depends on the electrode geometry and solution resistivity. For recessed disc electrodes, such as the Pt electrodes in this work, one obtains: [227]

$$R_S = \frac{\varrho_S}{4r_e} + \frac{\varrho_S h}{r_e^2 \pi} \tag{4.15}$$

where ϱ_S is the resistivity of the electrolyte (approximately $70\,\Omega\,\mathrm{cm}$ for PBS) and h is the height of the cylindrical recess, which corresponds to the thickness of the Parylene C. The metal resistance is governed by the geometry and resistivity of the metal lines and does not require further specifications and is in general negligible compared to the solution resistance.

The kinetic polarization represented by the charge-transfer resistance, R_{ct}, has already been introduced (cf. Eq.2.30), likewise the space-charge polarization of the double layer, C_{dl}. Here, the assumption was that the electrode-electrolyte interface is atomically smooth. In reality, of course, it has microscopic irregularities and structural defects, and more often than not specifically adsorbed and included (or intercalated) chemical species influence the local electric field. Such spatially distributed interface properties are not well represented by ordinary lumped circuit elements, but require the use of equally distributed impedance elements. An empirically derived description of the frequency behavior of such distributed phenomena was first provided by Cole [228] in 1942 in relation with the dielectric

constant behavior of polar liquids and solids:

$$\epsilon_r - \epsilon_\infty = \frac{\epsilon_r - \epsilon_\infty}{\left[1 + (j\omega\tau_0)^{(1-\alpha)}\right]} \tag{4.16}$$

where ϵ_∞ is the high-frequency limit of the relative permittivity, τ_0 is the mean dielectric relaxation time, and α is an empirical parameter describing the width of the frequency distribution of dielectric relaxation times.[229] It was also pointed out by Cole[228] that such behavior can be represented by an empirical impedance with a power-law frequency-dependence:

$$Z_{CPE}(j\omega) = \frac{1}{T(j\omega)^\alpha} \tag{4.17}$$

where CPE is an acronym for *constant-phase element* to account for the fact that the phase angle of Z_{CPE} is frequency-independent. The parameter T_{CPE} is a measure for the magnitude of Z_{CPE} and α may take values between 0 and 1 with $\alpha = 0$ describing a resistance and $\alpha = 1$ corresponding to an ideal capacitance.

Another type of distributed element arises on account of diffusional phenomena, which occur in response to charge-transfer and accompanying local concentration changes[230]. The concentration polarization or impedance that is observed under a small ac perturbation is described by[229]

$$Z_W(j\omega) = \sigma_W \omega^{-1/2} - j\sigma_W \omega^{-1/2} \tag{4.18}$$

where σ_W is the mass-transfer coefficient

$$\sigma_W = \frac{RT}{z^2F^2\sqrt{2}}\left[\frac{1}{\sqrt{D_O}c_O(0)} + \frac{1}{\sqrt{D_R}c_R(0)}\right] \tag{4.19}$$

with D_O and D_R being the diffusion coefficients of oxidized and reduced species, respectively, and $c_O(0)$ and $c_R(0)$ being their respective surface concentrations. Alternatively, using the relation $1/\sqrt{j} = (1/\sqrt{2})(1-j)$, Eq. 4.18 can be rewritten:

$$Z_W(j\omega) = \frac{\sqrt{2}\sigma_W}{(j\omega)^{1/2}} \tag{4.20}$$

which formally corresponds to Eq. 4.17 with $T_W = 1/(\sqrt{2}\sigma_W)$ and $\alpha = 0.5$. The diffusional impedance, Z_W, also known as the Warburg impedance[231], is hence only a special case of the more general Z_{CPE}. It has a constant phase angle of 45° and is placed in series with R_{ct}.

In addition to the interfacial phenomena mentioned above, one frequently encounters so-called pseudocapacitances, C_ϕ, which originate from faradaic electron-transfer processes involving a potential-dependent change of oxidation states, or of the chemical phase at the electrode surface. Such processes can neither be categorized

as space-charge nor kinetic polarization phenomena because there is neither an electrostatic build-up of charge involved as for C_{dl} nor a linear activation-controlled charge-transfer behavior as for R_{ct}. The pseudocapacitance was briefly introduced in Section 2.4.2 as a specific property of IrO_x, and, in this context, will be addressed in more detail further below (cf. Section 4.2.3). Besides the pseudocapacitance of transition-metal oxides, specific adsorption (or chemisorption) of atomic or molecular species can also give rise to pseudocapacitance if faradaic charge-transfer is involved. Such examples are the adsorption of H atoms on Pt (Eq. 4.2) prior to H_2 evolution [232] and the adsorption of charged proteins on metal surfaces [233]. The C_ϕ is placed in series with R_{ct} and parallel to Z_{CPE} (see Fig. 4.7). In certain cases, an additional charge-transfer resistance, R_ϕ, is required in parallel to C_ϕ to account for faradaic processes involved in adsorption/desorption processes [128].

Stray capacitances due to the device insulation (SiO_2 and Parylene C) and experimental setup (cables, electrochemical cell, etc.) also contribute to the overall measured impedance and are taken into account as C_i in Fig. 4.7. Numerical values of the impedance parameters are obtained by nonlinear least squares fitting (NLSF) of the experimental data to the equivalent circuit model.

4.3.2 Materials and Methods

All electrode sizes and materials were characterized in PBS. The experimental setup was the same as for CV (Section 4.2). The experimental sequence consisted of an electrochemical pre-cleaning step followed by EIS with a 10 mV (rms) ac signal applied between $1 - 10^5$ Hz. Measurements were performed at the electrodes' equilibrium potentials. The Pt electrodes were additionally characterized in PBS-BSA. Measurements were made using an Autolab PSTAT302N potentiostat with integrated frequency response analyzer controlled by the NOVA software (Ecochemie, Netherlands). We used OriginPro 8.5 (Originlab, USA) and ZView (Scribner, USA) for the data analysis and the NLSF of the EIS spectra, respectively.

4.3.3 Results and Discussion

Comparison of Different Electrode Materials

Fig. 4.8 shows the Bode plots of all electrode sizes and materials averaged over n_e measurements from n_e different electrodes (see Table 4.3 for the values of n_e). Fig. 4.9 compares the electrode impedances at 1 kHz obtained in this work with the values from the literature survey already presented earlier (cf. Fig. 2.8). The performances of our Pt and IrO_x electrodes lie within the reported ranges. On the other hand, our TiN electrodes have a much higher impedance than reported electrodes (about 1 order of magnitude) and show no difference to the

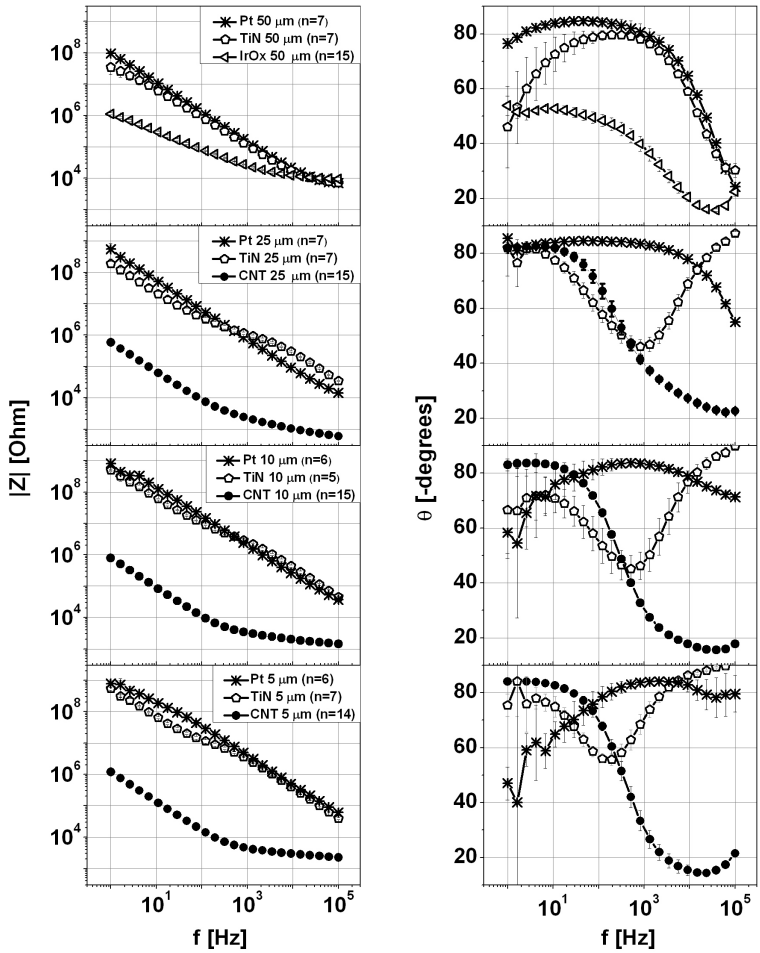

Fig. 4.8: Average Bode plots showing the impedance magnitude, $|Z|$, and phase angle, θ, obtained for the Pt, TiN, IrO_x, and CNT electrodes of 50, 25, 10, and 5 μm diameter measured between 1–10^5 Hz in PBS.

Pt electrodes. Clearly, the potential of TiN as a material for recording electrodes was not sufficiently exploited in this work. Possible reasons for this are provided further below. Our CNT electrodes outperform the Pt and TiN electrodes by 3 orders of magnitude and reported CNT electrode of comparable size by 1 order of magnitude[156]. Such behavior holds promise that electrodes even with sub-micron dimensions are feasible with a sufficiently low impedance.

All Pt electrodes in Fig. 4.8 are characterized by a phase angle, θ, close to the value of an ideal capacitor for which $\theta = -90°$. In contrast, the TiN electrodes show

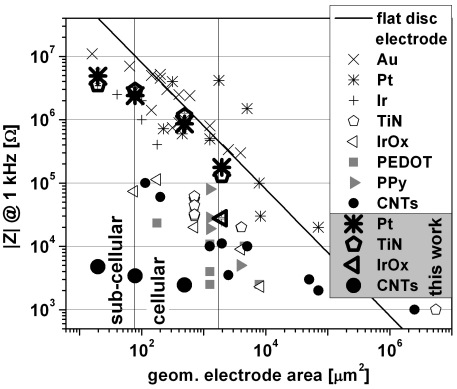

Fig. 4.9: Impedance magnitude, $|Z|$, at 1 kHz vs. geometric electrode area for the Pt, TiN, IrO_x, and CNT electrodes of 50, 25, 10, and 5 μm diameter obtained in this work in comparison to values reported in literature (cf. Fig. 2.8).

a marked faradaic behavior between 10^2–10^3 Hz. Electrodes coated with CNTs behave capacitively at low frequencies and resistive at higher frequencies similar to an electronic high-pass filter and typical for electrodes with a large interface capacitance. The impedance spectrum of the IrO_x electrodes is more elusive and is best analyzed by NLSF to the equivalent circuit provided in Fig. 4.7.

Table 4.3 provides the NLSF parameter for all electrode sizes and materials. The R_s of all 50 μm diameter electrodes (Pt, TiN, and IrO_x) is well-described by Eq. 4.15, which predicts $R_s = 7.36\,\text{kOhm}$. For the smaller electrodes, the R_s shows a strong dependence on the electrode material and is up to 3 orders of magnitude higher for the Pt and TiN electrodes as compared to the CNT electrodes. The R_s of the CNT electrodes can be described in terms of a porous electrode where the pores correspond to the interstitial electrolyte-filled space between the nanotubes. Assuming a cylindrical pore shape with the pore radius, r_p, the pore length, l, and the number of pores, n_p, the governing expression for the series resistance is [234]:

$$R_{s,p} = \frac{\varrho_S l}{r_p^2 \pi n_p} \tag{4.21}$$

The average diameter of the nanotubes is 34 nm (cf. Section 3.3.3). Assuming that the CNTs are arranged in a dense square lattice, the pores corresponding to the void space between the nanotubes can be approximated by cylinders with a radius $r_p = 7\,\text{nm}$. Further, the total number of pores equals the number of nanotubes, i.e. $n_p = 9.8 \cdot 10^5$ for the 25 μm diameter electrode, and the pore length corresponds to the height of the CNT film, $l \approx 2\,\mu\text{m}$. Using these values and a PBS resistivity of $\varrho_S = 70\,\Omega\text{cm}$, one obtains for a 25 μm diameter electrode $R_{s,p}$ =9.3 kΩ. In comparison, for a flat disc electrode R_s =15.4 kΩ. The latter is in good agreement with the corresponding value for a 25 μm Pt electrode in Table 4.3. On the other hand, the tabulated R_s for the CNT electrodes is more than an order of magnitude lower than the predicted $R_{s,p}$. Considering that the CNT length and density are reliably controlled during the growth process, the most uncertain factor in Eq. 4.21

Table 4.3: Average fitting parameters of the impedance spectra recorded with the Pt, TiN, IrOx, and CNT electrodes of 50, 25, 10, and 5 μm diameter.

Material	Ø [μm]	R_s [kΩ]	R_{ct} [kΩ]	T_{CPE} [nF s$^{\alpha-1}$]	α	T_W [μF s$^{-0.5}$]	C_ϕ [pF]	C_i [pF]	n_e
Test Chip									
Pt	50	7.53 ± 0.24	(7.97 ± 2.78) E5	1.85 ± 0.47	0.93 ± 0.02	–	–	54.79 ± 8.40	8
	25	20.38 ± 2.65	(6.23 ± 0.31) E6	0.32 ± 0.05	0.92 ± 0.00	–	–	56.46 ± 4.33	7
	10	80.81 ± 17.97	(1.36 ± 1.09) E6	0.13 ± 0.05	0.89 ± 0.03	–	–	32.21 ± 2.82	6
	5	(4.69 ± 2.70) E2	(2.12 ± 1.58) E5	0.47 ± 0.16	0.89 ± 0.04	(5.70 ± 2.49) E-4	–	23.93 ± 1.43	7
TiN	50	7.41 ± 1.71	(2.01 ± 4.34) E5	3.96 ± 1.33	0.89 ± 0.02	–	–	71.08 ± 20.76	8
	25	(0.83 ± 0.10) E3	(0.53 ± 0.15) E4	0.86 ± 0.18	0.84 ± 0.02	–	(2.49 ± 0.74) E2	49.38 ± 2.51	7
	10	(2.56 ± 1.51) E3	(1.78 ± 0.82) E4	0.39 ± 0.14	0.78 ± 0.06	–	75.83 ± 25.38	38.79 ± 4.52	5
	5	(7.02 ± 0.97) E3	(2.31 ± 0.79) E4	0.30 ± 0.08	0.80 ± 0.06	–	67.74 ± 8.53	43.19 ± 2.78	7
IrO_x	50	9.29 ± 1.25	(7.23 ± 5.55) E3	(2.46 ± 0.40) E2	0.62 ± 0.02	–	(3.66 ± 2.48) E4	49.19 ± 2.87	5
CNTs	25	0.63 ± 0.05	1.23 ± 0.14	(1.39 ± 0.32) E2	0.83 ± 0.02	11.73 ± 1.49	(1.92 ± 0.35) E5	(6.72 ± 0.53) E2	16
	10	1.15 ± 0.33	1.47 ± 0.13	(0.81 ± 0.24) E2	0.85 ± 0.03	11.43 ± 2.25	(1.52 ± 0.20) E5	(4.24 ± 2.33) E2	15
	5	2.37 ± 0.33	1.51 ± 0.21	(0.65 ± 0.12) E2	0.86 ± 0.02	10.58 ± 2.47	(0.87 ± 0.13) E5	(2.24 ± 0.31) E2	14
Neural Probe									
Pt	50	7.39 ± 0.29	(8.76 ± 8.08) E5	2.33 ± 0.32	0.91 ± 0.01	–	–	69.20 ± 7.33	10
	25	13.49 ± 0.65	(1.71 ± 1.50) E6	0.69 ± 0.14	0.91 ± 0.01	–	–	56.50 ± 7.79	8
	10	30.73 ± 9.55	(9.03 ± 6.13) E5	0.35 ± 0.12	0.84 ± 0.03	–	–	48.42 ± 3.67	5
	▲	4.02 ± 0.31	(2.70 ± 2.84) E5	9.57 ± 2.84	0.92 ± 0.01	–	–	(1.03 ± 0.15) E2	5
	▮	3.13 ± 0.71	(7.77 ± 8.16) E4	17.88 ± 5.83	0.92 ± 0.00	–	–	82.08 ± 33.24	4
	■	3.30 ± 0.05	(4.61 ± 1.12) E5	10.42 ± 8.33	0.92 ± 0.01	–	–	(1.26 ± 0.20) E2	8

▲: Triangular tip electrode. ▮: Rectangular reference electrode. ■: Square electrode.

is r_p. It can strongly be affected by the fabrication process and most likely covers a broad range of values. This also becomes evident from the SEM images in Fig. 3.8. The actual r_p for a 25 μm diameter electrode is therefore about 4 times larger than estimated. For the 10 and 5 μm diameter CNT electrodes we obtain 7 and 10 times larger r_p values, respectively, than estimated. An unexpected high R_s is seen for the TiN electrodes of 25, 10, and 5 μm diameter and may be attributed to the presence of a passivating oxide/oxynitride phase on the electrode surface.

The CNT electrodes have the lowest R_{ct}, which is 4–6 orders of magnitude lower compared to the Pt and TiN electrodes of the same size. Thus, charge-transfer occurs easiest at the CNT electrodes, which also explains why diffusional involvement in the form of the Z_W was mostly observed for the CNT electrodes. The enhanced reactivity of the CNTs may be related to the presence of O-containing functional groups as determined by FTIR (Appendix A, Fig. A.1) and possibly also redox active Ni traces [235,236]. The fast electron-transfer at the CNT electrodes may not evidently benefit neural stimulation, but is essential, if one intends to use CNTs for the *in vivo* electrochemical detection of redoxactive compounds, such as the neurotransmitters dopamine or serotonin. Carbon-fibre electrodes have a long tradition as *in vivo* neurochemical sensors [237], and microfabricated CNT electrodes are just starting to unfold their potential in this field [238,236].

The low impedance of the IrO_x and in particular CNT electrodes is a direct consequence of their large interfacial capacitance as reflected by T_{CPE} values, which are 2–3 orders of magnitude higher than for the corresponding Pt and TiN electrodes. Both, IrO_x and CNT electrodes also exhibit a strong pseudocapacitive contribution demonstrated by large C_ϕ values. The nearly ideal capacitive behavior of the Pt electrodes is reflected by a CPE exponent, α, close to unity, whereas the TiN, IrO_x, and CNT electrodes have smaller α values, which may indicate a higher roughness/porosity. One should be aware, however, that it is not only the structural roughness/porosity of a material that influences α. The extent of frequency dispersion is also influenced by the compositional properties of the interface and the mechanisms that govern the interfacial capacitance. This is in particular noticeable for IrO_x, where α depends on the electrode potential and hence on the extent of oxidation and hydration (Appendix B, Fig. B.1).

Finally, the parasitic capacitance, C_i, is comparable for the Pt, TiN, and IrO_x electrodes and is also comparable for the Pt test chip and neural probe. This is surprising considering that the probe unlike the test chip lacks a backside dielectric, and the Si is in direct contact with the PBS. The C_i of the CNT electrodes, on the other hand, is one order of magnitude higher compared to the other materials. Here, additional parasitic coupling compared to the planar Pt, TiN, and IrO_x electrodes may occur through the Parylene C-coated sidewalls of the vertical electrodes (see Fig. 3.8g).

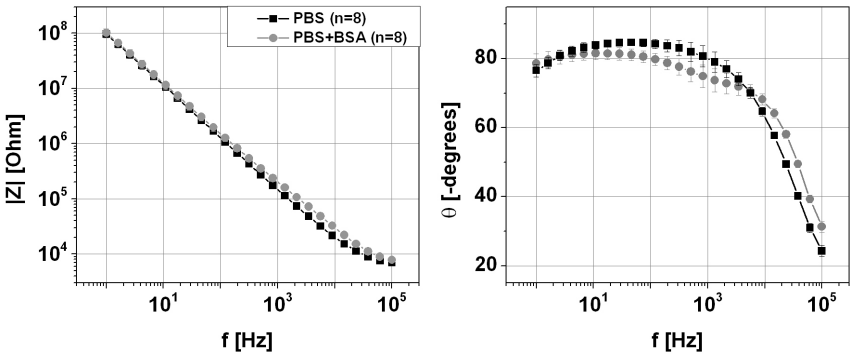

Fig. 4.10: Average Bode plots for Pt electrodes of 50 μm diameter measured between $1 - 10^5$ Hz in PBS and PBS-BSA.

Influence of Albumin Adsorption on the Pt Electrode Impedance

Fig. 4.10 shows the average Bode plots obtained with Pt electrodes of 50 μm diameter in PBS and and PBS-BSA. A closer analysis using NLSF (see Table 4.4 for the fit values) reveals that the BSA adsorption has no or only negligible effect on R_s, T_{CPE}, and α. In contrast, the R_{ct} was reduced by 2 orders of magnitude. At first, this does not appear consistent with the results from CV in PBS-BSA (cf. Section 4.2.3), which indicate a blocking of surface reactive sites. The enhanced reactivity seen with EIS is probably caused by faster charge-transfer kinetics between the Pt surface and functional groups of the adsorbed BSA molecules (Eq. 4.14). Similarly enhanced charge-transfer kinetics have also been reported for fibrinogen adsorption on Pt [199]. The presence of adsorbed BSA furthermore requires the introduction of a pseudocapacitance, C_ϕ, in parallel with a charge-transfer resistance, R_ϕ, (see Fig. 4.7). This pseudocapacitive behavior is probably also related to the presence of functional redox groups within the adsorbed BSA film.

Interestingly, in PBS-BSA a reduction of C_i was observed, which we attribute to the adsorbed BSA layer on the Parylene C acting as an additional insulation. This effect requires further investigation, and to our knowledge has not yet been taken into account in design studies of implantable probes. The electrode impedance at 1 kHz increases only by 35% in PBS-BSA, which is unlikely to have a significant impact on the quality of neural recording.

Table 4.4: Average fitting parameters of the impedance spectra recorded with 50 μm diameter Pt electrodes in PBS and PBS-BSA.

circuit element	medium	
	PBS	PBS-BSA
R_s [kΩ]	7.53 ± 0.24	6.61 ± 0.38
R_{ct} [kΩ]	(7.97 ± 2.78) E5	(1.31 ± 0.77) E3
T_{CPE} [nF s$^{\alpha-1}$]	1.85 ± 0.47	1.73 ± 0.46
α	0.93 ± 0.02	0.90 ± 0.02
C_ϕ [nF]	–	0.18 ± 0.12
R_ϕ [MΩ]	–	3.06 ± 3.21
C_i [pF]	54.79 ± 8.40	18.66 ± 0.55
$\lvert Z \rvert$(1 kHz) [kΩ]	175.91 ± 12.24	236.83 ± 23.54
n_e	8	8

4.3.4 Summary

We performed EIS on Pt, TiN, IrO_x, and CNT electrodes of 50, 25, 10, and 5 μm diameter in PBS. The impedance at 1 kHz was up to 3 orders of magnitude lower for the CNT electrodes compared to the other electrode materials. This was partly attributed to the large distributed surface area and hence capacitance (CPE) of the CNTs. Additional pseudocapacitive properties of the CNTs due to the presence of O-containing functional groups significantly contributed to the observed low impedance. Further, the CNT electrodes gave rise to the lowest R_{ct} and hence fastest reaction kinetics. Although not evidently beneficial for neural stimulation, this property may prove essential if CNTs are also used as a sensor material for the *in vivo* monitoring of neurochemicals. Hybrid implantable microsystems combining high-density neuroelectrical and neurochemical functionalities on one platform would greatly improve the understanding of neural communication. Finally, the influence of BSA adsorption on the impedance of Pt electrodes was studied. Only a minimal impedance increase was observed, which is unlikely to deteriorate the recording capability of the electrodes *in vivo*.

4.4 Coulometric Reciprocal Derivative Chronopotentiometry (RDC) of Pt Electrodes

4.4.1 Background

Various experimental methods have been proposed to determine the safe limits of neural stimulation under realistic conditions. As already pointed out in Section 2.4.3, charge-storage densities determined by CV are not reliable because they are based

on signal-shapes and time-scales, which do not represent an actual stimulation waveform. Not to mention, CV is performed in potentiostatic mode, while neural stimulation generally employs current pulses.

Two characterization methods are reported in literature: the first is simply termed the *voltage transient* technique[77,152,239,240,171], and the second is the *voltage-clamp* method. In the first, the electrode potential is measured in response to applied biphasic current pulses. Stimulation is considered safe when the electrode potential remains within the limits of water hydrolysis. These limits are assumed to correspond to the potentials for H_2 and O_2 evolution obtained with CV. This assumption, however, does not take into account that CV sweep rates generally are less than 0.1 V/s, while the electrode potential during current stimulation can change nonlinearly at rates higher than 1 kV/s. Such high rates can be accompanied by appreciable activation overpotentials depending on the nature and kinetics of the underlying redox processes. This technique is hence only applicable to those systems, which clearly behave kinetically reversible even at high voltage sweep rates, i.e. where the electrode potential does not depend on the sweep rate. Such information is not a priori available for electrode materials.

The *voltage-clamp* technique introduced by Bonner[241] involves applying a monophasic cathodic current pulse to an electrode. At the end of the pulse, the electrode potential is clamped back to its pre-pulse value[78,242,243,166]. The charge flowing within the 20 ms after switching to voltage clamp is the reversibly recoverable charge; any further flow of charge is considered irreversible or lost. With this method only monophasic current pulses can be studied, which has only limited value for neural stimulation.

In this work, we propose an alternative method based on RDC and coulometric analysis. Chronopotentiometry is a standard electroanalytical method that involves applying a constant current density, i, between the electrode under study (=WE) and a CE while measuring the transient electrode potential, $E(t)$, with respect to a RE.[244] When a system that is initially at equilibrium is subjected to an anodic current, the electrode potential shifts rapidly in the positive direction due to charging of the EDL. This shift continues until the potential is reached where an oxidation of an electroactive species at the interface takes place. Considering the ideal case of a reversible redox reaction of the form $\mathrm{R} \rightleftharpoons \mathrm{O} + \mathrm{ze}^-$, when applying an anodic current, the substance R will be oxidized and its concentration at the electrode surface will drop, while the concentration of O will rise. The resulting $E(t)$ response is obtained with the Nernst equation (Eq. 2.36) where $c_R(0,t)$ and $c_O(0,t)$ are solved using the time-dependent diffusion equation (Fick's second law).

Analytical solutions have been derived by Sand [245]:

$$c_R(0,t) = c_R^* - \frac{2i}{zF}\sqrt{\left(\frac{1}{\pi D_R}\right)t} \tag{4.22}$$

$$c_O(0,t) = c_O^* + \frac{2i}{zF}\sqrt{\left(\frac{1}{\pi D_O}\right)t} \tag{4.23}$$

With the substitution

$$P_{R/O} = \frac{2i}{zF}\sqrt{\left(\frac{1}{\pi D_{R/O}}\right)} \tag{4.24}$$

the Nernst equation will take the form:

$$E(t) = E^\circ + \frac{RT}{zF}\ln\frac{c_O^* + P_O t^{1/2}}{c_R^* - P_R t^{1/2}} \tag{4.25}$$

Fig. 4.11a shows the theoretical $E(t)$ transient in response to an anodic current density, i_A. With time, $E(t)$ increases because substance R gradually becomes depleted at the electrode surface. The standard electrode potential, E^0, is reached when $c_R(0,t) = c_O(0,t)$. Eventually, the electrode surface becomes depleted of substance R, and diffusion is insufficient to supply sufficient reactant to satisfy the imposed current density. At this point (the transition time, τ_A), the current is almost solely consumed to charge the EDL, and the potential shifts rapidly to a value where another redox reaction becomes more favorable (not shown).

If a cathodic current density of equal magnitude, $i_C = -i_A$, is applied at $t = \tau_A$, substance O will be reduced so that a cathodic transition time, τ_C, is recorded (Fig. 4.11b). If $\tau_C = \tau_A$, the same amount of charge has been transferred during the reduction and oxidation reaction and the redox system has returned to its initial state. If, however, substance O diffuses away prior to current reversal, there will be less charge-transfer on account of the reduction reaction compared to the oxidation reaction and hence $\tau_C' < \tau_A$.[246] Preventing $\tau_C' < \tau_A$ is essential to ensure safe neural stimulation. One may define an initial anodic state A and a corresponding cathodic state C at the end of the cathodic transient. These corresponding cathodic and anodic states (CCAS) are marked in Fig. 4.11.

In practice, one cannot precisely identify the transition times in an $E(t)$ trace because reactions may occur in parallel and capacitive charging due to the EDL, oxide films, and adsorbates may obscure the transition times. By plotting the reciprocal time derivative of the electrode potential, dt/dE, vs. E, one can improve the resolution and allow identification of the transition times. This method, called RDC, has been used in electrochemical analysis for theoretical and experimental studies of various electrode processes [247–254].

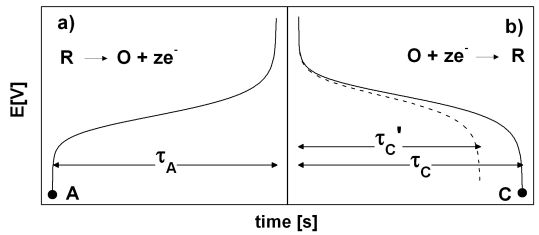

Fig. 4.11: Theoretical $E(t)$ transients of a reversible redox system in response to (a) anodic (oxidation) and (b) cathodic (reduction) current densities of equal magnitude. The transition times, τ_A and τ_C, represent the times until the electrode surface becomes depleted of R and O, respectively. The case, where the same amount of charge is transferred in both reactions corresponds to $\tau_A = \tau_C$. If unequal amounts of charge are transferred due to diffusional loss of substance O at the end of τ_A, the transition time of the oxidation reaction will decrease, $\tau'_C < \tau_A$. Indicated are the corresponding anodic (A) and cathodic (C) states of the $E(t)$ transients.

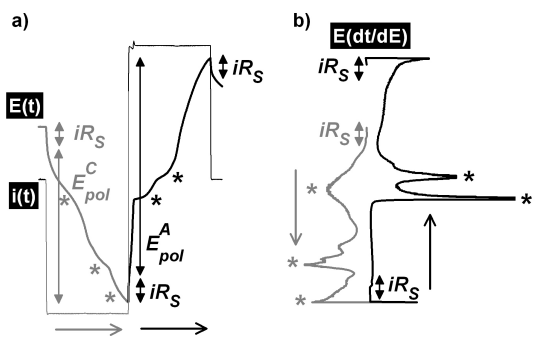

Fig. 4.12: (a) Typical voltage transient, $E(t)$, of a Pt electrode measured in response to a biphasic, symmetric current pulse, $i(t)$. (b) Corresponding reciprocal derivative of the voltage transient. Here we plot $E(dt/dE)$ for better comparison to the $E(t)$ transient in (a). Indicated are the graph segments related to the iR_s drop. Faradaic reactions are marked with $*$ in both curves. Open arrows point in the logic direction of each curve.

Fig. 4.12 shows a typical $E(t)$ transient (a) and corresponding RDC curve (b) measured with a Pt electrode in response to a biphasic, symmetric current pulse. Open arrows point in the logic direction of each curve. Each of the $*$-marked inflections in the $E(t)$ curve arises due to a redox reaction similar to the one in Fig. 4.11, and has a corresponding peak in the RDC curve. The RDC plot clearly reveals much more details about the different electrode processes than the $E(t)$ transient. Also indicated are the ohmic interface polarization, iR_s, which occurs at each current step due to the solution and metal resistances, and E_{pol}^{C} and E_{pol}^{A}, the cathodic and anodic electrode polarization, respectively, representing the combined effects from the double-layer, charge-transfer, diffusion, and pseudocapacitance.

For neural stimulation, one in particular wishes to avoid gas evolution at the end of each phase. Gas evolution is accompanied by diffusion of gas molecules from the electrode site. Inspired by the concept of transition times, such a loss of charge could be detected if appropriate CCAS could be identified in the measured RDC curve in Fig. 4.12b. Although most redox reactions occurring under realistic stimulation conditions are not considered to be kinetically reversible as assumed for the formalism above (Eqs. 4.22–4.25), the principle of transition times still holds [245]. The transition time is related to the concentration of the species that is consumed at the electrode through: [246]

$$\tau = \frac{z^2 F^2 \mathcal{A} {c^*}^2 \pi D}{4i} \tag{4.26}$$

where $\mathcal{A}$ is the electrode area. The above equation is valid for electrochemically reversible and irreversible reactions [245].

In order to determine the CCAS, one has to first identify the nature of the redox reactions in the RDC curve. This problem becomes largely simplified by knowing that the RDC response presents a behavior qualitatively similar to the voltammetric $i(E)$ response [255]. For reversible electrode processes, the square root of the peak amplitude in RDC is a linear function of the reactant concentration [255]:

$$y_P^{1/2} \propto \frac{z^{3/2} D^{1/2} c^*}{i} \tag{4.27}$$

This is an almost equivalent expression as for the peak height, i_P, in CV:

$$i_P \propto z^{3/2} D^{1/2} c^* v^{1/2} \tag{4.28}$$

where $1/i$ in Eq. 4.27 has been replaced by the square root of the scan rate $v^{1/2}$. This shows that CV conveys qualitatively similar information as RDC [255] and can hence be employed as a means to interpret RDC data.

Fig. 4.13a shows a CV curve recorded with a Pt electrode. Analog to Fig. 4.11, the CCAS are points prior and after a specific redox reaction, which, in this case, is the adsorption/desorption of H atoms on platinum (cf. Section 4.2.3). One can identify

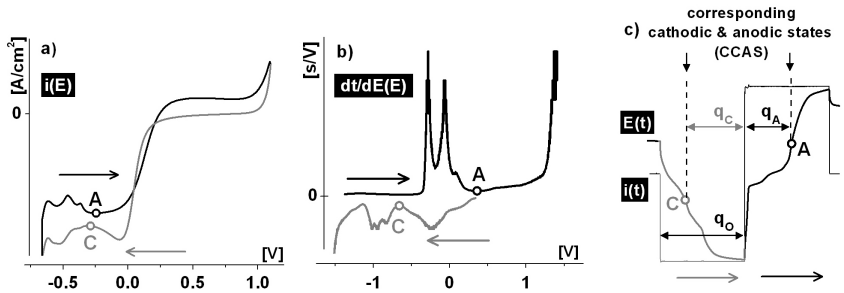

Fig. 4.13: (a) Typical voltammogram of a 50 μm diameter Pt electrode measured in PBS at 0.1 V/s. Indicated are the corresponding cathodic (C) and anodic (A) states (CCAS). (b) $dt/dE(E)$ plot with CCAS obtained with a Pt electrode in response to a biphasic current pulse. (c) Corresponding voltage transient, $E(t)$, and current pulse, $i(t)$, with applied charge density, q_0. Indicated are the cathodic and anodic charge densities, q_C and q_A, respectively, consumed between the two CCAS. Open arrows point in the logic direction of each curve.

these CCAS also in the RDC plot (Fig. 4.13b) by visually comparing with the CV curve. Introducing these CCAS into the original $E(t)$ transient in Fig. 4.13c, where H_2 evolution was assumed to occur at the end of the cathodic phase, one can indeed see that the anodic charge density, $q_A = i\tau_A$, is smaller than the cathodic one, $q_C = i\tau_C$ and hence clearly indicates the occurrence of some charge loss during the first phase. Combining RDC with the coulometric analysis of q_C and q_A therefore provides a means to clearly identify the onset of chemically irreversible reactions occurring under realistic stimulation conditions.

4.4.2 Materials and Methods

Measurements were performed with 50 μm diameter Pt electrodes in PBS, PBS-BSA, and PBS_{deox} using an Autolab PSTAT302N potentiostat controlled by the NOVA software (Ecochemie, The Netherlands). Chronopotentiometry required an additional AD converter (ADC10M, Ecochemie, The Netherlands) for high-speed sampling at 250 kHz. Data analysis was performed in OriginPro 8.5. For all chronopotentiometric experiments, 50 successive current pulses were applied. For data analysis, the 50th pulse was examined. In each buffer solution, the influence of the pulse polarity (AF or CF), the pulse width, and pulse amplitude were investigated. All experiments were performed with successively increasing charge densities.

For measurements in PBS and PBS_{deox}, the electrodes were conditioned by potential cycling prior to applying the current pulses in order to establish a clean electrode

surface and minimize possible memory effects due to previous charge densities. Settings for the CV were: 10 cycles between -0.9 V and 1.1 V at a scan rate of 2 V/s. The initial scan direction was either anodic or cathodic depending on whether AF or CF pulses were applied afterwards. When stimulating with a constant pulse amplitude (CPA), symmetric current pulses with a peak-to-peak amplitude of 20 μA were used. The phase width varied between 200–4000 μs, corresponding to charge densities, q_0, ranging from 0.10–2.03 mC/cm^2 (geometric electrode area). When pulsing with a constant pulse width (CPW), symmetric current pulses with a phase width of 400 μs and varying amplitudes 5–100 μA were used. The charge densities also ranged from 0.10–2.03 mC/cm^2. For all experiments, the inter-pulse interval was 9.1 ms, resulting in pulsing frequencies ranging from 83 Hz for longest to 105 Hz for shortest pulses. No electrode pre-conditioning was performed in PBS-BSA because this would have led to desorption of the protein film. Otherwise, the stimulation sequences were the same as in PBS and PBS$_{\mathrm{deox}}$.

In addition, we also performed initial experiments with 50 μm diameter TiN and 25 μm diameter CNT electrodes in PBS. The electrodes were subjected to AF-CPW stimulation using the same pulse parameters and stimulation sequence as above, but with different q_0 ranges. For the TiN electrode, we applied 1.12–10.50 mC/cm^2, and for the CNT electrode, 40.74–317.80 mC/cm^2.

4.4.3 Results

Influence of Albumin Adsorption

This section describes and compares the RDC results obtained in PBS and PBS-BSA. The graphical interpretation strongly benefits from the CV analysis performed in PBS and PBS-BSA (cf. Section 4.2.3). Fig. 4.14 shows two exemplary RDC data sets obtained with CF-CPA and AF-CPA stimulation in PBS and PBS-BSA. In each case, only a selection of all investigated charge densities is plotted. Throughout the discussion, the charge density values, q_0, q_C, and q_A, are referred to in terms of their absolute values related to the geometric electrode area. The polarities are implicit by the annotations CF (negative) and AF (positive) for q_0 and the subscripts, C (negative) and A (positive) for q_C and q_A, respectively. For better clarity, the iR_s drop is excluded from the plots. The observations for CPA stimulation also apply to a large extent to CPW stimulation (Appendix C, Fig. C.1). Differences are mentioned where required.

Similar to CV (Fig. 4.5), Pt-specific electrode reactions can be identified in the RDC graphs. Anodic features include H_2 oxidation (Eq. 4.3), phosphate protonation (Eq. 4.4), and H desorption (Eqs. 4.2) (H2O/PHP/HD); further, Pt oxidation (Eq. 4.5) and BSA oxidation (Eq. 4.14) (PO/AO), and, finally, Pt dissolution (Eq. 4.8) and O_2 evolution (Eq. 4.6) (PD/O2E). The narrow reductive peak at

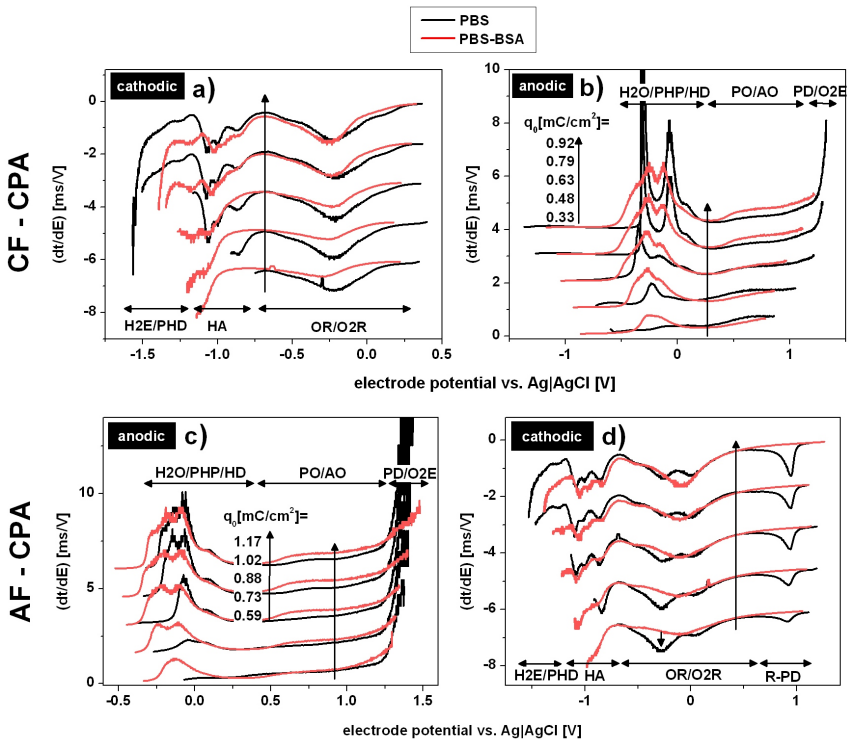

Fig. 4.14: Series of $dt/dE(E)$ plots obtained in response to constant pulse amplitude (CPA) stimulation of a 50 μm diameter Pt electrode in PBS and PBS-BSA. (a, b) Cathodic-first (CF) stimulation; (c, d) anodic-first (AF) stimulation. Only a selection of all applied (absolute) charge densities, q_0, is shown. Graphs are stacked by a constant offset. Regions of Pt-specific reactivity are indicated by horizontal arrows. Long vertical arrows point in the direction of increasing q_0. The short vertical arrow in (d) marks the peak identified as O_2 reduction.

the beginning of the cathodic phase of AF stimulation in PBS is assigned to the reduction of Pt dissolution products (Eq. 4.8) (R-PD). Results supporting this conclusion come from voltammetric measurements of Pt microelectrodes performed in PBS solution using an extended voltage range [209] and from own RDC measurements in PBS with a higher Cl^- concentration (0.3 M NaCl) (Appendix C, Fig. C.3).

Furthermore, a broad cathodic band with multiple shoulders is assigned to the reduction of dissolved O_2 and Pt oxide (O2R/OR) (Eqs. 4.1 and 4.5). Hydrogen adsorption (HA) (Eq. 4.2), phosphate deprotonation and H_2 evolution (PHD/H2E) (Eqs. 4.4 and 4.3) occurred at the end of the cathodic phase. Unlike CV, no distinct cathodic feature can be associated to PHD. Because the product of phosphate deprotonation is H_2, both H2E and PHD signals are grouped together. A pronounced flat region at the beginning of the anodic phase of CF stimulation is related to the (dis-)charging of the double-layer capacitance. In the following, the results of CF and AF stimulation will be discussed in detail.

Cathodic-First Stimulation In PBS-BSA, peaks for H adsorption and desorption appear at lower charge densities (q_0 <0.3 mC/cm^2) than in PBS. Furthermore, for charge densities <0.7 mC/cm^2, the OR/O2R signal is inhibited in PBS-BSA. Both observations are interrelated. Due to the inhibitory effect of BSA, less charge is consumed by Pt oxidation and reduction than in PBS. The unconsumed excess charge is redistributed to the subsequent H adsorption, which consequently manifests at lower q_0 values than in PBS. Similar to the observations with CV, H adsorption and desorption peaks are less pronounced in PBS-BSA. In addition, the H2E/PHD signal in PBS-BSA is larger than in PBS, which may be due to a higher rate of PHD in the presence of the negatively charged BSA.

It is also determined that the H_2 evolved in PBS is partly reoxidized in the subsequent anodic phase, which is not evident in PBS-BSA. In PBS, the peak amplitudes in the H2O/PHP/HD region increases strongly with q_0, whereas the amplitudes in PBS-BSA shows less dependence on q_0. Because the peak amplitude in RDC scales linearly with the squared reactant concentration (cf. Eq. 4.27), and the theoretical H adsorption/desorption capacity of Pt is limited to $\approx 210\,\mu$C/cm^2 [?], the increasing H2O/PHP/HD peak amplitudes in PBS can only be explained by an increased availability of oxidizable H_2. For $q_0 < 0.7$ mC/cm^2, the PO/AO signal in the anodic phase is smaller in PBS-BSA, confirming the inhibition of Pt oxide formation observed also with CV. On the other hand, the same signal becomes larger in PBS-BSA for higher charge densities, which can be attributed to BSA oxidation.

Anodic-First Stimulation H adsorption and desorption peaks in PBS-BSA appear at lower charge densities ($q_0 < 0.6$ mC/cm^2) than in PBS. As with CV, an increased

anodic PO/AO signal for PBS-BSA can be attributed to BSA oxidation. The presence of BSA also suppresses the PD/O2E wave at the end of the anodic phase. A narrow reductive peak (R-PD) is observed at the beginning of the cathodic phase at around 1 V. The R-PD peak is absent in the presence of BSA. The OR/O2R signal in PBS-BSA is partly inhibited for $q_0 < 1.0\,\mathrm{mC/cm^2}$ ($q_0 < 1.3\,\mathrm{mC/cm^2}$ for CPW stimulation; Appendix C, Fig. C.1). Noticeable is that AF stimulation in PBS gives rise to a OR/O2R signal consisting of two peaks, while only one broad peak with multiple shoulders is seen with CF stimulation.

The above observations allow the following conclusions: The adsorption of BSA on Pt electrodes inhibits the formation and reduction of surface oxides by blocking reactive sites[194,198], a process that competes with Cl^- adsorption from PBS[211]. Chloride anions are depleted from the electrode surface due to electrostatic repulsion by the net negative charge of adsorbed BSA molecules. Consequently, Pt corrosion and thus the PD/O2E and R-PD signals are suppressed. These findings are in agreement with previous studies that showed inhibition of Pt dissolution by adsorption of human serum albumin.[200,256]

Influence of Dissolved Oxygen

In Fig. 4.15, RDC graphs obtained with CPA stimulation in PBS and PBS_{deox} are compared. The discussion of the results will be restricted to CPA stimulation, but is equally valid for CPW stimulation (Appendix C, Fig. C.2). As expected, deoxygenation has a pronounced effect on the cathodic OR/O2R signal (Fig. 4.15a, d). Similar to the CV in Fig. 4.6b, one of the two OR/O2R shoulders seen with AF stimulation in PBS (small arrow in Fig. 4.15d) is consistently suppressed in PBS_{deox} (marked with a small vertical arrow), and is hence assigned to the reduction of dissolved O_2. At this point we may point out that the same signal was also suppressed in PBS-BSA (Fig. 4.14d). Thus, BSA adsorption impedes O_2 reduction, which has also been suggested by Cogan[81]. The reduction of O_2 in the presence of adsorbed BSA is kinetically inhibited due to blocked reactive sites on the Pt surface. The allocation of O_2 reduction in the case of CF stimulation in PBS was less conclusive. Furthermore, because less charge is consumed by O_2 reduction in PBS_{deox}, more charge becomes available for subsequent electrode processes, such as HA, H2E/PHD, and H2O/PHP/HD, which appeared at lower charge densities in PBS_{deox} than in PBS for both CF and AF stimulation.

Coulometric Analysis

As pointed out earlier in Section 4.2, by combining RDC with the coulometric analysis of q_C and q_A it is possible to determine the onset of chemically irreversible redox reactions occurring under realistic stimulation conditions. The theoretical

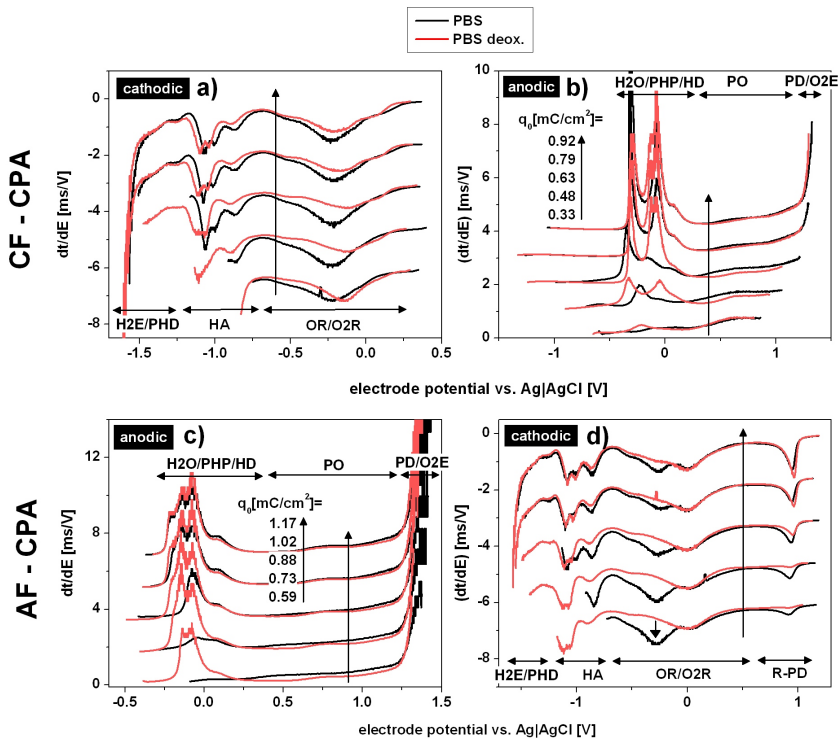

Fig. 4.15: Series of $dt/dE(E)$ plots obtained in response to constant pulse amplitude (CPA) stimulation of a 50 μm diameter Pt electrode in PBS and PBS_{deox}. (a, b) Cathodic-first (CF) stimulation; (c, d) anodic-first (AF) stimulation. Only a selection of all applied (absolute) charge densities, q_0, is shown. Graphs are stacked by a constant offset. Regions of Pt-specific reactivity are indicated by horizontal arrows. Long vertical arrows point in the direction of increasing q_0. The short vertical arrow in (d) marks the peak identified as O_2 reduction.

premise is that $q_C = q_A$ when no chemically irreversible reactions occur, and $q_C \neq q_A$ when such reactions take place. This needs a slight revision though. The consumed charge densities, q_C and q_A, are not entirely faradaic in nature. The charging of the double-layer capacitance also consumes some of the constant charge density applied during stimulation. We can take this into account by writing:

$$q_{C/A} = q_{dl,C/A} + q_{f,C/A} \tag{4.29}$$

with dl and f indicating double-layer and faradaic contributions, respectively (cf. Eq.2.44). For a perfectly symmetric system, i.e. equal faradaic charge densities, $q_{f,C} = q_{f,A}$, and equal capacitive contributions, $q_{dl,C} = q_{dl,A}$, we obtain $q_C = q_A$. However, because dE/dt changes throughout the $E(t)$ transient, there is always a varying capacitive current, $i_{dl} = C_{dl}(dE/dt)$, which can differ for the cathodic and anodic phase and hence $q_{dl,C} \neq q_{dl,A}$. Hence, even for chemically reversible faradaic reactions, the situation $q_C \neq q_A$ can occur on account of unequal capacitive charging. If, e.g. during CF pulsing, H_2 evolves at the end of the cathodic phase, and H_2 molecules diffuse away from the electrode, the consequence will be an imbalance $q_{f,C} > q_{f,A}$, which increases with increasing q_0. Eventually, this faradaic imbalance will exceed the capacitive mismatch causing q_C to increase at a faster rate than q_A. One will hence observe a clear divergence of q_C and q_A once chemically irreversible hydrolysis occurs. Similar considerations also apply for AF pulsing. Here, q_A would become larger than q_C when charge is lost due to O_2 evolution.

As CCAS we introduced the points prior to H adsorption and after H desorption (Fig. 4.13a, b). Thus, in the case of CF stimulation, q_C and q_A correspond to the amount of charge consumed by HA/PHD/H2E and H2O/PHP/HD, respectively, while for AF stimulation, q_A and q_C reflect the amount of charge consumed by PO/AO/PD/O2E and R-PD/OR/O2R, respectively. Fig. 4.16 shows the q_C and q_A (left column) and corresponding normalized charge densities, $q_C^0 = q_C/q_0$ and $q_A^0 = q_A/q_0$ (right column) for all four stimulation conditions in PBS and PBS-BSA. The same is also displayed for PBS versus PBS_{deox} in Fig. 4.17. At low values of q_0, the CCAS are not yet present; thus no q_C and q_A can be determined.

For all stimulation conditions and buffer solutions, corresponding q_C and q_A values initially show a similar q_0-dependence until they begin to diverge (Fig. 4.16 and Fig. 4.17, left column). At this diverging point, the consumed charge density of the first phase starts to increase at a faster rate (parallel to q_0) than that of the second phase. This behavior corresponds well to the theoretical prediction for the onset of chemically irreversible gas evolution. At the point of divergence, q_A^0 becomes minimal for CF and maximal for AF stimulation, as indicated by vertical solid lines for PBS and dashed lines for PBS-BSA and PBS_{deox}, respectively (Fig. 4.16 and Fig. 4.17, right column). Thus, the point of divergence marks the onset of chemically irreversible H_2 and O_2 evolution for CF and AF stimulation, respectively.

The case of $q_A = q_C$ prior to divergence is only observed for AF-CPA stimulation in PBS (Fig. 4.16g). Such a situation is expected for a perfectly symmetric system with

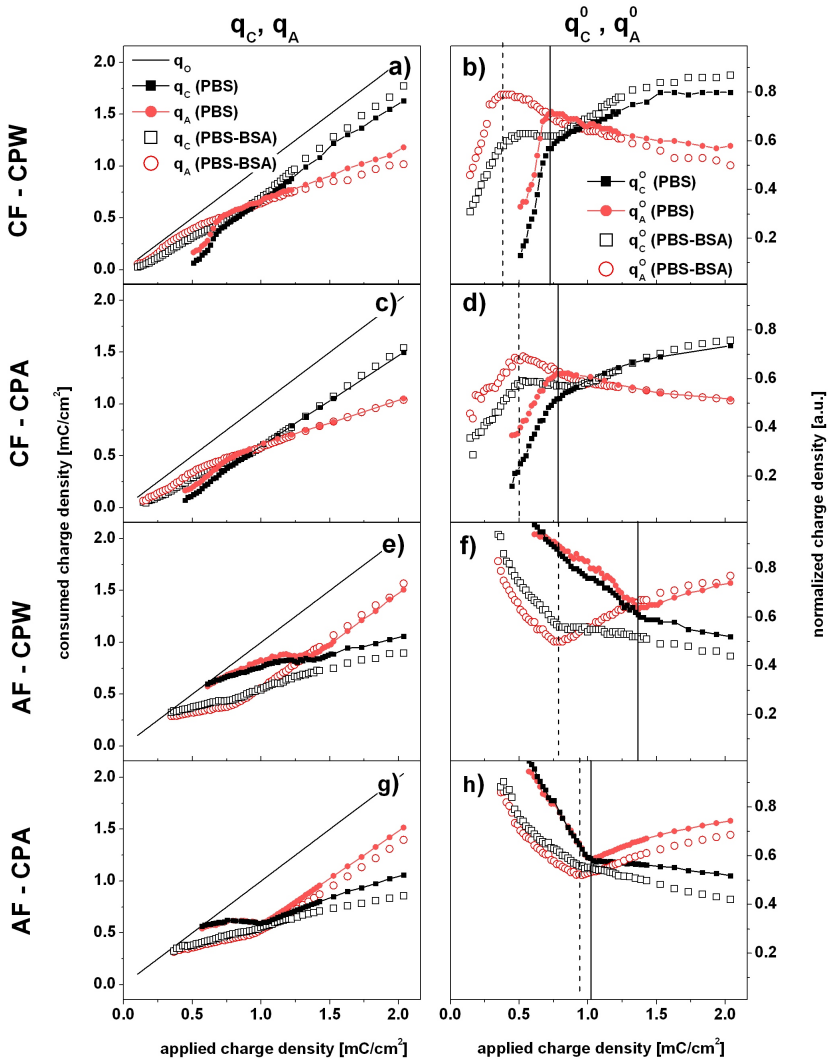

Fig. 4.16: (a, c, e, g) Consumed charge densities, q_C and q_A, vs. applied charge density, q_0, for cathodic-first (CF) and anodic-first (AF) stimulation with a constant pulse width (CPW) and amplitude (CPA) in PBS and PBS-BSA. (b, d, f, h) Corresponding normalized charge densities, $q_C^0 = q_C/q_0$ and $q_A^0 = q_A/q_0$. Solid and dashed vertical lines mark the onset of chemically irreversible gas evolution in PBS and PBS-BSA, respectively.

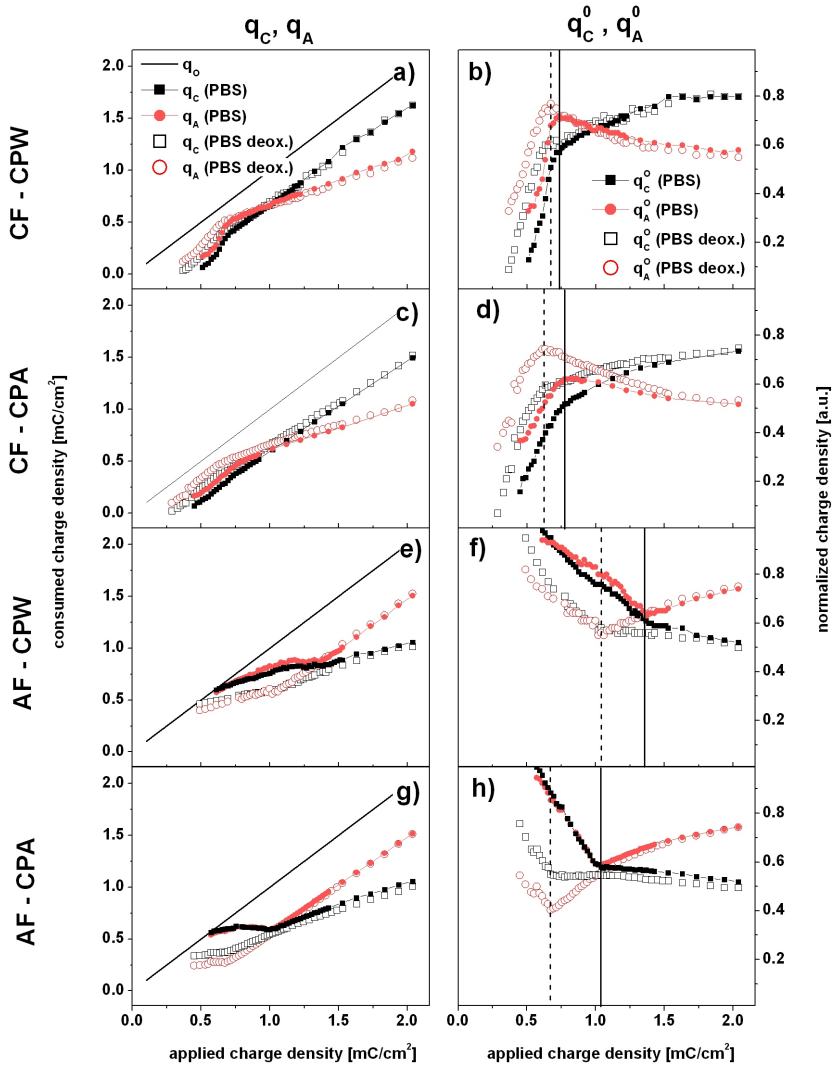

Fig. 4.17: (a, c , e, g) Consumed charge densities, q_C and q_A, vs. applied charge density, q_0, for cathodic-first (CF) and anodic-first (AF) stimulation with a constant pulse width (CPW) and amplitude (CPA) in PBS and $\mathrm{PBS_{deox}}$. (b, d, f, h) Corresponding normalized charge densities, q_C^0 and q_A^0. Solid and dashed vertical lines mark the onset of chemically irreversible gas evolution in PBS and $\mathrm{PBS_{deox}}$, respectively.

$\Delta q_f = 0$ and $\Delta q_{dl} = 0$. However, the same measurement in PBS_{deox} (Fig. 4.17g) reveals an offset $q_A < q_C$ prior to divergence. Because chemically irreversible O_2 reduction occurs to a larger extent in PBS than in PBS_{deox}, $q_A = q_C$ in the former case does not necessarily imply $q_{f,A} = q_{f,C}$.

In fact, in most cases, a rather constant offset between corresponding q_C and q_A values was observed prior to divergence, with the charge density of the second phase being larger than that of the first phase. In general, this offset was slightly larger in PBS_{deox} than in PBS, serving as an evidence for the irreversible nature of O_2 reduction. This initial offset may be due to $\Delta q_{dl,C/A} \neq 0$ as pointed out earlier. Also, the double layer capacitance, C_{dl}, is treated as constant, but is, in fact, bias-dependent (cf. Eq. 2.23) and may therefore differ in the two phases of the pulse. Furthermore, *chemical* modifications of the electrode surface by adsorption of impurities and/or oxidation can alter the electrode activity and thus change the rates at which reactions occur in the cathodic and anodic phase. Consequently, the graphically determined CCAS may not represent 100% (electro-)chemically corresponding states of the electrode surface, which may result in unequal q_C and q_A values prior to gas evolution. The offset may also be caused by undefined chemically irreversible reactions. This, however, would imply that such reactions commence at rather low applied charge densities, which is quite unlikely.

Only for AF-CPW stimulation in PBS (Fig. 4.16e, f) does the charge density of the first phase increasing at a faster rate than that of the second causing $q_A > q_C$ prior to the minimum of q_A^0. The absence of such an initial divergence in PBS-BSA indicates that its origin may either be chemically irreversible Pt dissolution or Pt oxidation, which are both suppressed in PBS-BSA. Preliminary RDC experiments in PBS with a higher Cl^- concentration and hence Pt dissolution rate also result in a stronger initial divergence than in physiological PBS (Appendix C, Fig. C.4).

Table 4.5 summarizes the q_0 values at the minimum/maximum of q_A^0 averaged over n_e experiments with n_e different electrodes for each stimulation condition. The tabulated values indicate that the onset of chemically irreversible gas evolution depends strongly on the buffer solution and occurs on average at 10–46% and 13–24% lower charge densities in PBS-BSA and PBS_{deox}, respectively, compared to PBS. In the case of PBS-BSA, the decrease can be explained by the inhibition of Pt oxidation and Pt dissolution, as well as Pt oxide and O_2 reduction due to the adsorbed BSA. For CF stimulation in PBS-BSA, enhanced phosphate deprotonation may also lead to a higher H_2 evolution rate, which shifts the maximum of q_A^0 towards lower q_0 values. Overall, gas evolution in PBS-BSA occurs with less injected charge than on a clean surface. As a consequence, q_C and q_A and, therefore, the minimum/maximum of q_A^0 are shifted towards lower q_0 values in PBS-BSA. This shift is less pronounced for AF-CPA stimulation (Fig. 4.16h) and may be caused by the increased desorption of BSA when longer pulses are applied, resulting in the dominance of the clean Pt behavior.

Table 4.5: Average charge densities at the onset of chemically irreversible gas evolution.

pulse polarity	solution	pulse type	charge density [mC/cm^2]	n_e
Test Chip				
CF	PBS	CPW	0.74 ± 0.06	4
		CPA	0.81 ± 0.11	4
	PBS+BSA	CPW	0.41 ± 0.03	4
		CPA	0.56 ± 0.04	2
	PBS_{deox}	CPW	0.65 ± 0.00	2
		CPA	0.66 ± 0.04	2
AF	PBS	CPW	1.34 ± 0.06	3
		CPA	1.03 ± 0.01	2
	PBS+BSA	CPW	0.80 ± 0.03	3
		CPA	0.94 ± 0.03	2
	PBS_{deox}	CPW	1.02 ± 0.03	2
		CPA	0.78 ± 0.15	2
Neural Probe				
CF	PBS	CPW	0.69	–

The 13–24% lower charge densities in PBS_{deox} (Table 4.5) compared to PBS are the consequence of the decreased availability of reducible O_2. In Section 4.2.3 we estimated that deoxygenation reduces the dissolved O_2 concentration by 188 μM. Therefore, the contribution of O_2 reduction at the O_2 levels found in the brain (5.9–93 μM, cf. Section 4.2.3) must account for 0.4–12% of the total injected charge if the reaction scales linearly with the concentration. Taking into account that O_2 reduction appears to be inhibited in the presence of BSA, it is expected that O_2 reduction will contribute even less to charge injection *in vivo*. In comparison, O_2 reduction in PBS (269 μM) consumes 19–34% of the total injected charge. Although O_2 reduction has been postulated as a possible cause for tissue injury during neural stimulation, it is unclear whether and at which levels O_2 reduction will become physiologically harmful.

The pulse type-dependence of gas evolution is strongest for AF stimulation in PBS. Here, O_2 evolves at much higher applied charge densities with CPW than with CPA stimulation. This is also seen with stimulation in PBS_{deox} but to a lesser extent. Coulometric analysis suggests that Pt dissolution in PBS occurs at a higher rate with AF-CPW than with AF-CPA stimulation (see also Appendix C, Fig. C.4). While it appears that for AF-CPA stimulation pulses are long enough to reverse most of the dissolution products, AF-CPW stimulation is more prone to charge loss due to irreversible Pt dissolution. This may explain why the onset of O_2 evolution shifts towards higher q_0 values in the latter case. No coulometric evidence for Pt dissolution was found with AF stimulation in PBS-BSA, confirming our findings

in Section 4.2.3. The influence of the pulse type was also seen for CF and AF stimulation in PBS-BSA. In both cases, gas evolved at higher charge densities with CPA stimulation compared to CPW stimulation. This is likely due to an increased BSA desorption with longer pulse widths, which shifts the onset of gas evolution closer to the values found in PBS.

4.4.4 Applying RDC to other Electrode Materials

Coulometric RDC was shown to be a reliable approach to identify chemically irreversible reactions occurring at Pt electrodes. However, Pt is not considered to be the electrode material of choice for stimulation at cellular and sub-cellular resolutions because it cannot safely supply sufficient charge to activate neural tissue. The question one has to answer is therefore, whether RDC can also be applied to study more promising materials such as TiN, IrO_x, and CNTs. The answer is yes and no. Coulometric RDC analysis is restricted to those materials with faradaic processes occuring during stimulation and where one can identify CCAS. Clearly, this is the case for IrO_x. However, because of the instability of the IrO_x leading to crack formation under stimulation similar as in Fig. 4.3, it was not possible to obtain reliable RDC measurements. On the other hand, for electrode materials, which operate largely by the capacitive charging of the double-layer and where faradaic charge-transfer is only moderately present, such as TiN and CNTs, the coulometric approach is not applicable.

Fig. 4.18 shows two RDC data sets obtained with CF-CPW stimulation of a TiN and CNT electrode of 50 and 25 μm diameter, respectively. The TiN electrode exhibits one well-defined peak in the cathodic phase, which in analogy to the respective CV plot in Fig. 4.2b may be attributed to H adsorption. The band at the very beginning of the anodic phase may then be assigned to H desorption. With increasing q_0, this band transforms into a sharp peak possibly related to H_2 oxidation and, eventually, disappears as a steep slope. The anodic phase is furthermore characterized by a long flat capacitive region, and similar to the CV in Fig. 4.2b is probably caused by a passivating oxide or oxynitride on the TiN surface. The onset of O_2 evolution could not be detected within the voltage range of the potentiostat. With such a capacitive behavior it is impossible do identify CCAS. The corresponding $E(t)$ transient is shown in Fig. 4.19a. Noteworthy is the long capacitive decay after the anodic phase.

The CNT electrode gives rise to similarly featureless and capacitive RDC graphs. Unlike TiN, however, there is a steep signal increase at the end of each phase related to H_2 and O_2 evolution, which are then estimated to occur at approx. 100 and 210 mC/cm^2, respectively. The corresponding $E(t)$ transient is shown in Fig. 4.19b. No capacitive decay occurs at the end of the anodic phase.

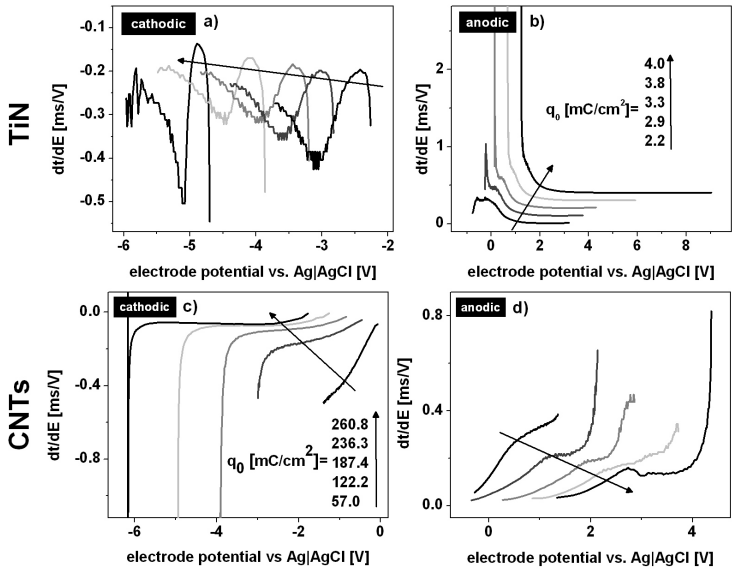

Fig. 4.18: Series of $dt/dE(E)$ plots obtained with a (a) 50 μm diameter TiN electrode and (b) 25 μm diameter CNT electrode in PBS with cathodic-first (CF) stimulation at a constant pulse width (CPW). Arrows point in the direction of increasing q_0.

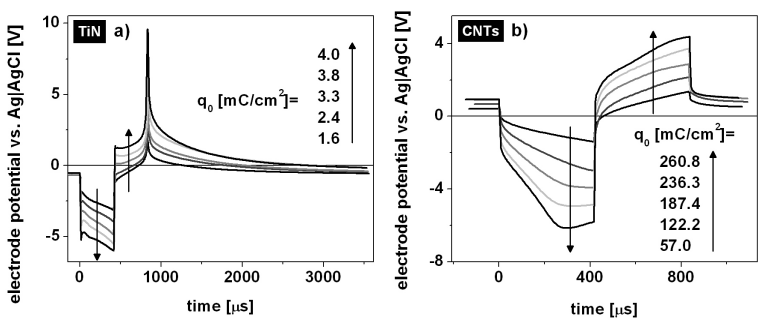

Fig. 4.19: Series of $E(t)$ transients recorded in PBS with a (a) 50 μm diameter TiN electrode and (b) 25 μm diameter CNT electrode in response to cathodic-first stimulation at a constant pulse width of 400 μs. Long arrows point in the direction of increasing q_0.

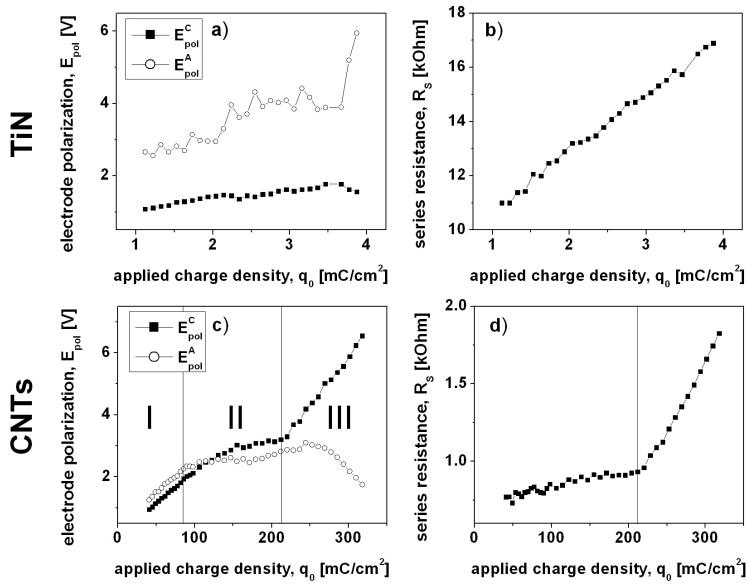

Fig. 4.20: Absolute cathodic and anodic electrode polarizations, E^C_{pol} and E^A_{pol}, respectively, for a (a) 50 μm diameter TiN and (c) 25 μm diameter CNT electrode obtained in response to cathodic-first stimulation of increasing charge density, q_0, with a constant pulse width of 400 μs in PBS. Series resistance, R_s, of the (b) 50 μm diameter TiN and (d) 25 μm diameter CNT electrode.

For both materials, the coulometric approach cannot be applied. There are, however, alternative parameters that may be evaluated in order to obtain further information about the onset of gas evolution at such capacitive electrodes. There is the ohmic polarization, iR_s (determined at the point of current reversal), and the cathodic and anodic interface polarizations, E^C_{pol} and E^A_{pol}, respectively (Fig. 4.12). Fig. 4.20a shows the absolute values of E^C_{pol} and E^A_{pol} for the TiN electrode. The cathodic and anodic polarizations have a nearly linear q_0-dependence as expected for a capacitive behavior and are separated by an offset. We observed a similar offset with Pt electrodes under comparable stimulation conditions and attributed it to unequal capacitive polarizations in both phases (Appendix C, Fig. C.5) [257]. For Pt it was also shown that upon gas evolution, the E^C_{pol} and E^A_{pol} values each settle at a plateau. The polarization curves of TiN don't exhibit such plateaus. Further, the series resistance of the TiN electrode (Fig. 4.20b) increases linearly with q_0, which may be related to a gradual surface oxidation and/or H adsorption. In conclusion, the overall polarization behavior of TiN does not provide any specific indications about the onset of gas evolution.

The CNT electrode gives rise to a different polarization behavior. The E^C_{pol} and

E^A_{pol} curves in Fig. 4.20c may be subdivided into 3 regions, I, II, and III. In the first region, the two curves rise linearly and in parallel with a small y-offset; starting at $90\,\mathrm{mC/cm^2}$ they appear to settle (region II), and starting at $210\,\mathrm{mC/cm^2}$ (region III), E^C_{pol} suddenly rises again while E^A_{pol} drops. Simultaneously, R_s in Fig. 4.20d slightly increases in region I and II, and similarly to E^C_{pol} abruptly rises in region III. At this stage, we may only speculate about the underlying mechanism: The polarization in region I reflects the linear charging of the double-layer capacitance; in region II, H_2 evolves, which is not accompanied by a considerable electrode polarization as long as there is no diffusional limitation involved, which is the case for hydrolysis (see also Appendix C, Fig. C.5); in region III, larger gas bubbles form and cannot escape, but block part of the CNT matrix; due to the reduced accessible CNT surface area, the overall double-layer capacitance drops, which in turn leads to an increase in E^C_{pol}; because the gas bubbles also block the resistive path way of the current flow, also R_s rises. The decrease of E^A_{pol} is less conclusive. If the proposed mechanism is true, H_2 evolution occurs at 2 order of magnitude higher charge densities than at Pt under comparable stimulation conditions (Table 4.5). This also means that the q_{csc} for the CNT electrodes (Table 4.2) overestimates the actual q_{cic} by a factor of 5. For Pt, it was by a factor of 2.

From the polarization behavior of the TiN and CNT electrodes we may draw another very important conclusion regarding the use of these materials in experimental paradigms employing simultaneous neural stimulation and recording. One problem of such closed-loop systems is the occurrence of a stimulus artifact, which means that stimulation with an electrode also affects a nearby recording electrode. The consequence is an overload of the high-gain recording amplifier, which generally lasts a few milliseconds. During this time period the recording electrode basically is blind to any spontaneous or evoked neural activity. By using electrode materials that require less polarization to supply the same amount of charge, also the stimulus artifact will decrease. This combined with the lack of a pronounced capacitive decay at the end of the anodic phase (cf. 4.19b) renders the CNT electrodes more favorable for closed-loop systems than TiN electrodes.

Charging and discharging mechanisms at porous electrodes have been studied in the context of supercapacitors and capacitive deionization (CDI) for the purpose of water desalination. Similarities to the case of neural stimulation exist. Basically, CDI relies on the fact that upon application of a voltage difference between two parallel porous electrodes, ions of opposite charge (counterions) become attracted and enter the porous matrix, while coions are expelled. Because the coion outflow is always less than the counterion inflow, the solution between the two electrodes effectively becomes depleted of ions and can be removed by a continuous stream of solution.[258] In the case of neural stimulation, only a single electrode is present, and also no solution stream is imposed. The mechanisms governing the in and outflow of ions should, however, be fairly similar in both applications. While macroscopically, CDI is a rather straightforward concept, there exists only a limited understanding

of the physics involved in the ionic transport in porous structures. The complexity arises on account of the intricate 3D morphology of porous electrodes combined with ion transport and space-charge formation. Most of the research on CDI has been experimental and restricted to conditions where no faradaic charge-transfer takes place. There is hence no relevant or only limited information available on the behavior of porous electrodes under gas evolution. To obtain further insight into this matter, future work must employ well-designed experimental and also numerical approaches to shed light on the processes occurring at CNT electrodes under stimulation.

4.4.5 Summary

We propose coulometric RDC as a new electroanalytical method to characterize electrodes under realistic stimulation conditions. Unlike other techniques described in literature, RDC allows the study of individual electrode processes and their dependence on experimental conditions. Combined with the coulometric approach, it is possibility to reliably detect chemically irreversible redox reactions, in particular gas evolution. Coulometric RDC with symmetric, biphasic current pulses was employed to characterize Pt electrodes in PBS, PBS-BSA, and PBS_{deox}. Additionally, the influence of three pulse parameters was investigated: the pulse width, amplitude, and polarity. The RDC plots revealed clear signatures of the individual electrode processes and were discussed in analogy to the corresponding CVs in Section 4.2.

By means of RDC it was determined that the presence of BSA inhibits Pt oxide formation and reduction, and also O_2 reduction by blocking surface reactive sites. Consequently, also the dissolution of Pt due to the presence of Cl^- ions was suppressed. Electrostatic repulsion by the net negative charge of adsorbed BSA may additionally reduce the accessibility of Cl^- ions to the Pt surface and locally deplete the electrode surface from Cl^- ions. As expected, measurements in PBS_{deox} resulted in a diminished O_2 reduction signal compared to PBS.

Coulometric analysis revealed that irreversible H_2 and O_2 evolution occurred at 10–46% lower applied charge densities in PBS-BSA than in PBS. This behavior was attributed to the inhibitory nature of adsorbed BSA, which limits the capability of Pt to undergo redox reactions and hence restrict its charge-injection capacity. On the other hand, we observed that an increased Pt dissolution rate in PBS under CPW stimulation shifted the onset of gas evolution to higher charge densities. We may generalize that any inhibition of redox activity will promote gas evolution and any enhanced redox reactivity will delay gas evolution. By increasing the pulse width, we also observed that the inhibitory effect of BSA adsorption could be eliminated resulting in the clean Pt behavior. Following the same principle, due to the smaller extent of O_2 reduction, gas evolved at 13–24% lower charge

densities in PBS_{deox} as compared to PBS. It was estimated that the *in vivo* O_2 reduction at the O_2 levels found in the brain would account for 0.4–12% of the total injected charge. The 50 μm diameter Pt electrodes of the neural probe and test chips resulted in comparable charge-injection capacities in PBS.

Finally, we also investigated TiN and CNT electrodes with RDC. The overall capacitive response of these materials rendered them unsuitable for coulometric analysis, which is only a useful approach for electrodes, which inject charge through faradaic reactions. In order to gain further insights in the phenomena that take place at such capacitive electrodes, we also analyzed their overall electrode polarization as a function of the applied charge density. While the TiN electrodes were characterized by a linear and hence capacitive relation between the electrode polarization and applied charge density, the CNT electrode polarization showed more variability. A mechanism was proposed to correlate the observed CNT electrode polarization with the occurrence of gas evolution. Further studies involving theoretical and experimental approaches are necessary to unfold the charge-injection and gas evolution mechanisms at such capacitive electrodes and provide reliable criteria to determine safe stimulation ranges.

Chapter 5

Acute *In Vivo* Performance of Neural Probes and Biocompatibility Aspects

5.1 Extracellular Neural Recording and Stimulation[1]

5.1.1 Introduction

Acute *in vivo* electrophysiological experiments in anaesthetized rats were performed to validate the probes' capability to detect extracellular action potentials and elicit a specific behavioral response upon electrical stimulation. The primary goal was to determine whether successful results can be obtained with the various probe designs and to which extent electrode size and material may pose limitations for the probe functionality.

Besides such probe design and material related aspects, the success rate of *in vivo* experiments is largely determined by the location and orientation of the electrodes relative to the neurons and targeted brain tissue [259]. Adopting the often assumed view of the brain being a homogeneous and isotropic volume conductor and a neuron a point current source [260], the amplitude of an action potentials decays inversely with the electrode-neuron distance. Hence, it is "easier" to record neural activity in brain regions with a higher density of spontaneously active neurons and hence a statistically smaller neuron-electrode proximity. Similarly, the potential

[1] The results presented in this section have been achieved in a joint effort together with Marleen Welkenhuysen [?]

field emanating from a stimulating electrode is often considered point source-like. Accurate placement of the stimulating electrodes is therefore essential for reliably determining stimulation thresholds.

Apart from the electrode configuration and placement in the brain, successful stimulation depends, of course, on the stimulation protocol, i.e. the the pulse length, amplitude, and frequency. Other factors that may influence the outcome of an *in vivo* experiment are related to the preparation of the animal. Stimulation under deep anaesthesia can result in higher thresholds than under light anaesthesia [187].

Additionally, external factors related to the electrophysiological setup including grounding, cable length, signal amplification, and ambient noise can profoundly effect the probe performance in particular the recording quality. Long and unshielded cables between the implanted (passive) probe and the peripheral amplifier and recording unit are prone to electromagnetic interference, and as such most effective in picking up ambient noise. Ground loops are yet another very common source of noise where unwanted electric signal stemming from improperly grounded devices can leak through the recording unit's ground and interfere with the recorded signals. Neural stimulation, on the other hand, is less affected by such set-up related issues. Here, the most crucial requirement is to use a floating bipolar current stimulator unit where the current is strictly flowing between two specified electrodes.

The *in vivo* functionality of the 1G probes was validated in the sensory-motor cortex of rats. Microstimulation of motor cortex neurons in layer V with a high pulsing frequency (330 Hz) has been shown to elicit contractions of contralateral body parts (e.g. hind limb) with current amplitude thresholds of up to 60 μA [187]. For both recording and stimulation with the 2G probes, primarily deeper brain structures were targeted, although initial experiments were also conducted in the motor cortex for comparison with the 1G probes. An advantageous deep brain region for neural recording is the hippocampus, which offers not only a high neuronal density but also a high spontaneous activity [261]. For stimulation with the 2G probe, the ventral tegmental area (VTA) track was targeted including the lateral periaquaductal gray and the deep mesencephalic nucleus. Neurons in these brain areas project to the facial motor neurons that control whisking activity. [262,263] Stimulation in this area is therefore expected to cause whisker movements.

5.1.2 Materials and Methods

In a typical animal experiment [264], rats were placed under general anesthesia (urethane 1.3 g/kg, intraperitoneally (ip)), the head was shaved and desinfected with alcohol (1% in 70% isopropyl alcohol), and local anesthesia (XylocaineR subcutaneously (sc), 2% 20 mg/ml; AstraZeneca SA, Belgium) was applied prior to the scalp incision. The head was fixed in a stereotaxic frame so that bregma and

lambda were in the same horizontal plane. A heating blanket controlled by an anal probe prevented hypothermia during the surgery. The rat's eyes were protected from dehydration by polymyxine B (Terra-Cortril; N.V. Pfizer S.A., Belgium). A longitudinal incision was made and burr holes were drilled after visualization of bregma. The packaged and electrochemically tested probe was screwed to a probe holder, which was then attached to the stereotaxic arm. After puncturing the dura with a needle, the probe was implanted with a microdrive (D. Kopf Instruments, USA) at a speed of 10 μm/s. Prior to implantation of the 2G probe, the Si protection was gently clipped off using a tweezer. The whole setup was suspended on an anti-vibration table placed inside a grounded Faraday cage. All *in vivo* experiments were carried out in accordance with protocols approved by the local University animal ethics committee and in accordance with the European Communities Council Directive of November 24, 1986 (86/609/EEC).

Each recording and stimulation experiment was performed in different animals, i.e. not simultaneously. For recording and stimulation with the 1G probes (50 μm diameter Ni/Au and Pt electrodes, 100 and 200 μm shaft thickness), we targeted the sensori-motor cortex (coordinates: 1 mm posterior to bregma, 2 mm lateral to the midline and up to 2 mm ventral of the dural surface). For neural recording with the long 2G probes (50 and 25 μm diameter Pt electrodes, 100 μm shaft thickness) we targeted the motor cortex-hippocampus-thalamus track (coordinates: 3.6 mm (or 3.3 mm) posterior to bregma, 2.4 mm (or 2.2 mm) lateral to the midline and up to 8 mm ventral of the dural surface) or the motor cortex-extended amygdala track (coordinates: 1 mm posterior to bregma, 2 mm lateral to the midline and up to 8.0 mm ventral of the dural surface [265]. Recording with the short 2G probes (10 μm diameter Pt electrodes, 100 μm shaft thickness) was performed in the cortex-hippocampus track (coordinates: 2.2 mm posterior to bregma, 2.2 mm lateral to the midline and up to 3 mm ventral of the dural surface). Neural stimulation with the 2G probes (triangular and 50 μm diameter Pt electrodes, 100 μm shaft thickness) was performed in the VTA track (coordinates: 6.72 mm posterior to bregma, 2 mm lateral to the midline and 5.5–6 mm ventral to the dural surface; 10° angle to the sagittal plane).

Single and multichannel neural recordings of spontaneous activity with the 1G and 2G probes comprising different electrode sizes and materials were performed either with a commercial system (Leadpoint, Medtronic, USA) with a maximum of 4 channels, 1 m long shielded cables, and an internal preamplifier, or with a custom set-up allowing parallel recording with up to 16 elecrodes [266]. Neural signals were recorded at a sampling rate of 24 kHz (Leadpoint) or 12.5 kHz (custom setup) and band pass-filtered between 0.5–5 kHz (Leadpoint) or 0.3–6 kHz (custom system). Because two recording setups were used with in part unknown specifications (Leadpoint) and different recording modalities (differential with the Leadpoint using two electrodes on the probe and non-differential with the custom system), the recorded signals cannot be compared against each other. Also, due to the

limited amount of 1G and 2G probes tested with each recording system, statistical validation in terms of the recording capability of different probe generations, electrode sizes, and materials cannot be provided. The presented data should therefore be considered a proof-of-concept for the successful recording capability of the probes rather than imply any qualitative or quantitative conclusions.

Neural stimulation with the 1G probe (50 μm diameter Au electrodes, 200 μm shaft thickness) were performed with CF, charge-balanced, and symmetric current pulses with a duration of 200 μs/phase and a pulsing frequency of 333 Hz (DS8000 stimulator in combination with a DLS100 current isolator, WPI, USA). The stimulation polarity was monopolar using a contact on the probe and a metal clamp attached to the animal's skin. Neural stimulation with ($n = 4$) 2G probes (Pt electrodes, 100 μm shaft thickness) was also performed with CF, charge-balanced, and symmetric current pulses with a duration of 100 μs/phase and a pulsing frequency of 50 Hz (DS8000 stimulator in combination with a DLS100 current isolator, WPI, USA). The stimulation polarity was either monopolar (triangular tip electrode or 50 μm diameter electrode vs. metal clamp on the skin) or bipolar (triangular tip electrode or 50 μm diameter electrode vs. large rectangular electrode on the probe). The whisker movements were recorded with a high resolution digital microscopic camera (Digimicro 2.0, DNT GmbH, Germany). Stimulation was performed with cyclic ON and OFF phases. A full stimulation sequence consisted of an initial OFF phase (10 s) to record the baseline whisker movements followed by three sequential ON/OFF phases of 10 s each. Stimulation amplitudes started at 50 μA and, if whisker movement was observed, were decreased in steps of 10 μA until no movement was seen. Higher stimulation currents in steps of 10 μA up to 100 μA, and in steps of 50 μA up to 200 μA were also applied to determine the amplitude-dependency of the movements.

After the experiments, the rats were sacrificed with Nembutal (3 ml, ip; CEVA Sante Animale, Belgium). The explanted probes were immediately cleaned with distilled water to remove blood and tissue residues. A more thorough cleaning involved spraying the probes with a soap-water mixture using a spray bottle and immersing the probes in trypsine (0.05% EDTA, invitrogen, USA) over night.

5.1.3 Results and Discussion

None of the probes broke during implantation and experimentation demonstrating good mechanical stability of both probe generations. Fig. 5.1 shows exemplary data segments of spontaneous activity recorded with the two device generations comprising different electrode sizes and materials. Good signals were obtained with 11 out of 23 tested 1G probes[264], where 'good' refers to a signal-to-noise ratio (SNR)>1.7[267,268]. The 2G probes resulted in a success rate of 7:7, which is much higher than for the 1G probes. One ought to bear in mind, though, that the

Table 5.1: Average stimulation thresholds determined with the second generation probes in 4 *in vivo* experiments.

stimulation polarity	electrode type	current threshold [μA]	charge density threshold [mC/cm^2]
bipolar	triangular	50 ± 14	0.053 ± 0.015
	50 μm Ø	73 ± 21	0.37 ± 0.11
monopolar	triangular	55 ± 21	0.059 ± 0.016
	50 μm Ø	115 ± 41	0.59 ± 0.21

neuronal yield and signal quality in electrophysiological recordings is influenced by many factors including the depth and type of anesthesia, the number of nearby active neurons, and the location of the electrodes (e.g. cortex, hippocampus). Furthermore, the surgical procedure and recording setup was gradually refined in the course of this work, i.e. when passing from the 1G to the 2G probes. With the 1G probes, successful recordings (Leadpoint) were obtained with the Ni/Au and Pt electrodes of 50 μm diameter. No spikes could be detected with smaller electrode sizes using these materials. In contrast, the 2G probes allowed recording of neural activity with the 50 μm (Leadpoint and custom setup), 25 μm (custom setup), and 10 μm diameter (custom setup) Pt electrodes.

Stimulation with the 1G Au electrodes resulted in contralateral hind limb contractions only at 10 times higher current amplitudes than predicted, i.e. at 600 μA. The explanted electrodes were consistently damaged after such a harsh treatment and the tissue presumably as well. Stimulation with the 2G Pt probes using the stimulation parameters described above elicited an amplitude-dependent movement of the whiskers. The values for the current and charge density thresholds for bipolar and monopolar stimulation are summarized in Table 5.1. The current threshold is theoretically solely determined by the excitability of the tissue [94] and should not depend of the electrode size, which was confirmed by the results (within standard deviation).

On the other hand, the charge density threshold and hence risk for electrode and neural damage [269] should increase with decreasing electrode area. The charge density thresholds of the triangular electrode are approximately one order of magnitude lower than the values determined for chemically irreversible gas evolution under CF-CPW stimulation *in vitro* (Table 4.5). In contrast, the thresholds for the 50 μm diameter Pt electrode are of the same order of magnitude as the values in Table 4.5. Although the mechanisms underlying stimulation-induced neural injury are not well understood, we can say that stimulation with the triangular electrode is less likely to induce damage than stimulation with the 50 μm diameter electrode. Future experiments involving chronic stimulation and histochemical analysis will shed more light on this matter.

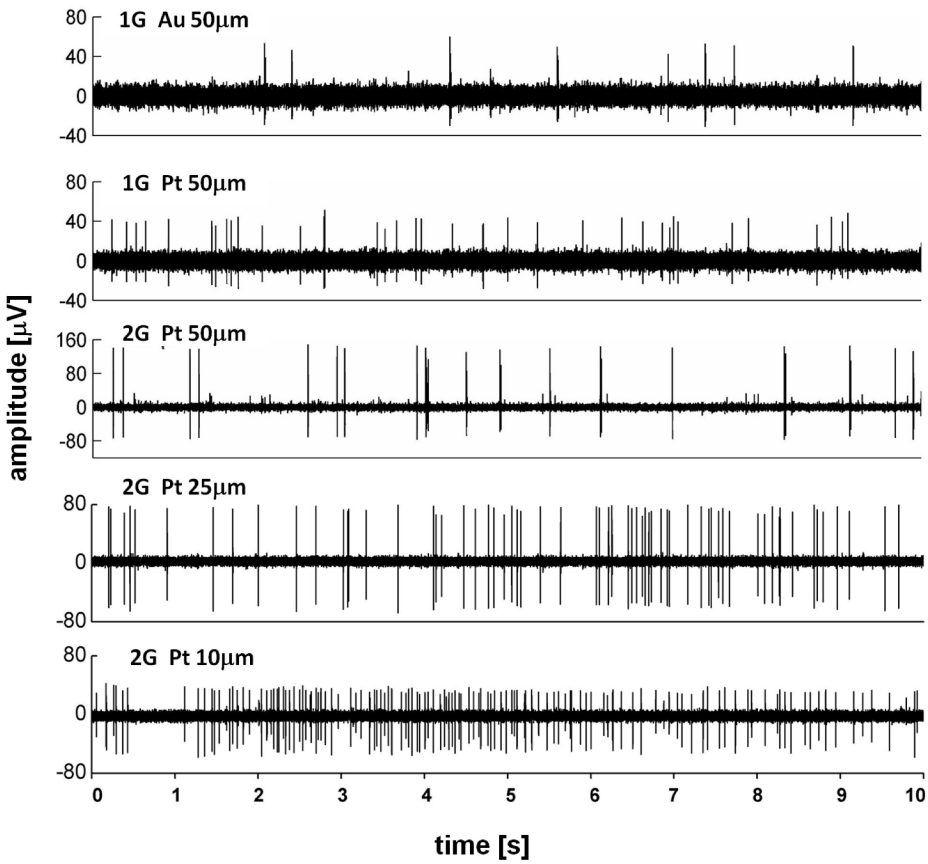

Fig. 5.1: Examples of spontaneous neural activity recorded with 1G probes containing 50 μm diameter Au and Pt electrodes in the motor cortex, and in the hippocampus with 2G probes containing Pt electrodes of 50, 25, and 10 μm diameter. All data are from different animals and probes and are shown as recorded.

5.2 *In vivo* Electrochemical Characterization

5.2.1 Introduction

We have shown in Chapter 4 that an electrode's ability to record neural signals and introduce electric charge into the host environment is sensitive to the physico-chemical constitution of the electrode-electrolyte interface. By also investigating the influence of albumin adsorption on the electrode behavior, our understanding of the electrode-electrolyte interface has been refined. Even though, the presented *in vitro* model regards only a fraction of the factors that may affect the electrode behavior *in vivo*. The complex compositional and structural tissue properties can not nearly be reproduced *in vitro*. Various proteins with different distributions and steric orientations of charged groups can adsorb onto an electrode surface to form a proteinaceous layer which may behave differently than its individual constituent [270,271].

In addition, numerous other electroactive substances encountered in brain tissues, including the neurotransmitter dopamine, ascorbic acid, NO, O_2, and H_2O_2, readily react at electrode surfaces [237]. In this work, a particular interest was to shed light on those electrode processes that may interfere with the (acute) recording and stimulation capabilities of an electrode. Electrochemical methods are most suitable to explore such effects *in vivo*, because they provide *in situ* information on the processes taking place at an electrode without being destructive, i.e. without the need to extract tissue from the brain to perform the experiments.

Traditionally, *in vivo* electrochemical methods in neuroscience including fast-scan cyclic voltammetry and amperometry are used to investigate the neurochemistry of the brain by monitoring dynamic events, such as the change in extracellular dopamine concentration during electrical stimulation. [237] In recent years, electrochemical techniques have increasingly been employed to also characterize neural electrodes *in vivo* [174,272–274,189,18,173]. Most of these reports employ EIS to study the electrode impedance of recording electrodes. One report also describes the use of CV to study CNT electrodes *in vivo* [173]. To our knowledge, no *in vivo* CV data is available for Pt microelectrodes.

In order to validate the *in vitro* results described in the previous chapter, *in vivo* electrochemical experiments, including CV, EIS, and RDC were performed using 2G probes with 50 μm diameter Pt electrodes. Unlike *in vitro*, the accessible experimental volume *in vivo* is very restricted and requires setup modifications to allow the accommodation of a 3-electrode electrochemical cell. Providing a reliable RE in close proximity to the probe is essential for reliable and sensitive measurements. If the RE is to far from the probe, a considerable tissue resistance will introduce noise into the measurements and corrupt the recorded electrode potentials. *In vivo* neurochemical experiments often rely on Ag|AgCl wires directly

implanted in the animal's brain or immersed in a reference solution in contact with the brain surface[237]. Electrochemical experiments for the characterization of neural probes have employed either stainless steel screws fixed to the skull[174,274], or Ag|AgCl wires or pellets positioned on the brain surface in a reference solution. Neither of these REs was considered acceptable for our purpose, which requires that the RE be close to the probe and surrounded by a reference solution. A custom RE was therefore devised small enough to be co-implanted with the probe.

5.2.2 Materials and Methods

In order to realize an implantable version of the 3-electrode electrochemical cell, miniaturized Ag|AgCl reference electrodes were manufactured to allow co-implantation with the probes. For this purpose, quartz glass capillaries (Sutter Instruments, USA) with an outer diameter of 1 mm and an inner diameter of 0.5 mm were pulled with a micropipette laser-puller (Model P-2000, Sutter Instrument, USA) to a tip length of approximately 6 mm and an orifice opening of 3 μm. For the reference electrolyte, a 1.5% w/w agar gel was prepared in 3 M KCl: 0.6 g agar were soaked in 20 g 3 M KCl under magnetic stirring at 50°C for 1h and then heated up to 200°C under further addition of 20 g KCl. After the mixture clarified, it was quickly injected into the glass pipettes through the large opening with the help of a syringe. Thin silver wires were chloridized in 3 M KCl (Auto Chloridizer, HSE, Germany) generating a thin AgCl coating. The wires were carefully inserted into the agar-filled micropipettes. The pipette openings with the Ag|AgCl wires partly sticking out were sealed with small sheets of parafilm to prevent dehydration of the agar. A ready-prepared miniature reference electrode (μRE) is shown in Fig. 5.2a. The reference electrodes were stored in 3 M KCl till implantation. All chemicals were analytical grade and used as delivered (Sigma-Aldrich, USA). For each implantation, three μREs were fixed on the probe holder using sticky tape and were screwed together with a 2G probe (Fig. 5.2b, c). The probe-pipette distance was approximately 1.5 mm and the pipette-pipette distance was 1 mm. All *in vivo* measurements were performed in the motor cortex (coordinates: 1 mm posterior to bregma, 2 mm lateral to the midline and up to 2 mm ventral of the dural surface) following the standard surgery protocol described above. During experiments, the brain surface was regularly moisturized with fresh PBS. Measurement results refer to data obtained from three animals.

The *in vivo* electrochemistry of 50 μm diameter Pt electrodes was investigated by CV, EIS, and RDC according to the protocols defined in Section 4.4.2. Briefly, 0.5 h after implanting the probes, 10 CV cycles were measured at a scan rate of 0.1 V/s between the limits of gas evolution determined in PBS, followed by EIS using a 10 mV (rms) ac signal applied between $1 - 10^5$ Hz. For RDC, 50 biphasic CF current pulses were applied in CPW mode. Measurements were made using an Autolab PSTAT302N potentiostat with integrated frequency response analyzer

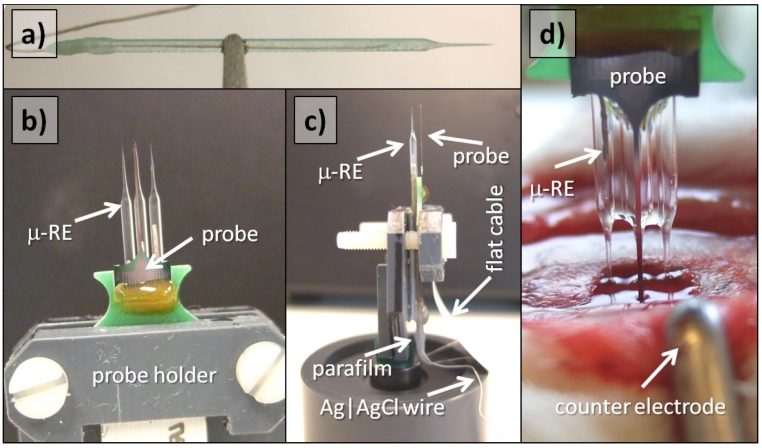

Fig. 5.2: (a) Miniature reference electrode (μ-RE). (b) Front and (c) side view of an assembly consisting of a 2G probe with 3 μ-REs fixed to a probe holder. (d) Implanted probe-μRE assembly.

controlled by the NOVA software (Ecochemie, NL). For RDC, an additional ADC module (ADC10M, Ecochemie, NL) was used for high-speed sampling at 250 kHz. The EIS data was analyzed by NLSF (ZView, Scribner, USA) to the equivalent circuit model in Fig. 4.7.

5.2.3 Results and Discussion

Fig. 5.3 compares the CVs obtained with 50 μm diameter Pt electrodes in PBS and PBS-BSA using a test chip (cf. Section 4.2.3), and *in vivo* with a probe. Stability tests confirmed that the performance of the custom μREs was comparable to that of the commercial Ag|AgCl REs. The H adsorption and desorption features between -0.6 V and -0.3 V (Eq. 4.2), the current step between -0.2 V and 0.2 V due to the reduction of dissolved O_2 (Eq. 4.1), and the Pt oxide reduction peak around 0 V are barely discernible *in vivo*, most likely on account of an adsorbed proteinaceous layer, which blocks the Pt surface reactions. In addition, the anodic oxidation signal from 0.5 V onwards is much larger *in vivo* than in PBS-BSA, which may be due to the adsorption and oxidation of larger amounts of proteins (Eq. 4.14) [275,199] and/or due to other electroactive species. Dopamine and serotonin are known to undergo oxidation between 0.5 and 0.7 V vs. Ag|AgCl [237]. Clearly, the *in vivo* electrochemical fingerprint of the electrode-tissue interface cannot entirely be described with the simplified PBS-BSA model. For a more accurate analysis of the underlying electrode processes *in vivo*, CVs should be measured during and

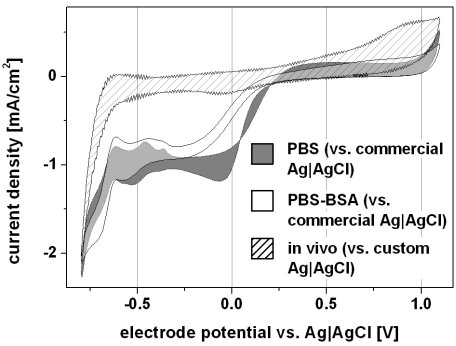

Fig. 5.3: Comparison of CVs measured with 50 μm diameter Pt electrodes *in vivo* (2G probe; motor cortex), and in PBS and PBS-BSA (test chip; cf. Fig. 4.5) at 0.1 V/s.

after the probe implantation for prolonged periods of time to capture the dynamic changes at the interface.

In Fig. 5.4 we compare the average Bode plots obtained in PBS using the test chip and *in vivo* with $n_e = 5$ different Pt electrodes in 3 different animals. The impedance magnitudes diverge for higher frequency most likely due to a larger series resistance *in vivo*. In addition, the *in vivo* phase angle is shifted to more positive values compared to the phase angle in PBS. More clarity about the underlying mechanisms is obtained from the NLSF values in Table 5.2. As expected, the R_s *in vivo* is about one order of magnitude larger than in PBS and PBS-BSA (cf. Table 4.4) and may be attributed to the higher resistivity of brain tissue (400 Ω cm for gray matter [276] compared to 70 Ω cm for PBS). A pronounced shift of α towards smaller values can be noticed, which is responsible for the observed phase angle shift.

Unlike the measurements in PBS-BSA, no adsorption pseudocapacitance, C_ϕ, and accompanying resistance, R_ϕ, were required to fit the *in vivo* spectra, although the CV measurement in Fig. 5.3 clearly indicates the presence of an adsorbed protein layer. Similarly, the *in vivo* R_{ct} and C_i values were of the same order of magnitude as in PBS (cf. Table 4.4). The reasons for this similarity are only speculative, but may be related to the fact the exposure time of the implanted probes to tissue was less (<1 h) than the exposure time of test chip to the PBS-BSA solution (>3 h) prior to performing EIS. Hence the influence of adsorbed proteins is less pronounced than in PBS-BSA. This, however, contradicts the observations with CV, which suggest a strong protein adsorption *in vivo*. The *in vivo* electrode impedance at 1 kHz was 50% higher than in PBS-BSA. For acute experiments, such an increase in electrode impedance may not considerably affect the recording efficacy.

Fig. 5.5 shows an exemplary RDC data set obtained with CF-CPW stimulation *in vivo* in comparison to the corresponding RDC response obtained with a test chip in PBS (cf. Appendix C, Fig. C.1). Similar to the *in vivo* CV in Fig. 5.3, faradaic features related to H adsorption and desorption as well as Pt oxide reduction were strongly suppressed, which may be related to the presence of an adsorbed protein layer. The rather featureless and capacitive *in vivo* response

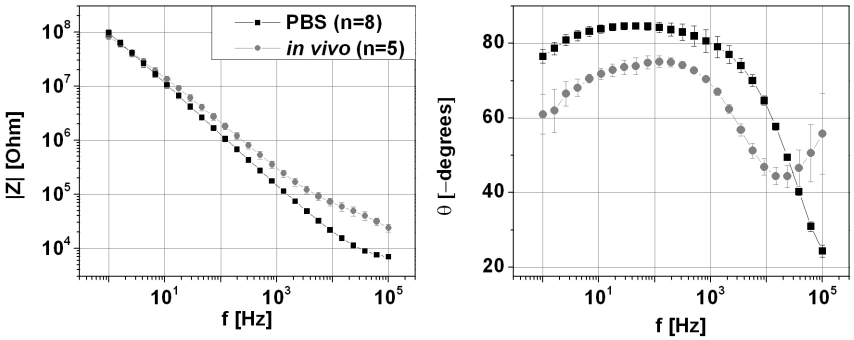

Fig. 5.4: Average Bode plots for Pt electrodes of 50 μm diameter measured between 1 – 10^5 Hz in PBS (test chip) and *in vivo* (2G probe; motor cortex).

Table 5.2: Average fitting parameters of the impedance spectra recorded *in vivo* (acute) using 2G probes with 50 μm diameter electrodes.

circuit element	medium	
	PBS	brain
R_s [kΩ]	7.53 ± 0.24	49.26 ± 12.40
R_{ct} [kΩ]	(7.97 ± 2.78) E5	(3.35 ± 1.57) E5
T_{CPE} [nF s$^{\alpha-1}$]	1.85 ± 0.47	2.20 ± 0.33
α	0.93 ± 0.02	0.83 ± 0.02
C_ϕ [nF]	–	–
R_ϕ [MΩ]	–	–
C_i [pF]	54.79 ± 8.40	52.13 ± 17.34
$\|Z\|$(1 kHz) [kΩ]	175.91 ± 12.24	355.65 ± 55.17
n_e	8	5

is not suitable for coulometric analysis. Within the range of investigated q_0, no typical signal increase indicating gas evolution occurred. Clearly, the overall *in vivo* behavior of the Pt electrodes differs strongly from the results obtained *in vitro*. The typical electrochemical signatures are almost entirely obscured and don't allow any qualitative or quantitative analysis of the electrode processes and hence of safe stimulation ranges. Further experiments also employing CPA stimulation will have to answer the question whether coulometric RDC can provide any specific indication of the onset of chemically irreversible reactions during *in vivo* stimulation. In addition, future *in vitro* studies should also investigate the combined effects of other proteins and possibly also neuronal cell cultures.

5.3 Biocompatibility Aspects

5.3.1 Introduction

As already mentioned in Section 2.4.1, a material is never per se biocompatible or not. Depending on the intended field of application (*in vitro* or *in vivo*, brain, eye, cochlear, heart, etc.) and exposure time to the biological tissue (hours to decades), one may have to reassess the biocompatibility of a particular material. Considering that the neural probes developed in this work were primarily intended for acute experiments (3-5 h) in order to validate the probes' functionality and establish a reliable physiological setup, long-term biocompatibility was rather of secondary importance. Nonetheless, a long-term study of 5 weeks involving 10 1G probes with Pt electrodes demonstrated that 2 probes remained functional, i.e. were able to record signals after 4 weeks post-implantation. Immunohistochemical analysis indicated an extensive tissue reaction to probe implantation at 1 week post-implantation. [264]

In several short-term *in vitro* experiments involving the test chips with Pt and TiN electrodes, successful electrophysiological measurements could be performed with cardiomyocytes up to 4 days *in vitro* [266,277]. Based on this limited amount of experimental validation, it would be premature to classify the employed materials or the fabrication process as biocompatible. On the other hand, there were no

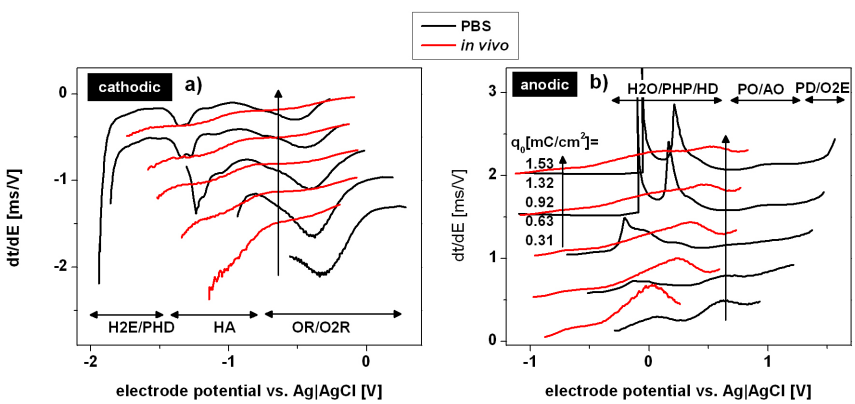

Fig. 5.5: Series of $dt/dE(E)$ plots obtained in response to CF-CPW stimulation with 50 μm diameter Pt electrodes *in vivo* (2G probe; motor cortex) and in PBS (test chip). (a) Cathodic phase, (b) anodic phase. Only a selection of all applied (absolute) charge densities, q_0, is shown. Graphs are stacked by a constant offset. Regions of Pt-specific reactivity (as identified in PBS) are indicated by horizontal arrows. Long vertical arrows point in the direction of increasing q_0.

indications of short-term cytotoxicity.

Although it has been demonstrated that pristine and chemically functionalized CNTs are biocompatible toward neurons [119,278], their relative novelty to the field of neural engineering still leaves many questions unanswered. In particular, integrating CNTs on microfabricated structures may contaminate the CNTs with toxic organic compounds or metal traces introduced by the fabrication and handling process. Such concerns are much more persistent for CNTs than for Pt and TiN, because the 3D porous and hydrophobic morphology of CNTs may easily and irreversibly entrap organic species [279,280] and be decorated by metallic nanoparticles [281]. In addition to such contamination issues, chemical modifications by acid and/or oxygen plasma treatment may also affect the biocompatibility of the CNTs [282]. Consequently, for any new fabrication approach, the biocompatibility of the CNTs needs to be reassessed. Here, we have performed preliminary *in vitro* biocompatibility tests of fabricated CNT substrates using primary rat hippocampal neurons.

5.3.2 Materials and Methods

For biocompatibility testing, test chips were prepared according to the process sequence displayed in Fig. 3.7; however, the two lift-off steps were omitted and an unpatterned metal stack of Ti/Pt/Ti/TiN (20 nm/200 nm/20 nm/100 nm) was used instead. The CNTs were grown according to the procedure described in Section 3.3.3. Cell viability was tested with primary hippocampal neurons isolated from embryonic rats. The CNT substrates were sterilized in 70% ethanol and incubated with poly L-lysine (Sigma-Aldrich, USA) prior to cell plating. After 5 days *in vitro*, samples were removed from the incubator, fixated with formaldehyde, and treated with a 2% OsO_4 solution (Sigma-Aldrich, USA) for increased contrast during SEM analysis (SU8000, Hitachi, Japan). Finally, the samples were rinsed with PBS, dehydrated in solutions of increasing ethanol concentration, and subjected to critical point drying (Tousimis, USA).

5.3.3 Results and Discussion

Fig. 5.6 shows SEM images of neurons grown on fabricated CNT substrates after 5 days *in vitro*. The neurons readily formed equally branched neural networks on top of the Parylene C and exposed CNT areas as shown in Fig.5.6a and b. Visible neurite ruptures are an artifact caused by sample preparation. The neuronal cell bodies did not make conformal contact with the underlying CNT microbundles, but rather seemed suspended on the surface (Fig. 5.6c and d). Recent reports investigating the *in vitro* interaction between vertically-aligned carbon nanofibers and myocytes [156] and PC-12 cells [283] concluded that the nanofibres were able to penetrate the cell membrane. We don't believe that similar behavior is possible with the CNTs due

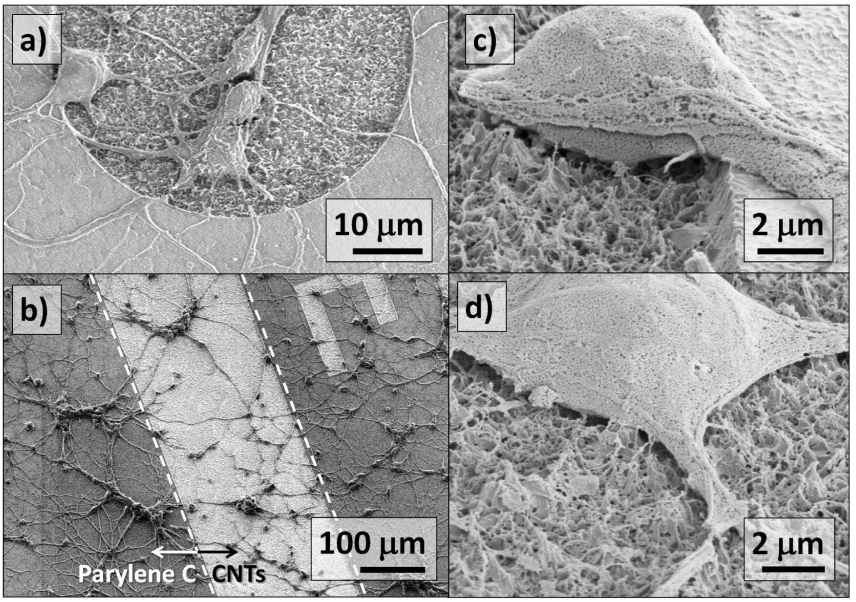

Fig. 5.6: Scanning electron micrographs of primary rat hippocampal neurons after 5 days *in vitro* on fabricated CNT substrates.

to their tendency to form microbundles, which are too larger to penetrate the cell membrane. Furthermore, due to the presence of a necrotic and fibrous tissue layer between a prospective CNT-based implant and healthy tissue, neurons *in vivo* are not expected to be in a sufficiently close proximity to the electrode surface to attach. The observed *in vitro* neuron-CNT interaction is hence only of secondary relevance for implanted devices. Nonetheless, the results clearly demonstrate that encased CNT electrode can be fabricated using the proposed process flow without introducing any acute toxic compounds. Additional biocompatibility experiments will be necessary to statistically support these promising results.

5.4 Summary

Successful recordings of spontaneous action potentials in cortical and deep brain regions could be demonstrated with the 1G and 2G probes comprising different electrode materials (Au and Pt) and sizes (10, 25, and 50 μm). Considering that the 10 μm diameter Pt electrodes have an impedance of 2.4 $\pm$ 0.1 MOhm at 1 kHz (cf. Fig. 4.9), recording with even smaller electrodes is only a realistic scenario for future implants, if the electrode impedance is significantly reduced. To our knowledge, *in vivo* recording with neural probes has so far only been demonstrated

down to electrode sizes of 7 μm diameter using Ir electrodes with an impedance of 2.5 MOhm a 1 kHz [149].

Reliable bipolar and monopolar neural stimulation was only achieved with the 2G probes. Here, the stimulation threshold determined with the large triangular Pt tip electrode lied well below the charge densities determined for irreversible gas evolution *in vitro*. In contrast, stimulation with the 50 μm diameter Pt electrodes required charge densities at the limit of safe stimulation. In order to also enable safe stimulation with smaller electrodes and hence higher selectivity, future neural implants must employ more efficient electrode materials.

We performed acute *in vivo* CV, EIS, and RDC analysis of the 2G probes with 50 μm diameter Pt electrodes using a custom-made implantable Ag|AgCl RE in order to validate and complement the *in vitro* results obtained in PBS and PBS-BSA in the previous chapter. The overall electrochemical signature of Pt was strongly suppressed *in vivo* as determined by CV and RDC. Such inhibition could be caused by an adsorbed proteinaceous film. While the strong anodic oxidation signal recorded with CV supports this conclusion, the EIS data does not confirm the presence of a strongly adsorbed protein layer. Due to the capacitive RDC response we could not perform coulometric analysis to identify the onset of irreversible gas evolution during stimulation. Furthermore, the *in vivo* electrode impedance increased only by 50% compared to the impedance measured in PBS-BSA, which is unlikely to affect the acute *in vivo* recording efficacy.

Overall, the *in vivo* electrochemical data provide rather unspecific information about the processes that take place at the electrode-tissue interface. Further insights into these processes may be obtained from electrochemical measurements performed during the probe insertion and during chronic implantation. Such data may provide a more refined picture of the electrode-tissue dynamics and especially allow the identification of the nature of the strongly capacitive electrode response. Additional correlation of the observed electrochemical response with the neural signal quality and stimulation thresholds may also help identify the qualitative changes occurring at the interface. Useful information may also be obtained from systematic *in vitro* experiments involving other proteins and also neural cell cultures.

Finally, from initial *in vitro* viability experiments using primary rat hippocampal neurons we can conclude that the microfabricated CNT electrodes are not afflicted by adverse or toxic substances introduced during the fabrication. The proposed fabrication process can hence be employed to realize future CNT-based neural implants. Based on the range of successful *in vitro* and *in vivo* physiological experiments, we may say that the employed electrode materials and device structures are sufficiently biocompatible to allow short-term *in vivo* experiments of a few days.

Final Remarks & Outlook

Neural probes offer unique scientific and clinical opportunities for investigation, diagnosis, and therapy of neural conditions. Dysfunctional activity can often be identified non-invasively using neuroimaging techniques, including fMRI combined with EEG. Once localized, affected brain structures can be studied in further detail by introducing probes to analyze the neurochemistry, record the electrical activity, and stimulate either acutely or chronically.

In this thesis, two probe generations have been developed, and successful proof-of-concept recording and stimulation in cortical and deep brain areas of rats have been demonstrated. As such, the probes can be engaged in a variety of experimental paradigms ranging from long-term multi-channel recording, electrode impedance monitoring to chronic behavioral studies involving stimulation. The current probes offer the possibility to record with up to 11 10–50 μm diameter Pt electrodes and safely stimulate with one relatively large contact in monopolar and bipolar mode.

For an actual and meaningful communication with the brain, recording and stimulation must be performed simultaneously. Providing a direct stimulation feedback to neural recording and vice versa may help normalize dysfunctional activity patterns in an efficient way [284] and serve as a means to study activity-dependent neuroplasticity [11] and functional links between different brain regions. Such closed-loop strategies and hence timed stimulation may in particular benefit clinical DBS by improving its specificity and therefore help reduce possible side effects due to redundant stimulation. Also, the more economical charge utilization in closed-loop systems may translate into greater safety and longer battery life. The major challenges for *in vivo* closed-loop systems are the development of real-time and specific detection algorithms, safe stimulation, minimal interference between recording and stimulation channels, and a stable and chronic electrode-tissue interface.

In terms of the latter, the performance of the probes developed in this work has mostly been tested in acute experiments. While acute experiments are essential to validate new implantable systems, they do not represent clinically relevant chronic settings. Unfortunately, the stability of chronic recordings with neural probes

generally shows a large variability and spans periods of only a few weeks up to several months [285]. This gradual signal loss and degradation of the electrode-tissue coupling can have several reasons, include micromotions of the probe and the formation of an insulating glial scar around the implant in response to tissue inflammation [286,285]. Various strategies have been proposed to reduce the extent of inflammation and hence scar tissue formation, including drug-eluting hydrogel coatings to promote neural growth toward the electrodes [285,287,25] and also new biohybrid approaches with neural stem cell-seeded probes [288**?**]. It remains unclear, however, whether these biological approaches actually can offer a lasting remedy.

Clearly, significant improvements of the long-term electrode-tissue coupling and signal quality can only be achieved on the basis of a profound understanding of the physiological, biochemical, and electrical changes that take place during chronic device operation. Histological and immunohistochemical analyses of dissected brain tissue are surely indispensable in order to study the extent and nature of inflammation, but their biggest shortcoming is their destructivity. More ambitious strategies for the *in situ* characterization of the electrode-tissue interface are needed. The simultaneous *in vivo* monitoring and correlation of the electrode and tissue impedance, signal quality, and biochemical composition would surely provide a more complete picture.

In this thesis, we have only scratched the surface of what may be possible by using *in situ* electrochemical techniques. Acute *in vivo* experiments in anaesthetized rats involving EIS, CV, and RDC of 2G probes with 50 μm diameter Pt electrodes were performed to gain insight into the processes that take place at implanted electrodes. The observed electrochemical fingerprint was rather unspecific and did not allow a clear identification of individual electrode process. A more refined picture of the electrode-tissue interface and the nature of the underlying electrode processes may be obtained from chronic electrochemical analysis possibly also involving the simultaneous quantification of neural signal quality and stimulation thresholds. Additional information about the electrode performance can also be obtained from more realistic *in vitro* experiments taking into account the compositional and possibly also structural complexity of brain tissue. This thesis has analyzed the influence of two relevant factors on the *in vitro* electrode performance: albumin adsorption and the concentration of dissolved O_2. Future experiments may involve other proteins and also *in vitro* neural cultures. Besides electrochemical techniques, microdialysis is another *in situ* approach that may help provide a more comprehensive biochemical profiling of the electrode-tissue properties after the implantation of a neural probe.

Strategies to provide a more reliable electrode-tissue coupling must also seek to improve the electrode side of the interface. Electrode materials with a lower impedance may increase the recording sensitivity and possibly allow the detection of signals even in the presence of the insulating glial scar surrounding the implant. Here, we've shown that CNTs are the most promising of all electrode materials

with electrode impedances below 10 kOhm even for the 5 μm diameter electrodes. However, the use of CNTs in neural implants also raises concerns about their pathogenic potential and exposure limits. There still exists a lack of information regarding the acute and long-term effects that CNTs may have on the brain. Such issues must be addressed concomitantly to the improvement of their physico-chemical properties.

Unlike recording, there is basically no information available on the long-term stimulation efficacy of neural probes, let alone the simultaneous recording and stimulation *in vivo*. Safe stimulation, in particular with electrodes of cellular dimensions, still is the more difficult task to achieve with neural probes compared to recording. Due to this shortcoming, there exists a fundamental gap in terms of the understanding of the mechanisms underlying both functionalities. Significant progress in stimulation (with neural probes) has been delayed mostly due to the lack of suitable electrode materials that can cope with the relatively high currents required to activate neural tissue. We have sought to mitigate this shortcoming by employing a relatively large tip electrode for stimulation. In addition, we have shown that CNTs are the most promising electrode material for safe stimulation at cellular and sub-cellular scales. Furthermore, stimulation with CNT electrodes is accompanied by a much smaller electrode polarization compared to Pt and TiN electrodes. Consequently, stimulus artifacts interfering with simultaneous recording and stimulation may equally be reduced, which is beneficial for closed-loop applications.

Considerable research must now follow to uncover the mechanisms of neural activation. With electrical stimuli, the clinical effects at the level of the whole organisms have a long history of empirical documentation, but their interpretation at the cellular and molecular level is still lagging behind. Future research must also adopt pharmacological methods to assess the effects of electrical stimulation. In addition, new experimental approaches are required to identify the factors that may lead to tissue and electrode degradation during stimulation. An important step towards a better understanding of the potentially harmful electrode processes occurring under stimulation has been provided in this thesis. A new coulometric technique has been presented that allows a clear and specific detection of the onset of gas evolution. We have also shown that its usability is limited to electrode materials employing faradaic charge-transfer processes. Therefore, there still exists the need to provide practical techniques to characterize electrodes relying on capacitive charging mechanisms. A profound understanding of the processes occurring at electrodes under stimulation is a prerequisite to provide better electrode designs and stimulation strategies.

Efforts are currently undertaken by many research groups to equip neural probes with a multitude of functionalities, including optical stimulation, large-scale recording involving 100s of electrode sites, closed-loop modalities, and many more. Such technological advances offer exciting new possibilities to study the brain

at an unprecedented spatiotemporal resolution and have already demonstrated remarkable achievements. However, in order to really and profoundly contribute to the field of neuroscience, such new technologies must escape the stage of proof-of-concept and become available to a broad range of research facilities. Only through widespread and multifocal research initiatives it will be possible to fully answer questions related to the efficiency, reliability, and safety of these probes.

Appendix A

Contact Angle and Fourier Transform Infrared Analysis of CNTs

Introduction

It is known that chemical modifications by acid treatment and/or exposure to oxygen plasma can profoundly change the properties of CNTs, including hydrophobicity and biocompatibility [289,282]. Avoiding chemical changes of the CNTs during device fabrication (cf. Section 3.3.3) was an important aspect of process reliability in this work. Such a restriction ensures that post-processing treatments can be tailored to specifically modify the CNTs. In order to investigate the impact of the different processing steps on the chemical properties of the CNTs, we performed contact angle measurements and FTIR analysis.

Materials and Methods

Contact angle measurements and FTIR analysis were preformed on as-grown CNTs, BHF-treated CNTs, and SiO_2-coated and BHF-treated CNTs. The CNTs were uniformly grown on a wafer with TiN/Ni (100 nm/2 nm) following the procedure described in Section 3.3.3. Test samples with as-grown CNTs and CNTs coated with 300 nm CVD SiO_2 were immersed in BHF for 1.5 min. All FTIR spectra were collected in transmittance (%) mode (IFS 66 v/S, Bruker Optics, Germany)

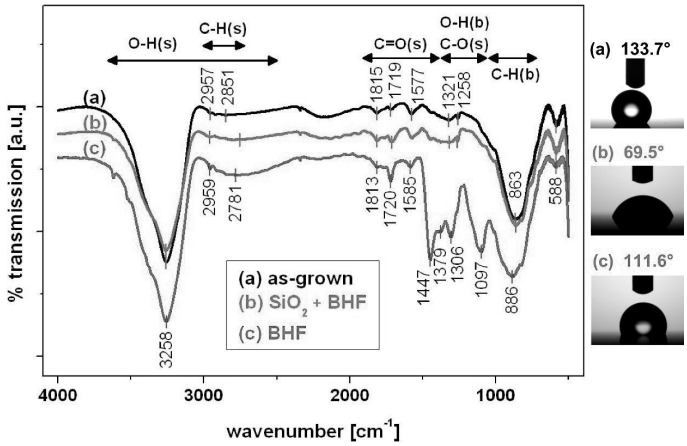

Fig. A.1: Basline-corrected transmittance infrared spectra of (a) as-grown CNTs, (b) SiO_2-coated CNTs after BHF treatment, and (c) CNTs after BHF treatment. The corresponding contact angles for the three substrates are shown on the right-hand side.

over the wavenumber range of $500 - 4000\,\mathrm{cm}^{-1}$. Recorded spectra were corrected for baseline and analyzed using OriginPro 8.5 (Originlab, USA). Contact angle measurement were preformed with an OCA20 contact angle systems (dataphysics, Germany) using $1\,\mu\mathrm{l}$ droplets of distilled water.

Results and Discussion

Fig. A.1 shows the baseline-corrected FTIR spectra and contact angles determined from as-grown CNTs, BHF-treated CNTs, and BHF-treated SiO_2-coated CNTs similar to the fabrication sequence of the actual CNT electrodes. All spectra contain a broad band with a maximum near $3258\,\mathrm{cm}^{-1}$ originating from stretching modes due to various O-H containing surface groups [290,291] possibly related to humidity on the sample surface. A weak band centered around $2700\,\mathrm{cm}^{-1}$ may be caused by O-H and C-H stretching modes [292]. The signals at $1813\,\mathrm{cm}^{-1}$, $1720\,\mathrm{cm}^{-1}$, and $1585\,\mathrm{cm}^{-1}$ are assigned to C=O stretching modes [293,294,292]. In addition, for the BHF-treated as-grown CNTs, a strong peak appeared at $1447\,\mathrm{cm}^{-1}$, which also describes C=O stretching vibrations [293,294]. Signals in the region 1400-1000 cm^{-1} are assigned to O-H bending and/or C-O stretching modes [293,292]. A strong peak in this region at $1097\,\mathrm{cm}^{-1}$ was observed for the BHF-treated CNTs. The band at approximately $850\,\mathrm{cm}^{-1}$ is attributed to C-H bending modes [292]. Clearly, the BHF treatment introduces additional O-containing functional groups. In contrast, the spectrum of the BHF-treated SiO_2-coated CNTs does not reveal any significant

changes compared to the as-grown CNTs, which indicates that the BHF exposure time is sufficient to remove the oxide and leave the CNTs unaltered. The results also indicate that functional groups are to some extent present in the as-grown CNTs.

The contact angle is lowest for the BHF-treated SiO_2-coated CNTs. The BHF treatment of the as-grown CNTs only marginally improved their wettability, which is unexpected considering the largest IR signal increase due to hydrophilic functional groups. Therefore, the improved wettability of the BHF-treated SiO_2-coated CNTs is rather physical than chemical in nature. It was indeed shown that a better hydrophilicity can be achieved with CNT films that have an open microtexture as opposed to closed unmodified CNT films [295]. The appearance of microbundles on the BHF-treated SiO_2-coated CNTs may hence account for the reduced contact angle. On the other hand, no microbundles were observed after BHF treatment of the as-grown CNTs. This demonstrates that the presence of the SiO_2 is essential for mediating the BHF into the CNT matrix and eventually forming the microbundles which improve the wettability.

Summary

FTIR spectra of CNTs immersed in BHF for 1.5 min revealed a strong signal increase for O-containing functional groups as compared to as-grown CNTs. Prolonged exposure of CNTs to BHF therefore chemically modifies the CNTs. In contrast, no such modifications were observed with CNTs coated with CVD SiO_2 and subsequently immersed in BHF for 1.5 min to remove the SiO_2. We may therefore conclude, that the fabrication process proposed in Section 3.3.3 does not chemically alter the CNTs. This aspect is essential for providing sufficient flexibility with post-processing treatments to specifically tune the CNT properties. In addition, the best CNT wettability as determined by contact angle measurements was achieved with the SiO_2-coated and BHF-treated CNTs. Only a marginal improvement was observed for the BHF-treated CNTs despite their largest signal increase on account of hydrophilic functional groups. The as-grown CNTs were the least hydrophilic. The difference in wettability was attributed to the presence of microbundles, which only appeared on the SiO_2-coated and BHF-treated CNTs.

Appendix B

Potentiodynamic Electrochemical Impedance Spectroscopy of IrO_x

Introduction

One of the more salient electronic features of IrO_x is its ability to switch between a semiconducting and metallic state upon injection and ejection of protons and electrons. In order to gain further insight into this behavior, we performed potentiodynamic EIS (PDEIS), i.e. potential-resolved EIS. The interfacial properties of a metal-electrolyte interface have been introduced in Chapter 2. Here we will briefly discuss the properties of the semiconductor-electrolyte interfaces. Many oxide films that form spontaneously on metal surfaces are semiconducting, including TiO_2, SnO_2, and ZnO.

When a semiconducting electrode is immersed into an electrolyte, a potential difference is established at the interface. If the conductivity of the (doped) semiconductor is considerably lower than that of the electrolyte, practically all of the potential drop occurs over the space-charge region that forms at the electrode. The situation is opposite to that of the metal-electrolyte interface and very similar to that at a semiconductor-metal contact. The charge distribution in the semiconductor is analogous to that in the diffuse double layer on the solution side of a metal-electrolyte interface and is accordingly derived using the Poisson-Boltzmann equation. Considering an n-type semiconductor, the capacitance of the

space-charge region, C^0_{sc}, can be written as:

$$C^0_{sc} = \epsilon_r \epsilon_0 \kappa \cosh\left[\frac{e(E - E_{fb})}{k_B T}\right] \tag{B.1}$$

where ϵ_r is the dielectric constant of the semiconductor, E_{fb} is the flatband potential[1], i.e. the potential where the potential drop over the semiconductor vanishes (no energy band bending due to surface charges) and κ is the well-known inverse Debye length (cf. Eq. 2.16) with the only difference that N^0 is replaced by the donor concentration, N_D, and $z = 1$. For the important case of depletion, Eq. B.1 can be linearized according to

$$C^0_{sc} = \frac{1}{2}\epsilon_r \epsilon_0 \kappa \left[(E - E_{fb}) - \frac{k_B T}{e_0}\right]^{-1/2} \tag{B.2}$$

From this, one obtains the Mott-Schottky relation:

$$\frac{1}{C^{02}_{cs}} = \left[\frac{2}{\epsilon_r \epsilon_0 \kappa}\right]^2 \left[(E - E_{fb}) - \frac{k_B T}{e_0}\right] \tag{B.3}$$

A plot of $1/{C^0_{sc}}^2$ over E for a n-type semiconductor should be a straight line with a positive slope, while a negative slope is expected for a p-type semiconductor. The intersection with the E axis, i.e. for $1/{C^0_{sc}}^2 = 0$, occurs at $E \approx E_{fb}$, because $k_B T/e_0 \cong 25\,\text{mV}$ and hence (almost) negligible.[296]

Materials and Methods

We performed PDEIS in PBS (0.150 M NaCl, 0.016 M Na_2HPO_4, 0.004 M KH_2PO_4, pH 7.4) with 50 μm diameter IrO_x electrodes 4 days after the electrodeposition. Details about the processing are given in Section 3.3.3. Prior to experiments, the open-circuit potential (OCP) was determined. The experimental protocol consisted of 10 initial CV cycles applied between −1.1 and 0.8 V followed by EIS measurements with ac signals of 10 mV (rms) applied between 1–10^5 Hz. Spectra were recorded at different dc potentials starting at 0.8 and stepping down to −1.1 V in steps of 0.1 V. Before recording each spectrum, the respective dc potential was fixed for 10 s to reach steady-state. Analysis of the spectra was performed by NLSF to the equivalent circuit shown in Fig. 4.7. Measurements were made using an Autolab PSTAT302N potentiostat with integrated frequency response analyzer controlled by the NOVA software (Ecochemie, Netherlands). We used OriginPro 8.5 (Originlab, USA) and ZView (Scribner, USA) for the data analysis and the NLSF of the EIS spectra, respectively.

[1] The E_{fb} corresponds to the potential of zero charge, E_{pzc}.

Results and Discussion

Fig. B.1 shows the potential-dependence of the six circuit elements employed to model the small-signal ac behavior of the IrO_x electrode. The data are shown as best fit values ± error estimates determined from testing the change in the goodness of fit, i.e. the sum of squares (= average percentage error between the original data points and the calculated values). The OCP was established at $-0.2\,V$. Close to this value, the series resistance, R_s, switches from a low to a high resistive state upon decreasing the electrode potential. In contrast, the CPE and pseudocapacitance experience a sharp decrease in magnitude as described by T_{CPE} and C_ϕ, respectively. At the same time, the phase transition is marked by a sharp peak in R_{ct} and a pronounced dip in α. For the sake of completeness, we also provide the parasitic capacitance C_i. Normally, it shouldn't depend on the electrode potential, but obviously it does as evidenced by a peak at the transition point. This may be related to the fact that the proposed equivalent circuit does not entirely describe all effects taking place at the interface. Especially interdependencies between the different phenomena may lead to slightly erroneous fits.

The observed phase change is considered to be related to a metal-to-semiconductor transition with decreasing potential where the oxidized form, $IrO_x(OH)_{3-x}$, (Eq. 4.10) displays metallic behavior and its reduce form, $Ir(OH)_3$, has semiconducting characteristics [297–299]. In order to validate this, a Mott-Schottky plot is provided in Fig. B.2 with $1/T_{CPE}^2$ over E. Overlayed is the voltammetric i vs. E relation for qualitative comparison. We can identify three distinct regions: Region I corresponds to the metallic-like state characterized by a large capacitance and presence of faradaic processes. With decreasing potential, in region II, a sharp and linear rise in $1/T_{CPE}^2$ can be observed, which coincides with the appearance of the voltammetric reduction peak at around $-0.2\,V$ marking the transition $Ir(IV) \longrightarrow Ir(III)$.

The linear Mott-Schottky behavior of IrO_x has been described in literature [297] and attributed to a p-type semiconducting character, which also explains the increase in R_s with decreasing potential. The intersection of the linear fit of region II with the E-axis results in $E_{fb} \approx -0.2\,V$ and hence coincides with the OCP. With decreasing potential, in region III, the capacitance increases again. We attribute this increase to faradaic rather than electrostatic processes, including H adsorption. Noticeable is that α exhibits a pronounced minimum at -0.1 V and hence close to E_{fb}. The system therefore exhibits the strongest frequency dispersion close to E_{fb} and hence the potential of zero charge. This behavior cannot be explained solely on the basis of structural irregularities as often assumed for the origin of the CPE, but clearly is also related to the chemical composition and charge distribution at the interface. Unfortunately, at this moment we cannot provide a valid explanation of the physical processes leading to the potential-dependence of α. The sudden increase of R_{ct} at $-0.1\,V$ and hence close to E_{fb} may be attributed to the absence

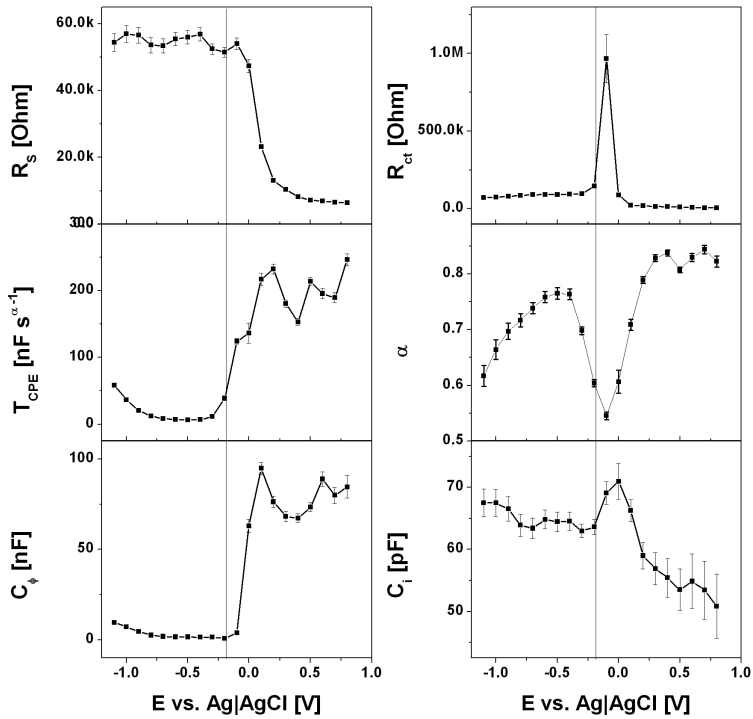

Fig. B.1: Potentiodynamic behavior of the equivalent circuit parameters of an IrO_x electrode. Vertical lines mark the open-circuit potential.

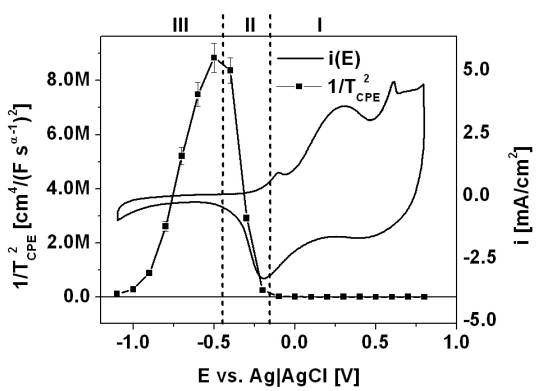

Fig. B.2: Mott-Schottky plot, $1/T^2_{CPE}$ vs. E, and voltammetric i vs. E response of an IrO_x electrode. The dashed vertical lines separate three distinct regions: Region I describes the metallic (faradaic) behavior, region II marks the linear behavior of a p-type semiconductor, and region III represents the semiconducting region under the influence of H adsorption.

of an interfacial electric field that can promote charge-transfer.

Summary

We have employed PDEIS to study the interfacial processes occurring at an anodically electrodeposited IrO_x electrode. The increase in film resistance and decrease in interfacial capacitance with decreasing electrode potential was attributed to a metal-to-semiconductor phase transition. From the linear Mott-Schottky potential-dependence of T_{CPE} we could deduce a p-type semiconducting behavior below the flatband potential, which was identified at $-0.2\,V$ vs. Ag|AgCl. Close to this potential, the system exhibits a strong frequency dispersion as evidenced by a pronounced minimum in α. Further, the R_{ct} was maximum close to E_{fb} and hence in the absence of an interfacial electric field. The direct implications of the above results for neural recording or stimulation with IrO_x electrodes remain largely elusive at the moment. It is clear, however, that the majority of the charge transfer with IrO_x electrodes takes place at anodic potentials and hence at potentials, which are least efficient for neural stimulation. Reported strategies to overcome this shortcoming employed an anodic dc electrode bias during CF stimulation [170,300]. Unfortunately, such an electrode bias also drives a dc current across the interface, which may damage the electrode and tissue during chronic operation.

Appendix C

Supporting Information to Section 4.4.3

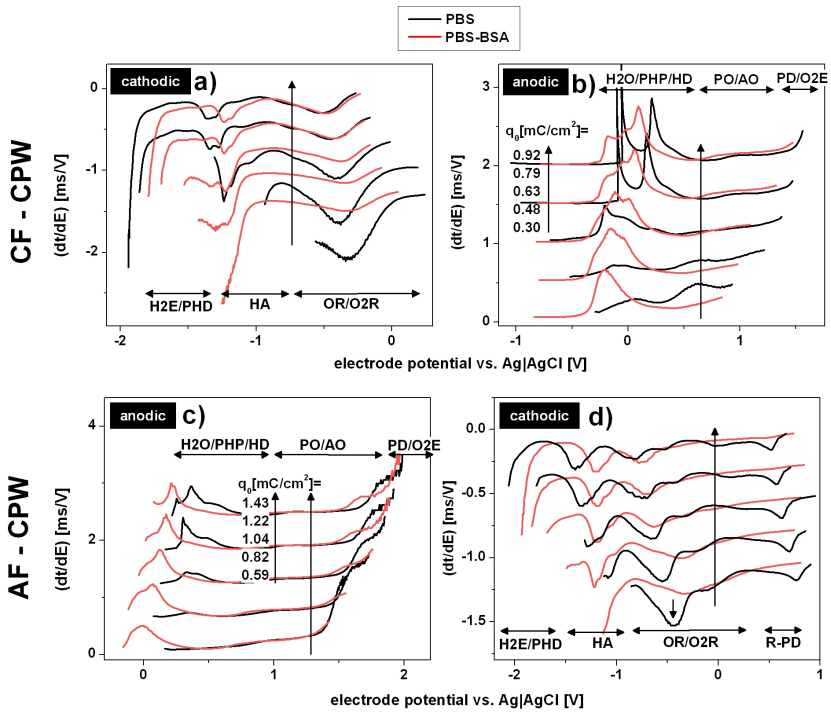

Fig. C.1: Series of $dt/dE(E)$ plots obtained in response to constant-pulse-width (CPW) stimulation of a 50 μm diameter Pt electrode in PBS and PBS-BSA. (a, b) Cathodic-first (CF) stimulation; (c, d) anodic-first (AF) stimulation. Only a selection of all applied (absolute) charge densities, q_0, is shown. Graphs are stacked by a constant offset. Regions of Pt-specific reactivity are indicated by horizontal arrows. Long vertical arrows point in the direction of increasing q_0. The short vertical arrow in (d) marks the peak identified as O_2 reduction.

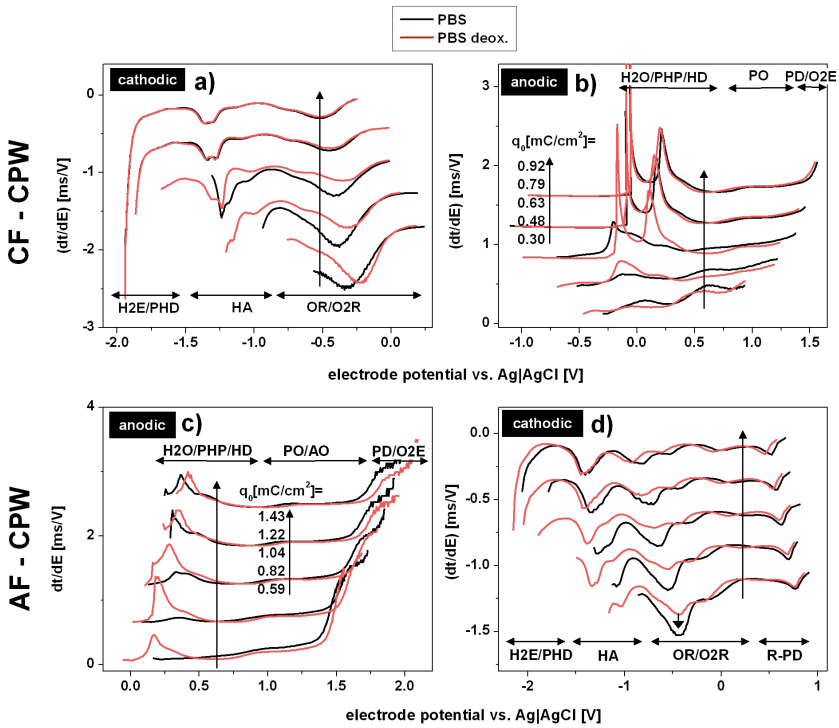

Fig. C.2: Series of $dt/dE(E)$ plots obtained in response to constant-pulse-width (CPW) stimulation of a 50 μm diameter Pt electrode in PBS and PBS_{deox}. (a, b) Cathodic-first (CF) stimulation; (c, d) anodic-first (AF) stimulation. Only a selection of all applied (absolute) charge densities, q_0, is shown. Graphs are stacked by a constant offset. Regions of Pt-specific reactivity are indicated by horizontal arrows. Long vertical arrows point in the direction of increasing q_0. The short vertical arrow in (d) marks the peak identified as O_2 reduction.

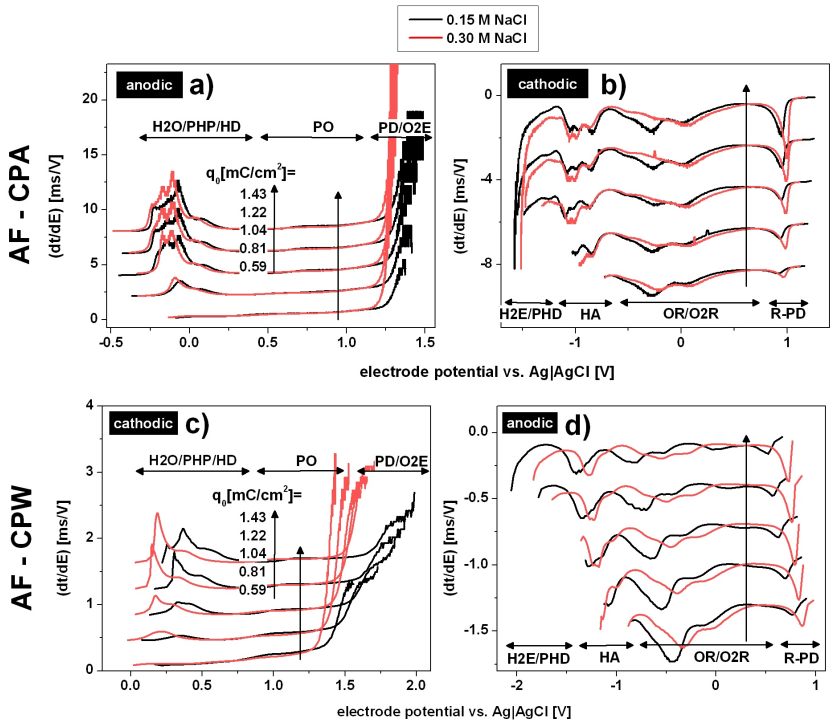

Fig. C.3: Series of $dt/dE(E)$ plots obtained in response to anodic-first (AF) stimulation of 50 μm diameter Pt electrodes in PBS with 0.15 and 0.3 M NaCl. (a, b) constant-pulse-amplitude (CPA) stimulation; (c, d) constant-pulse-width (CPW) stimulation. Only a selection of all applied (absolute) charge densities, q_0, is shown. Graphs are stacked by a constant offset. Regions of Pt-specific reactivity are indicated by horizontal arrows. Long vertical arrows point in the direction of increasing q_0. An increased cathodic R-PD peak is observed in 0.3 M NaCl PBS and can be attributed to the the higher Pt dissolution rate in the preceding anodic phase compared to 0.15 M NaCl PBS. Also part of the OR/O2R signal is suppressed in 0.3 M NaCl PBS compared to 0.15 M NaCl PBS because more Cl^- ions are present to block reactive sites on the Pt surface.

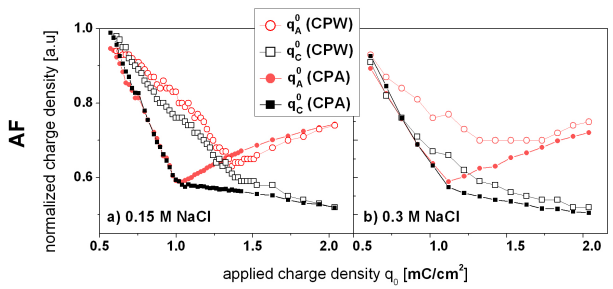

Fig. C.4: Normalized charge densities for reciprocal derivative chronopotentiometry with anodic-first (AF) stimulation using either a constant pulse width (CPW) or amplitude (CPA) in PBS of (a) 0.15 M NaCl and (b) 0.30 M NaCl. For CPW stimulation, the divergence of q_A^0 and q_C^0 prior to the minimum of q_A^0 is stronger in 0.3 M Cl^- PBS and may be attributed to the higher Pt dissolution rate and hence irreversible charge loss compared to 0.15 M Cl^- PBS. In comparison, no such changes are observed for CPA stimulation, which may either indicate that CPA stimulation is less prone to Pt dissolution or is more effective in reversing the Pt dissolution products.

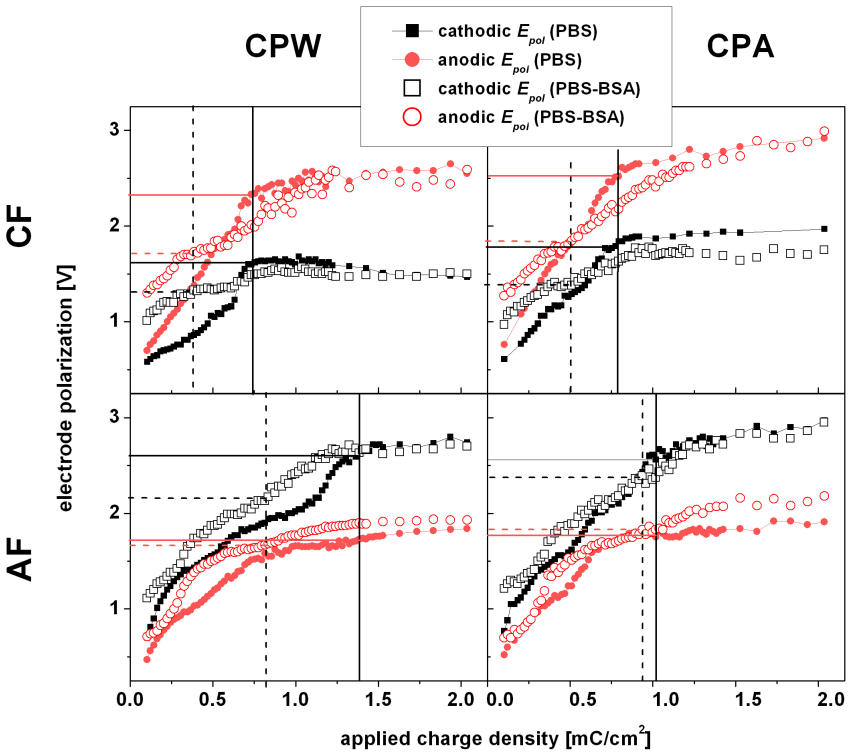

Fig. C.5: Absolute cathodic and anodic electrode polarizations, E^C_{pol} and E^A_{pol}, respectively, obtained in PBS and PBS-BSA for a range of applied charge densities, q_0. Stimulation conditions were anodic-first (AF) or cathodic-first (CF) at either constant pulse width (CPW) or amplitude (CPA). Vertical solid and dashed lines mark the onset of irreversible gas evolution in PBS and PBS-BSA, respectively, as determined in Fig. 4.16. Pairs of vertical solid (PBS) and dashed (PBS-BSA) lines indicate the anodic and cathodic E_{pol} values at the onset of irreversible gas evolution.

Appendix D

Lithography protocols

Pt lift-off	
spin HMDS	3000 rpm, 500 rpm/s ramp, 30 s
spin LOR5A	3000 rpm, 500 rpm/s ramp, 30 s
cure	5 min, 180° on hotplate
spin IX845	3000 rpm, 500 rpm/s ramp, 30 s
cure	3 min, 105° on hotplate
expose	5.5 s (MA6), hard contact
develop	1 min 30 s in OPD262
metal deposition	Ti/Pt/20 (20 nm/200 nm/20 nm)
lift-off	10 min in hot acetone or hot microstrip + 10 min with ultrasonic; 5 min in OPD262
etch mask for Parylene C	
spin HMDS	3000 rpm, 500 rpm/s ramp, 30 s
spin IX845	1500 rpm, 500 rpm/s ramp, 30 s
cure	3 min, 150° on hotplate
expose	7.5 s (MA6), hard contact
develop	1 min 30 s in OPD262
etch mask for frontside DRIE	
spin HMDS	3000 rpm, 500 rpm/s ramp, 30 s
spin AZ4563	1500 rpm, 500 rpm/s, 9 sec
wait	10 min
cure	5 min, 90° on hotplate
spin AZ4563	1500 rpm, 500 rpm/s, 9 sec
wait	10 min
cure	10 min, 105° on hotplate
wait	2 h for rehydration
exposure	105 s (MA6), hard contact
develop	6–7 min in 351:H_2O (1:3)

Bibliography

[1] Wise, K.D.; Angell, J.B.; Starr, A., An integrated-circuit approach to extracellular microelectrodes, *IEEE T. Bio-Med. Eng.* **1970**, *17*, 238–247.

[2] Kipke, D.R.; Shain, W.; Buzsáki, G.; Fetz, E.; Henderson, J.M.; Hetke, J.F.; Schalk, G., Advanced neurotechnologies for chronic neural interfaces: new horizons and clinical opportunities., *J. Neurosci.* **2008**, *28*(46), 11830–11838.

[3] Rousche, P.J.; Normann, R.A., Chronic recording capability of the Utah Intracortical Electrode Array in cat sensory cortex, *J. Neurosci. Methods* **1998**, *82*, 1–15.

[4] Liu, X.; McCreery, D.; Carter, R.; Bullara, L.; Yuen, T.; Agnew, W., Stability of the interface between neural tissue and chronically implanted intracortical microelectrodes, *IEEE Trans. Rehab. Eng.* **1999**, *7*, 315–326.

[5] Csicsvari, J.; Henze, D.A.; Jamieson, B.; Harris, K.D.; Sirota, A.; Bartho, P.; Wise, K.D.; Buzsaki, G., Massively parallel recording of unit and local field potentials with silicon-based electrodes, *J. Neurophysiol.* **2003**, *90*, 1314–1323.

[6] Kipke, D.R.; Vetter, R.J.; Williams, J.C.; Hetke, J.F., Silicon-substrate intracortical microelectrode arrays for long-term recording on neuronal spike activity in cerebral cortex, *IEEE Trans. Rehab. Eng.* **2003**, *11*, 151–155.

[7] Nicolelis, M.A.L.; Dimitrov, D.; Carmena, J.M.; Crist, R.; Lehew, G.; Kralik, J.D.; Wise, S.P., Chronic, multisite, multielectrode recordings in macaque monkeys, *Proc. Natl. Acad. Sci. U. S. A.* **2003**, *100*(19), 11041–11046.

[8] McCreery, D.; Pikov, V.; Lossinsky, A.; Bullara, L.; Agnew, W., Arrays for chronic functional micro stimulation of the lumbosacral spinal cord, *IEEE T. Neur. Sys. Reh.* **2004**, *12*(2), 195–207.

[9] Buzsaki, G., Large-scale recording of neuronal ensembles, *Nat. Neurosci.* **2004**, *7*(5), 446–451.

[10] Suner, S.; Fellows, M.R.; Vargas-Irwin, C.; Nakata, G.K.; Donoghue, J.P., Reliability of signals from a chronically implanted, silicon-based electrode array in non-human primate primary motor cortex, *IEEE T. Neur. Sys. Reh.* **2005**, *13*(4), 524–541.

[11] Jackson, A.; Mavoori, J.; Fetz, E.E., Long-term motor cortex plasticity induced by an electronic neural implant, *Nature* **2006**, *444*(7115), 56–60.

[12] Du, J.; Riedel-Kruse, I.H.; Nawroth, J.C.; Roukes, M.L.; Laurent, G.; Masmanidis, S.C., High-Resolution Three-Dimensional Extracellular Recording of Neuronal Activity With Microfabricated Electrode Arrays, *J. Neurophysiol.* **2009**, *101*(3), 1671–1678.

[13] Schmidt, R.; Diba, K.; C., L.; D., S.; G., B.; R., K., Single-Trial Phase Precession in the Hippocampus, *J. Neurosci.* **2009**, *29*(42), 13232–13241.

[14] Montgomery, S.; Betancur, M.; G., B., Behavior-Dependent Coordination of Multiple Theta Dipoles in the Hippocampus, *J. Neurosci.* **2009**, *29*(5), 1381–1394.

[15] Robblee, L.S.; Rose, T.L., Electrochemical guidelines for selection of protocols and electrode materials for neural stimulation., in W.F. Agnew; D.B. McCreery, eds., *Neural Prostheses: Fundamental Studies*, Prentice Hall, Englewood Cliffs, NJ, **1990**.

[16] Merrill, D.; Merrill, D.; Tresco, P., Impedance characterization of microarray recording electrodes in vitro, *IEEE T. Bio-Med. Eng.* **2005**, *52*(11), 1960–1965.

[17] Cogan, S.F., Neural Stimulation and Recording Electrodes, *Annu. Rev. Biomed. Eng.* **2008**, *10*(1), 275–309.

[18] Lempka, S.; Miocinovic, S.; Johnson, M.; Vitek, J.; McIntyre, C., In vivo impedance spectroscopy of deep brain stimulation electrodes, *J. Neural Eng.* **2009**, *6*(4), 046001.

[19] Jochum, T.; Denison, T.; Wolf, P., Integrated circuit amplifiers for multi-electrode intracortical recording, *J. Neural Eng.* **2009**, *6*(1), 012001–012026.

[20] Meyer, R.D.; Cogan, S.F.; Nguyen, T.H.; Rauh, R.D., Electrodeposited iridium oxide for neural stimulation and recording electrodes, *IEEE Trans. Neural Syst. Rehab. Eng.* **2001**, *9*, 2–11.

[21] Keefer, E.W.; Botterman, B.R.; Romero, M.I.; Rossi, A.F.; Gross, G.W., Carbon nanotube coating improves neuronal recordings., *Nat. Nanotechnol.* **2008**, *3*(7), 434–439.

[22] Abidian, M.R.; Martin, D.C., Multifunctional Nanobiomaterials for Neural Interfaces, *Adv. Funct. Mater.* **2009**, *19*(4), 573–585.

[23] Shain, W.; Spataro, L.; Dilgen, J.; Haverstick, K.; Retterer, S.; Isaacson, M.; Saltzman, M.; Turner, J., Controlling cellular reactive responses around neural prosthetic devices using peripheral and local intervention strategies, *IEEE T. Neur. Sys. Reh.* **2003**, *11*(2), 186–188.

[24] Bjornsson, S.J.; Oh, Y.A.; Al-Kofahi, Y.J.; Lim, K.L.; Smith, J.N.; Turner, S.; De, B.; Roysam, W.S.; Kim, S.J., Effects of insertion conditions on tissue strain and vascular damage during neuroprosthetic device insertion, *J. Neural Eng.* **2006**, *3*, 196–207.

[25] Zhong, Y.H.; Bellamkonda, R.V., Dexamethasone-coated neural probes elicit attenuated inflammatory response and neuronal loss compared to uncoated neural probes, *Brain Res.* **2007**, *1148*, 15–27.

[26] Benabid, A.L.; Pollak, P.; Gao, D.M.; Hoffmann, D.; Limousin, P.; Gay, E.; Payen, I.; Benazzouz, A., Chronic electrical stimulation of the ventralis intermedius nucleus of the thalamus as a treatment of movement disorders, *J. Neurosurg.* **1996**, *84*(2), 203–214.

[27] Nuttin, B.J.; Gabriels, L.A.; Cosyns, P.R.; Meyerson, B.A.; Andreewitch, S.; Sunaert, S.G.; Maes, A.F.; Dupont, P.J.; Gybels, J.M.; Gielen, F.; Demeulemeester, H.G., Long-term electrical capsular stimulation in patients with obsessive-compulsive disorder, *Neurosurgery* **2003**, *52*, 1263–1272.

[28] Kringelbach, M.L.; Jenkinson, N.; Owen, S.L.; Aziz, T.Z., Translational principles of deep brain stimulation, *Nat. Rev. Neurosci.* **2007**, *8*(8), 623–635.

[29] Gubellini, P.; Salin, P.; Kerkerian-Le Goff, L.; Baunez, C., Deep brain stimulation in neurological diseases and experimental models: From molecule to complex behavior, *Progr. Neurobiol.* **2009**, *89*(1), 79–123.

[30] Najafi, K.; Wise, K.; Mochizuki, T., A high-yield IC-compatible multichannel recording array, *IEEE T. Electron. Dev.* **1985**, *32*(7), 1206–1211.

[31] Norlin, P.; Kindlundh, M.; Mouroux, A.; Yoshida, K.; Hofmann, U., A 32-site neural recording probe fabricated by DRIE of SOI substrates, *J. Micromech. Microeng.* **2002**, *12*, 414–419.

[32] Cheung, K.C.; Djupsund, K.; Dan, Y.; Lee, L.P., Implantable multichannel electrode array based on SOI technology, *J. Microelectromech. Syst.* **2003**, *12*, 179–184.

[33] Seymour, J.P.; Kipke, D.R., Neural probe design for reduced tissue encapsulation in CNS, *Biomaterials* **2007**, *28*(25), 3594–3607.

[34] Chen, J.; Wise, K.; Hetke, J.; Bledsoe, S.C., J., A multichannel neural probe for selective chemical delivery at the cellular level, *IEEE T. Bio-Med. Eng.* **1997**, *44*, 760–769.

[35] Seidl, K.; Spieth, S.; Herwik, S.; Steigert, J.; Zengerle, R.; Paul, O.; Ruther, P., In-plane silicon probes for simultaneous neural recording and drug delivery, *J. Micromech. Microeng.* **2010**, *20*(10), 105006–105016.

[36] Bai, Q.; Wise, K.D.; Anderson, D.J., A high-yield microassembly structure for three-dimensional microelectrode arrays, *IEEE T. Bio-Med. Eng.* **2000**, *47*, 281–289.

[37] Aarts, A.A.A.; Neves, H.P.; Puers, R.P.; Van Hoof, C., An interconnect for out-of-plane assembled biomedical probe arrays, *J. of Micromech. Microeng.* **2008**, 064004–06409.

[38] Sodagar, A.; Wise, K.; Najafi, K., A Fully Integrated Mixed-Signal Neural Processor for Implantable Multichannel Cortical Recording, *IEEE T. Bio-Med. Eng.* **2007**, *54*(6), 1075–1088.

[39] Campbell, P.; Jones, K.; Huber, R.; Horch, K.; Normann, R., A silicon-based, three-dimensional neural interface: manufacturing processes for an intracortical electrode array, *IEEE Trans. Bio-Med. Eng.* **1991**, *38*(8), 758–768.

[40] Hochberg, L.R.; Serruya, M.D.; Friehs, G.M.; Mukand, J.A.; Saleh, M.; Caplan, A.H.; Branner, A.; Chen, D.; Penn, R.D.; Donoghue, J.P., Neuronal ensemble control of prosthetic devices by a human with tetraplegia, *Nature* **2006**, *442*(7099), 164–171.

[41] Boyden, E.S.; Zhang, F.; Bamberg, E.; Nagel, G.; Deisseroth, K., Millisecond-timescale, genetically targeted optical control of neural activity., *Nat. Neurosci.* **2005**, *8*(9), 1263–1268.

[42] Adamantidis, A.R.; Zhang, F.; Aravanis, A.M.; Deisseroth, K.; de Lecea, L., Neural substrates of awakening probed with optogenetic control of hypocretin neurons, *Nature* **2007**, *450*(7168), 420–424.

[43] Han, X.; Qian, X.; Bernstein, J.G.; Zhou, H.h.; Franzesi, G.T.; Stern, P.; Bronson, R.T.; Graybiel, A.M.; Desimone, R.; Boyden, E.S., Millisecond-Timescale Optical Control of Neural Dynamics in the Nonhuman Primate Brain, *Neuron* **2009**, *62*(2), 191–198.

[44] Zhang, J.; Laiwalla, F.; Kim, J.; Urabe, H.; Van Wagenen, R.; Song, Y.K.; Connors, B.; Zhang, F.; Deisseroth, K.; Nurmikko, A., Integrated device for optical stimulation and spatiotemporal electrical recording of neural activity in light-sensitized brain tissue, *J. Neural Eng.* **2009**, *6*(5), 055007–0055019.

[45] Royer, S.; Zemelman, B.V.; Barbic, M.; Losonczy, A.; BuzsÃąki, G.; Magee, J.C., Multi-array silicon probes with integrated optical fibers: light-assisted perturbation and recording of local neural circuits in the behaving animal, *Eur. J. Neurosci.* **2010**, *31*(12), 2279–2291.

[46] Cho, I.J.; Baac, H.W.; Yoon, E., A 16-site neural probe integrated with a waveguide for optical stimulation, *Proc. Annu. Int. Conf. IEEE MEMS* **2010**, 995–8.

[47] Im, M.; Cho, I.J.; Wu, F.; Wise, K.; Yoon, E., Neural probes integrated with optical mixer/splitter waveguides and multiple stimulation sites, *Proc. Annu. Int. Conf. IEEE MEMS* **2011**, 1051–1054.

[48] Meissner, W.; Leblois, A.; Hansel, D.; Bioulac, B.; Gross, C.E.; Benazzouz, A.; Boraud, T., Subthalamic high frequency stimulation resets subthalamic firing and reduces abnormal oscillations, *Brain* **2005**, *128*(10), 2372–2382.

[49] Shi, L.H.; Luo, F.; Woodward, D.J.; Chang, J.Y., Basal ganglia neural responses during behaviorally effective deep brain stimulation of the subthalamic nucleus in rats performing a treadmill locomotion test, *Synapse* **2006**, *59*(7), 445–457.

[50] Martens, H.C.F.; Toader, E.; Decre, M.M.J.; Anderson, D.J.; Vetter, R.; Kipke, D.R.; Baker, K.B.; Johnson, M.D.; Vitek, J.L., Spatial steering of deep brain stimulation volumes using a novel lead design, *Clin. Neurophysiol.* **2011**, *122*(3), 558–566.

[51] Schmickler, W.; Santos, E., *Interfacial Electrochmistry*, Springer, Heidelberg, 2nd edition, **2010**.

[52] von Helmholtz, H., Ueber einige Gesetze der Vertheilung elektrischer Ströme in körperlichen Leitern mit Anwendung auf die thierisch-elektrischen Versuche, *Ann. Phys. Chem.* **1853**, *165*, 211–233.

[53] Gouy, G., Constitution of the electric charge at the surface of an electrolyte, *J. Physique* **1910**, *9*, 457–467.

[54] Chapman, D., A contribution to the theoray of electrocapillarity, *Philos. Mag.* **1913**, *25*, 475–481.

[55] H.-J. Butt, K.G.; Kappl, M., *Physics and chemistry of interfaces*, Wiley-VCH, Weinheim, **2003**.

[56] Stern, O., Zur theorie der elektrolytischen doppelschicht., *Z. Elektrochem.* **1924**, *30*, 508–516.

[57] Bockris, J.O.; Reddy, A.K., *Modern Electrochemistry 2*, Plenum Press, New York, **1973**.

[58] Norde, W., *Colloids and Interfaces in Life Sciences*, Marcel Dekker, New York, **2003**.

[59] Gellings, P.; Bouwmeester, H., eds., *The CRC Handbook of Solid State Electrochemistry*, CRC Press, Boca Raton, **1996**.

[60] Bard, A.; Faulkner, L., *Electrochemical Methods*, Wiley & Sons, New York, **2001**.

[61] Plonsey, R.; Barr, R., *Bioelectricity - A quantitative approach*, Springer, New York, 3rd edition, **2007**.

[62] Hentall, I.D.; Zorman, G.; Kansky, S.; Fields, H.L., Relations among threshold, spike height, electrode distance, and conduction velocity in electrical stimulation of certain medullospinal neurons, *J. Neurophysiol.* **1984**, *51*(5), 968–977.

[63] Grill, W.M.; Mortimer, J.T., The effect of stimulus pulse duration on selectivity of neural stimulation., *IEEE T. Bio-Med. Eng.* **1996**, *43*(2), 161–166.

[64] Tehovnik, E.J., Electrical stimulation of neural tissue to evoke behavioral responses, *J. Neurosci. Methods* **1996**, *65*(1), 1–17.

[65] Rattay, F.; Resatz, S., Dipole Distance for Minimum Threshold Current to Stimulate Unmyelinated Axons With Microelectrodes, *IEEE T. Bio-Med. Eng.* **2007**, *54*(1), 158–162.

[66] Wagenaar, D.A.; Pine, J.; Potter, S.M., Effective parameters for stimulation of dissociated cultures using multi-electrode arrays, *J. Neurosci. Methods* **2004**, *138*(1-2), 27–37.

[67] Joucla, S.; Yvert, B., Improved focalization of electrical microstimulation using microelectrode arrays: a modeling study., *PLoS One* **2009**, *4*(3), e4828.

[68] Butler, J., Studies in heterogeneous equilibria. Part II. – The kinetic interpretation of the nernst theory of electromotive force, *Trans. Faraday Soc.* **1924**, *19*, 729–733.

[69] Erdey-Gruz, T.; Volmer, M., *Z. Physik. Chem.* **1930**, *150*, 203.

[70] Neuman, M.R., Biopotential Electrodes, in J.D. Bronzino, ed., *The Biomedical Engineering Handbook*, CRC Press, Boca Raton, 2nd edition, **2000**.

[71] Saito, Y., A Theoretical Study on the Diffusion Current at the Stationary Electrodes of Circular and Narrow Band Types, *Rev. Polarog. (Jap.)* **1968**, *15*, 177–187.

[72] Brummer, S.B.; Turner, M.J., Electrical Stimulation with Pt Electrodes: II. Estimation of Maximum Surface Redox (Theoretical Non-Gassing) Limits, *IEEE T. Bio-Med. Eng.* **1977**, *24*(5), 440–443.

[73] Brummer, S.B.; McHardy, J.; Turner, M.J., Electrical-Stimulation With Pt Electrodes - Trace Analysis For Dissolved Platinum And Other Dissolved Electrochemical Products, *Brain Behavior And Evolution* **1977**, *14*(1-2), 10–22.

[74] Black, R.; Hannaker, P., Dissolution of Smooth Platinum Electrodes in Biological Fluids, *Appl. Neurophysiol.* **1979**, *42*(6), 366–374.

[75] McHardy, J.; Robblee, L.; Marston, J.; Brummer, S., Electrical stimulation with Pt electrodes. IV. Factors influencing Pt dissolution in inorganic saline, *Biomaterials* **1980**, *1*(3), 129 – 134.

[76] Robblee, L.; McHardy, J.; Agnew, W.; Bullara, L., Electrical stimulation with Pt electrodes. VII. Dissolution of Pt electrodes during electrical stimulation of the cat cerebral cortex, *J. Neurosci. Methods* **1983**, *9*(4), 301 – 308.

[77] Rose, T.L.; Robblee, L.S., Electrical-Stimulation With Pt Electrodes .8. Electrochemically Safe Charge Injection Limits With 0.2 Ms Pulses, *IEEE T. Bio-Med. Eng.* **1990**, *37*(11), 1118–1120.

[78] Morton, S.L.; Daroux, M.L.; Mortimer, J.T., The Role of Oxygen Reduction in Electrical Stimulation of Neural Tissue, *J. Electrochem. Soc.* **1994**, *141*(1), 122–130.

[79] Huang, C.Q.; Carter, P.M.; Shepherd, R.K., Stimulus induced pH changes in cochlear implants: An in vitro and in vivo study, *Ann. Biomed. Eng.* **2001**, *29*(9), 791–802.

[80] Cogan, S.F.; Guzelian, A.A.; Agnew, W.F.; Yuen, T.G.H.; McCreery, D.B., Over-pulsing degrades activated iridium oxide films used for intracortical neural stimulation, *J. Neurosci. Methods* **2004**, *137*(2), 141–150.

[81] Cogan, S.; Ehrlich, J.; Plante, T.; Gingerich, M.; Shire, D., Contribution of Oxygen Reduction to Charge Injection on Platinum and Sputtered Iridium Oxide Neural Stimulation Electrodes, *IEEE T. Bio-Med. Eng.* **2010**, *57*(9), 2313–2321.

[82] Trasatti, S., Work function, electronegativity, and electrochemical behaviour of metals: III. Electrolytic hydrogen evolution in acid solutions, *J. Electroanal. Chem. and Interfacial Electrochem.* **1972**, *39*(1), 163–184.

[83] Feldberg, S.W.; Enke, C.G.; Bricker, C.E., Formation and Dissolution of Platinum Oxide Film: Mechanism and Kinetics, *J. Electrochem. Soc.* **1963**, *110*(7), 826–834.

[84] Conway, B.E., Electrochemical oxide film formation at noble metals as a surface-chemical process, *Prog. Surf. Sci.* **1995**, *49*(4), 331–452.

[85] Jerkiewicz, G., Surface Oxidation of Noble Metal Electrodes, in A. Wieckowski, ed., *Interfacial Electrochemistry: Theory, Experiment, and Applications*, Marcel Dekker, New Jersey, chapter 32, 559–598, **1999**.

[86] Pudenz, R.H.; Bullara, L.A.; Jacques, S.; Hambrecht, F.T., Electrical stimulation of the brain. III. The neural damage model., *Surg Neurol* **1975**, *4*(4), 389–400.

[87] Agnew, W.F.; Yuen, T.G.; Pudenz, R.H.; Bullara, L.A., Neuropathological effects of intracerebral platinum salt injections., *J. Neuropathol. Exp. Neurol.* **1977**, *36*(3), 533–546.

[88] Lilly, J.C.; Hughes, J.R.; Alvord, E.C.; Galkin, T.W., Brief, Noninjurious Electric Waveform For Stimulation of the Brain, *Science* **1955**, *121*(3144), 468–469.

[89] Valenstein, E.S.; Beer, B., Unipolar and bipolar electrodes in self-stimulation experiments., *Am J Physiol* **1961**, *201*, 1181–1186.

[90] Wetzel, M.C., The identification of self-stimulation elements for adjacent electrodes in the cat., *Physiol Behav* **1970**, *5*(8), 899–905.

[91] Ranck, J.B., Which Elements Are Excited In Electrical-Stimulation Of Mammalian Central Nervous-System - Review, *Brain Res.* **1975**, *98*(3), 417–440.

[92] Rattay, F., The basic mechanism for the electrical stimulation of the nervous system, *Neuroscience* **1999**, *89*(2), 335–346.

[93] McIntyre, C.C.; Grill, W.M., Selective microstimulation of central nervous system neurons., *Ann Biomed Eng* **2000**, *28*(3), 219–233.

[94] Tehovnik, E.J.; Tolias, A.S.; Sultan, F.; Slocum, W.M.; Logothetis, N.K., Direct and indirect activation of cortical neurons by electrical microstimulation, *J. Neurophysiol.* **2006**, *96*(2), 512–521.

[95] Nitsche, M.A.; Paulus, W., Excitability changes induced in the human motor cortex by weak transcranial direct current stimulation., *J Physiol* **2000**, *527 Pt 3*, 633–639.

[96] Manola, L.; Holsheimer, J.; Veltink, P.; Buitenweg, J.R., Anodal vs cathodal stimulation of motor cortex: A modeling study, *Clin. Neurophysiol.* **2007**, *118*(2), 464–474.

[97] Wongsarnpigoon, A.; Grill, W.M., Computational modeling of epidural cortical stimulation., *J. Neural Eng.* **2008**, *5*(4), 443–454.

[98] Yazdan-Shahmorad, A.; Lehmkuhle, M.J.; Gage, G.J.; Marzullo, T.C.; Parikh, H.; Miriani, R.M.; Kipke, D.R., Estimation of electrode location in a rat motor cortex by laminar analysis of electrophysiology and intracortical electrical stimulation, *Journal of Neural Engineering* **2011**, *8*(4), 046018.

[99] Macherey, O.; van Wieringen, A.; Carlyon, R.; Deeks, J.; Wouters, J., Asymmetric Pulses in Cochlear Implants: Effects of Pulse Shape, Polarity, and Rate, *JARO* **2006**, *7*(3), 253–266.

[100] Benabid, A.L.; Wallace, B.; Mitrofanis, J.; Xia, C.; Piallat, B.; Fraix, V.; Batir, A.; Krack, P.; Pollak, P.; Berger, F., Therapeutic electrical stimulation of the central nervous system, *Comptes Rendus Biologies* **2005**, *328*(2), 177–186.

[101] Williams, D.F., *The Williams dictionary of biomaterials*, Liverpool University Press, Liverpool, **1999**.

[102] Ratner, B.D.; Hoffman, A.S.; Schoen, F.J.; Lemons, J.E., eds., *Biomaterials Science: An Introduction to Materials in Medicine*, Elsevier, Amsterdam, 2nd edition, **2004**.

[103] Dymond, A.M., Characteristics of Metal-tissue Interface of Stimulation Electrodes, *IEEE T. Bio-Med. Eng.* **1976**, *23*(4), 274–280.

[104] Stensaas, S.S.; Stensaas, L.J., Histopathological evaluation of materials implanted in the cerebral cortex., *Acta Neuropathol.* **1978**, *41*(2), 145–155.

[105] Majji, A.B.; Humayun, M.S.; Weiland, J.D.; Suzuki, S.; DaAnna, S.A.; de Juan, E., Long-Term Histological and Electrophysiological Results of an Inactive Epiretinal Electrode Array Implantation in Dogs, *Investigative Ophthalmology & Visual Science* **1999**, *40*(9), 2073–2081.

[106] Chouard, C.H.; Pialoux, P., Biocompatibility of cochlear implants, *Bull. Acad. Natl. Med.* **1995**, *179*(3), 549–555.

[107] Niparko, J.K.; Altschuler, R.A.; Xue, X.L.; Wiler, J.A.; Anderson, D.J., Surgical implantation and biocompatibility of central nervous system auditory prostheses., *Ann. Otol. Rhinol. Laryngol.* **1989**, *98*(12 Pt 1), 965–970.

[108] George, P.M.; Lyckman, A.W.; LaVan, D.A.; Hegde, A.; Leung, Y.; Avasare, R.; Testa, C.; Alexander, P.M.; Langer, R.; Sur, M., Fabrication and biocompatibility of polypyrrole implants suitable for neural prosthetics, *Biomaterials* **2005**, *26*(17), 3511–3519.

[109] Loeb, G.E.; Bak, M.J.; Salcman, M.; Schmidt, E.M., Parylene As A Chronically Stable, Reproducible Microelectrode Insulator, *IEEE T. Bio-Med. Eng.* **1977**, *24*(2), 121–128.

[110] Schmidt, E.M.; McIntosh, J.S.; Bak, M.J., Long-term implants of Parylene-C coated microelectrodes., *Med. Biol. Eng. Comput.* **1988**, *26*(1), 96–101.

[111] Hoogerwerf, A.; Wise, K., A three-dimensional microelectrode array for chronic neural recording, *IEEE T. Bio-Med. Eng.* **1994**, *41*(12), 1136–1146.

[112] Schmidt, S.; Horch, K.; Normann, R., Biocompatibility of silicon-based electrode arrays implanted in feline cortical tissue., *J. Biomed. Mater. Res.* **1993**, *27*(11), 1393–1399.

[113] Rosenberg, B.; Vancamp, L.; Krigas, T., Inhibition of cell division in escherichia coli by electrolysis products from a platinum electrode., *Nature* **1965**, *205*, 698–699.

[114] Steinemann, S.G., Metal implants and surface reactions, *Injury* **1996**, *27*, –.

[115] Cyster, L.A.; Grant, D.M.; Parker, K.G.; Parker, T.L., The effect of surface chemistry and structure of titanium nitride (TiN) films on primary hippocampal cells, *Biomol. Eng.* **2002**, *19*(2-6), 171–175.

[116] Gawad, S.; Giugliano, M.; Heuschkel, M.; Wessling, B.; Markram, H.; Schnakenberg, U.; Renaud, P.; Morgan, H., Substrate arrays of iridium oxide microelectrodes for in vitro neuronal interfacing., *Front. Neuroeng.* **2009**, *2*, 1.

[117] Göbbels, K.; Kuenzel, T.; van Ooyen, A.; Baumgartner, W.; Schnakenberg, U.; Bräunig, P., Neuronal cell growth on iridium oxide, *Biomaterials* **2010**, *31*(6), 1055–1067.

[118] Wang, K.; Fishman, H.A.; Dai, H.J.; Harris, J.S., Neural stimulation with a carbon nanotube microelectrode array, *Nano Lett.* **2006**, *6*(9), 2043–2048.

[119] Mattson, M.P.; Haddon, R.C.; Rao, A.M., Molecular functionalization of carbon nanotubes and use as substrates for neuronal growth, *J. Mol. Neurosci.* **2000**, *14*(3), 175–182.

[120] Pantarotto, D.; Partidos, C.D.; Graff, R.; Hoebeke, J.; Briand, J.P.; Prato, M.; Bianco, A., Synthesis, structural characterization, and immunological properties of carbon nanotubes functionalized with peptides, *J. Am. Chem. Soc.* **2003**, *125*(20), 6160–6164.

[121] Lovat, V.; Pantarotto, D.; Lagostena, L.; Cacciari, B.; Grandolfo, M.; Righi, M.; Spalluto, G.; Prato, M.; Ballerini, L., Carbon nanotube substrates boost neuronal electrical signaling, *Nano Lett.* **2005**, *5*(6), 1107–1110.

[122] Liopo, A.V.; Stewart, M.P.; Hudson, J.; Tour, J.M.; Pappas, T.C., Biocompatibility of native and functionalized single-walled carbon nanotubes for neuronal interface, *J. Nanosci. Nanotechnol.* **2006**, *6*(5), 1365–1374.

[123] Smart, S.K.; Cassady, A.I.; Lu, G.Q.; Martin, D.J., The biocompatibility of carbon nanotubes, *Carbon* **2006**, *44*(6), 1034–1047.

[124] Mazzatenta, A.; Giugliano, M.; Campidelli, S.; Gambazzi, L.; Businaro, L.; Markram, H.; Prato, M.; Ballerini, L., Interfacing neurons with carbon nanotubes: Electrical signal transfer and synaptic stimulation in cultured brain circuits, *J. Neurosci.* **2007**, *27*(26), 6931–6936.

[125] Shein, M.; Greenbaum, A.; Gabay, T.; Sorkin, R.; David-Pur, M.; Ben-Jacob, E.; Hanein, Y., Engineered neuronal circuits shaped and interfaced with carbon nanotube microelectrode arrays, *Biomed. Microdevices* **2009**, *11*(2), 495–501.

[126] Lasia, A., Electrochemical Impedance Spectroscopy and Its Applications, in B.E. Conway; J. Bockris; R. White, eds., *Modern Aspects of Electrochemistry*, Kluwer Academic/Plenum publishers, New York, volume 32, 143–248, **1999**.

[127] Banks, D.J.; Balachandran, W.; Richards, P.R.; Ewins, D., Instrumentation to evaluate neural signal recording properties of micromachined microelectrodes inserted in invertebrate nerve, *Physiol. Meas.* **2002**, *23*(2), 437–448.

[128] Conway, B.E., *Electrochemical Supercapacitors*, Kluwer Academic/Plenum publishers, New York, **1999**.

[129] Conway, B.; Pell, W., Double-layer and pseudocapacitance types of electrochemical capacitors and their applications to the development of hybrid devices, *J. Solid State Electrochem.* **2003**, *7*(9), 637–644.

[130] Frackowiak, E.; Metenier, K.; Bertagna, V.; Beguin, F., Supercapacitor electrodes from multiwalled carbon nanotubes, *Appl. Phys. Lett.* **2000**, *77*(15), 2421–2423.

[131] Abidian, M.R.; Martin, D.C., Experimental and theoretical characterization of implantable neural microelectrodes modified with conducting polymer nanotubes., *Biomaterials* **2008**, *29*(9), 1273–1283.

[132] Cui, X.; Hetke, J.F.; Wiler, J.A.; Anderson, D.J.; Martin, D.C., Electrochemical deposition and characterization of conducting polymer polypyrrole/PSS on multichannel neural probes, *Sens. Actuators, A* **2001**, *93*(1), 8–18.

[133] Chen, C.H.; Su, H.C.; Chuang, S.C.; Yen, S.J.; Chen, Y.C.; Lee, Y.T.; Chen, H.; Yew, T.R.; Chang, Y.C.; Yeh, S.R.; Yao, D.J., Hydrophilic modification of neural microelectrode arrays based on multi-walled carbon nanotubes, *Nanotechnology* **2010**, *21*(48), 485501–10.

[134] Della Santina, C.C.; Kovacs, G.T.A.; Lewis, E.R., Multi-unit recording from regenerated bullfrog eighth nerve using implantable silicon-substrate microelectrodes, *J. Neurosci. Methods* **1997**, *72*(1), 71–86.

[135] Yoon, T.H.; Hwang, E.J.; Shin, D.Y.; Park, S.I.; Oh, S.J.; Jung, S.C.; Shin, H.C.; Kim, S.J., A micromachined silicon depth probe for multichannel neural recording, *IEEE T. Bio-Med. Eng.* **2000**, *47*(8), 1082–1087.

[136] Lee, K.; Massia, S.; He, J.P., Biocompatible benzocyclobutene-based intracortical neural implant with surface modification, *J. Micromech. Microeng.* **2005**, *15*(11), 2149–2155.

[137] Chen, C.H.; Yao, D.J.; Tseng, S.H.; Lu, S.W.; Chiao, C.C.; Yeh, S.R., Micro-multi-probe electrode array to measure neural signals, *Biosens. Bioelectron.* **2009**, *24*(7), 1911–1917.

[138] Janders, M.; Egert, U.; Stelzle, M.; Nisch, W., Novel thin film titanium nitride micro-electrodes with excellent charge transfer capability for cell stimulation and sensing applications, *Proc. Annu. Int. Conf. IEEE Eng. Med. Biol. Soc.* **1996**, *1*, 245–247.

[139] Gabriel, G.; Gómez-Martínez, R.; Villa, R., Single-walled carbon nanotubes deposited on surface electrodes to improve interface impedance., *Physiol. Meas.* **2008**, *29*(6), S203–S212.

[140] Johnson, M.D.; Franklin, R.K.; Scott, K.A.; Brown, R.B.; Kipke, D.R., Neural probes for concurrent detection of neurochemical and electrophysiological signals in vivo, *Proc. Annu. Int. Conf. IEEE Eng. Med. Biol. Soc.* **2005**, *1-7*, 7325–7328.

[141] Kisban, S.; Herwik, S.; Seidl, K.; Rubehn, B.; Jezzini, A.; Umilta, M.A.; Fogassi, L.; Stieglitz, T.; Paul, O.; Ruther, P. A10 Ruther, P., Microprobe Array with Low Impedance Electrodes and Highly Flexible Polyimide Cables for Acute Neural Recording, *Proc. Annu. Int. Conf. IEEE Eng. Med. Biol. Soc.* **2007**, 175–178.

[142] Moxon, K.A.; Leiser, S.C.; Gerhardt, G.A.; Barbee, K.A.; Chapin, J.K., Ceramic-based multisite electrode arrays for chronic single-neuron recording., *IEEE T. Bio-Med. Eng.* **2004**, *51*(4), 647–656.

[143] Neves, H.P.; Orban, G.A.; Koudelka-Hep, M.; Stieglitz, T.; Ruther, P., Development of modular multifunctional probe arrays for cerebral applications, *Proc. Int. Conf. Proc. IEEE Neural Eng.* **2007**, *1–2*, 104–109.

[144] Chen, Y.Y.; Kuo, T.S.; Jaw, F.S., A laser micromachined probe for recording multiple field potentials in the thalamus, *J. Neurosci. Methods* **2004**, *139*(1), 99–109.

[145] Cheung, K.C., Implantable Microscale Neural Interfaces, *Biomed. Microdevices* **2007**, *9*, 923–938.

[146] Cui, X.; Zhou, D., Poly (3,4-Ethylenedioxythiophene) for Chronic Neural Stimulation, *IEEE Trans. Neural Syst. Rehab. Eng.* **2007**, *15*(4), 502–508.

[147] Abidian, M.; Corey, J.; D, K.; D, M., Conducting-Polymer Nanotubes Improve Electrical Properties, Mechanical Adhesion, Neural Attachment, and Neurite Outgrowth of Neural Electrodes, *Small* **2010**, *6*(3), 421–429.

[148] Wilks, S.J.; Richardson-Burns, S.M.; Hendricks, J.L.; Martin, D.C.; Otto, K.J., Poly(3,4-ethylene dioxythiophene) (PEDOT) as a micro-neural interface material for electrostimulation, *Front.Neuroeng.* **2009**, *2*(7).

[149] Perlin, G.E.; Wise, K.D., The effect of the substrate on the extracellular neural activity recorded micromachined silicon microprobes, *Proc. Annu. Int. Conf. IEEE Eng. Med. Biol. Soc.* **2004**, 2002–5.

[150] Nam, Y.; Branch, D.W.; Wheeler, B.C., Epoxy-silane linking of biomolecules is simple and effective for patterning neuronal cultures, *Biosensors & Bioelectronics* **2006**, *22*(5), 589–597.

[151] Sanchez, G.; Dalchiele, E.; Bologna Alles, A., Electrical characterization of titanium nitride surfaces for pacing electrodes, *J. Mater. Sci.* **2006**, *41*(11), 3241–3247.

[152] Weiland, J.D.; Anderson, D.J.; Humayun, M.S., In vitro electrical properties for iridium oxide versus titanium nitride stimulating electrodes, *IEEE T. Bio-Med. Eng.* **2002**, *49*, 1574–1579.

[153] Ludwig, K.A.; Uram, J.D.; Yang, J.Y.; Martin, D.C.; Kipke, D.R., Chronic neural recordings using silicon microelectrode arrays electrochemically deposited with a poly(3,4-ethylenedioxythiophene) (PEDOT) film, *J. Neural Eng.* **2006**, *3*(1), 59–70.

[154] Venkatraman, S.; Hendricks, J.; S, R.B.; E, J.; D, M.; J, C., PEDOT coated Microelectrode Arrays for Chronic Neural Recording and Stimulation, *Proc. Annu. Int. Conf. IEEE Neural Eng.* **2009**, 376–379.

[155] Gabay, T.; Ben-David, M.; Kalifa, I.; Sorkin, R.; Abrams, Z.R.; Ben-Jacob, E.; Hanein, Y., Electro-chemical and biological properties of carbon nanotube based multi-electrode arrays, *Nanotechnology* **2007**, *18*(3), 1–6.

[156] Fung, A.O.; Tsiokos, C.; Paydar, O.; Chen, L.H.; Jin, S.; Wang, Y.; Judy, J.W., Electrochemical properties and myocyte interaction of carbon nanotube microelectrodes., *Nano Lett.* **2010**, *10*(11), 4321–4327.

[157] Brummer, S.B.; Turner, M.J., Electrochemical Considerations For Safe Electrical-Stimulation Of Nervous-System With Platinum-Electrodes, *IEEE T. Bio-Med. Eng.* **1977**, *24*(1), 59–63.

[158] Schmidt, E.M.; Bak, M.J.; Hambrecht, F.T.; Kufta, C.V.; O'Rourke, D.K.; Vallabhanath, P., Feasibility of a visual prosthesis for the blind based on intracortical microstimulation of the visual cortex., *Brain* **1996**, *119*, 507–522.

[159] McCreery, D.B.; Bullara, L.A.; Agnew, W.F., Neuronal activity evoked by chronically implanted intracortical microelectrodes., *Exp. Neurol.* **1986**, *92*(1), 147–161.

[160] Hambrecht, F.T., Visual Prostheses Based On Direct Interfaces With the Visual-system, *Baillieres Clinical Neurology* **1995**, *4*(1), 147–165.

[161] McCreery, D.B.; Yuen, T.G.; Agnew, W.F.; Bullara, L.A., A characterization of the effects on neuronal excitability due to prolonged microstimulation with chronically implanted microelectrodes., *IEEE T. Bio-Med. Eng.* **1997**, *44*(10), 931–939.

[162] Rousche, P.; Normann, R., Chronic intracortical microstimulation (ICMS) of cat sensory cortex using the Utah intracortical electrode array, *IEEE Trans. Neural Syst. Rehab. Eng.* **1999**, *7*(1), 56–68.

[163] McCreery, D.B.; Agnew, W.F.; Bullara, L.A., The effects of prolonged intracortical microstimulation on the excitability of pyramidal tract neurons in the cat., *Ann. Biomed. Eng.* **2002**, *30*(1), 107–119.

[164] McCreery, D.B.; Yuen, T.G.; Bullara, L.A., Chronic microstimulation in the feline ventral cochlear nucleus: physiologic and histologic effects., *Hear. Res.* **2000**, *149*(1-2), 223–238.

[165] Brummer, S.B.; Turner, M.J., Electrical Stimulation with Pt Electrodes: I. A Method for Determination of "Real" Electrode Areas, *IEEE T. Bio-Med. Eng.* **1977**, *24*(5), 436–439.

[166] Hung, A.; Zhou, D.; Greenberg, R.; Goldberg, I.B.; Judy, J.W., Pulse-clamp technique for characterizing neural-stimulating electrodes, *J. Electrochem. Soc.* **2007**, *154*(9), C479–C486.

[167] Zhou, D.; Greenberg, R., Electrochemical characterization of titanium nitride microelectrode arrays for charge-injection applications, *Proc. Annu. Int. Conf. IEEE Eng. Med. Biol. Soc.* **2003**, *2*, 1964–1967.

[168] Patan, M.; Shah, T.; Sahin, M., Charge injection capacity of TiN electrodes for an extended voltage range, *Proc. Annu. Int. Conf. IEEE Eng. Med. Biol. Soc.* **2006**, *1-15*, 5516–5518.

[169] Cogan, S.F.; Troyk, P.R.; Ehrlich, J.; Plante, T.D., In Vitro Comparison of the Charge-Injection Limits of Activated Iridium Oxide (AIROF) and Platinum-Iridium Microelectrodes, *IEEE T. Bio-Med. Eng.* **2005**, *52*, 1612–1614.

[170] Cogan, S.F.; Troyk, P.R.; Ehrlich, J.; Plante, T.D.; Detlefsen, D.E., Potential-biased, asymmetric waveforms for charge-injection with activated iridium oxide (AIROF) neural stimulation electrodes, *IEEE T. Bio-Med. Eng.* **2006**, *53*(2), 327–332.

[171] Cogan, S.F.; Ehrlich, J.; Plante, T.D.; Smirnov, A.; Shire, D.B.; Gingerich, M.; Rizzo, J.F., Sputtered Iridium Oxide Films for Neural Stimulation Electrodes, *J. Biomed. Mater. Res. B* **2009**, *89B*(2), 353–361.

[172] Beebe, X.; Rose, T., Charge injection limits of activated iridium oxide electrodes with 0.2 ms pulses in bicarbonate buffered saline (neurological stimulation application), *IEEE T. Bio-Med. Eng.* **1988**, *35*(6), 494–495.

[173] Minnikanti, S.; Pereira, M.G.A.G.; Jaraiedi, S.; Jackson, K.; Costa-Neto, C.M.; Li, Q.; Peixoto, N., In vivo electrochemical characterization and inflammatory response of multiwalled carbon nanotube-based electrodes in rat hippocampus, *J. Neural Eng.* **2010**, *7*(1), 016002.

[174] Weiland, J.; Anderson, D., Chronic neural stimulation with thin-film, iridium oxide electrodes, *IEEE T. Bio-Med. Eng.* **2000**, *47*, 911–918.

[175] Yamato, H.; Ohwa, M.; Wernet, W., Stability of Polypyrrole and Poly(3,4-ethylenedioxythiophene) For Biosensor Application, *J. Electroanal. Chem.* **1995**, *397*(1-2), 163–170.

[176] Green, R.A.; Williams, C.M.; Lovell, N.H.; Poole-Warren, L.A., Novel neural interface for implant electrodes: improving electroactivity of polypyrrole through MWNT incorporation., *J. Mater. Sci. Mater. Med.* **2008**, *19*(4), 1625–1629.

[177] Cott, D.; Chiodarelli, N.; Vereecken, P.M.; Vereecke, B.; Van Elshocht, S.; De Gendt, S., A CMOS Compatible Carbon Nanotube Growth Approach, *2010 MRS Fall Meeting* **2011**.

[178] Frackowiak, E.; Béguin, F., Electrochemical storage of energy in carbon nanotubes and nanostructured carbons, *Carbon* **2002**, *40*(10), 1775–1787.

[179] Lee, S.W.; Yabuuchi, N.; Gallant, B.M.; Chen, S.; Kim, B.S.; Hammond, P.T.; Shao-Horn, Y., High-power lithium batteries from functionalized carbon-nanotube electrodes, *Nat. Nanotechnol.* **2010**, *5*(7), 531–7.

[180] Najafi, K.; Hetke, J., Strength characterization of silicon microprobes in neurophysiological tissues, *IEEE T. Bio-Med. Eng.* **1990**, *37*(5), 474–481.

[181] Andrei, A.; Welkenhuysen, M.; Eberle, W.; Nuttin, B., Predictive experimental model of micromachined neural implants' in-vivo insertion behavior, *(submitted)* **2011**.

[182] Edell, D.J.; Toi, V.V.; McNeill, V.M.; Clark, L.D., Factors Influencing The Biocompatibility Of Insertable Silicon Microshafts In Cerebral-Cortex, *IEEE T. Bio-Med. Eng.* **1992**, *39*(6), 635–643.

[183] Jensen, W.; Yoshida, K.; Hofmann, U.G., In-vivo implant mechanics of flexible, silicon-based ACREO microelectrode arrays in rat cerebral cortex, *IEEE T. Bio-Med. Eng.* **2006**, *53*(5), 934–940.

[184] Szarowski, D.H.; Andersen, M.D.; Retterer, S.; Spence, A.J.; Isaacson, M.; Craighead, H.G.; Turner, J.N.; Shain, W., Brain responses to micro-machined silicon devices, *Brain Res.* **2003**, *983*, 23–35.

[185] Welkenhuysen, M.; Andrei, A.; Ameye, L.; Eberle, W.; Nuttin., B., Effect of insertion speed on tissue response and insertion mechanics of a chronical implanted silicon-based neural probe, *(submitted)* **2011**, –, –.

[186] Andrei, A., Disposable protection for high aspect ratio micro-engineered devices, Patent application No. 61/433847 filed for US Provision, **2011**.

[187] Gioanni, Y.; Lamarche, M., A Reappraisal Of Rat Motor Cortex Organization By Intracortical Microstimulation, *Brain Res.* **1985**, *344*(1), 49–61.

[188] Neuronexus - AXIALArray, `http://www.neuronexustech.com/Products/ResearchProducts/MicroelectrodeArray/ProbeDesigns/AXIALArray/AXIALModels/tabid/308/Default.aspx`.

[189] Logothetis, N.K.; Kayser, C.; Oeltermann, A., In Vivo Measurement of Cortical Impedance Spectrum in Monkeys: Implications for Signal Propagation, *Neuron* **2007**, *55*(5), 809–823.

[190] Ksienski, D., A minimum profile uniform current density electrode, *IEEE T. Bio-Med. Eng.* **1992**, *39*(7), 682–692.

[191] Kotov, N.; Winter, J.; Clements, I.; Jan, E.; Timko, B.; Campidelli, S., Nanomaterials for Neural Interfaces, *Adv. Mat.* **2009**, *21*(40), 3970–4004.

[192] Yamanaka, K., Anodically Electrodeposited Iridium Oxide-films (AEIROF) From Alkaline-solutions For Electrochromic Display Devices, *Jap. J. Appl. Phys.* **1989**, *28*(4), 632–637.

[193] Rand, D.R.; Musa, S.; Eberle, W., Glutamate oxidase immobilization on electrodeposited iridium oxide electrodes for the detection of glutamate in vitro, *(submitted)* **2011**, –, –.

[194] Roscoe, S.G.; Fuller, K.L., Fouling of model surfaces: adsorption and removal of whole unpasteurized milk, *Food Res. Int.* **1994**, *27*(4), 363–369.

[195] Rouhana, R.; Budge, S.M.; MacDonald, S.M.; Roscoe, S.G., Electrochemical studies of the interfacial behaviour of alpha-lactalbumin and bovine serum albumin, *Food Res. Int.* **1997**, *30*(1), 13–20.

[196] Roscoe, S.G., In Situ FTIR Studies of an Oxidation Product from Protein Adsorption at the Platinum Electrode, *J. Coll. Interf. Sci.* **2000**, *228*(2), 438–440.

[197] Hibbert, D.B.; Weitzner, K.; Carter, P., Voltammetry of platinum in artificial perilymph solution, *J. Electrochem. Soc.* **2001**, *148*(1), E1–E7.

[198] Cosman, N.P.; Roscoe, S.G., Electrochemical Quartz Crystal Nanobalance (EQCN) Studies of Protein Interfacial Behavior at Pt, *Langmuir* **2004**, *20*(5), 1711–1720.

[199] Farcas, M.; Cosman, N.P.; Ting, D.K.; Roscoe, S.G.; Omanovic, S., A comparative study of electrochemical techniques in investigating the adsorption behaviour of fibrinogen on platinum, *J. Electroanal. Chem.* **2010**, *649*(1-2), 206–218.

[200] Robblee, L.; McHardy, J.; Marston, J.; Brummer, S., Electrical stimulation with Pt electrodes. V. The effect of protein on Pt dissolution, *Biomaterials* **1980**, *1*(3), 135 – 139.

[201] Peters, T., Serum-albumin, *Adv. Protein Chem.* **1985**, *37*, 161–245.

[202] Thompson, E., *Proteins of the Cerebrospinal Fluid: Analysis and Interpretation in the Diagnosis and Treatment of Neurological Deiseases*, Elsevier Academic Press, San Diego, 2 edition, **2005**.

[203] PhosphoSite - beta trace, `http://www.phosphosite.org/proteinAction.do?id=14460&showAllSites=true`.

[204] MedlinePlus Encyclopedia - Albumin, `http://www.nlm.nih.gov/medlineplus/ency/article/003480.htm`.

[205] MedlinePlus Encyclopedia - IgG, `http://www.nlm.nih.gov/medlineplus/ency/article/003544.htm`.

[206] O'Keefe Jr, J.H.; Cordain, L.; Harris, W.H.; Moe, R.M.; Vogel, R., Optimal low-density lipoprotein is 50 to 70 mg/dl: Lower is better and physiologically normal, *J. Am. Coll. Cardiology* **2004**, *43*(11), 2142–2146.

[207] Rifai, N.; Warnick, G.R.; McNamara, J.R.; Belcher, J.D.; Grinstead, G.F.; Frantz, I.D., Measurement of low-density-lipoprotein cholesterol in serum: a status report., *Clin. Chem.* **1992**, *38*(1), 150–160.

[208] Takehara, K.; Ide, Y.; Nakazato, T.; Yoza, N., On the assignment of the redox peaks observed in phosphate and phosphite solutions at a Pt electrode, *J. Electroanal. Chem.* **1990**, *293*(1-2), 285 – 290.

[209] Hudak, E.M.; Mortimer, J.T.; Martin, H.B., Platinum for neural stimulation: voltammetry considerations, *J. Neural Eng.* **2010**, *7*(2), 026005–026010.

[210] Breiter, M.W.; Weininger, J.L., Dissolution of Oxygen Layers on Platinum in Chloride Solutions, *J. Electrochem. Soc.* **1962**, *109*(12), 1135–1138.

[211] Gilman, S., Studies of Anion Adsorption on Platinum by the Multipulse Potentiodynamic (M.p.p.) Method. I. Kinetics of Chloride and Phosphate Adsorption and Associated Charge at Constant Potential1, *J. Phys. Chem.* **1964**, *68*(8), 2098–2111.

[212] Conway, B.E.; Mozota, J., Chloride-ion effects on the reversible and irreversible surface oxidation processes at Pt electrodes, and on the growth of monolayer oxide films at Pt, *J. Chem. Soc., Faraday Trans. 1* **1982**, *78*(6), 1717–1732.

[213] Milosev, I.; Strehblow, H..H.; Navinsek, B.; Metikos-Hukovic, M., Electrochemical and thermal oxidation of TiN coatings studied by XPS, *Surf. Interface Anal.* **1995**, *23*, 529–39.

[214] Birss, V.; Bock, C.; Elzanowska, H., Hydrous Ir oxide films: the mechanism of the anodic prepeak reaction, *Can. J. Chem.* **1997**, *75*(11), 1687–1693.

[215] Juodkazyte, J.; Scaronebeka, B.; Valsiunas, I.; Juodkazis, K., Iridium Anodic Oxidation to Ir(III) and Ir(IV) Hydrous Oxides, *Electroanalysis* **2005**, *17*(11), 947–952.

[216] Petit, M.A.; Plichon, V., Anodic electrodeposition of iridium oxide films, *J. Electroanal. Chem.* **1998**, *444*(2), 247–252.

[217] Granqvist, C.G., *Handbook of inorganic electrochromic materials.*, Elsevier, Amsterdam, **2002**.

[218] Gottesfeld, S.; McIntyre, J.D.E., Electrochromism In Anodic Iridium Oxide-films .2. Ph Effects On Corrosion Stability and the Mechanism of Coloration and Bleaching, *J. Electrochem. Soc.* **1979**, *126*(5), 742–750.

[219] Conway, B.E., Transition from "Supercapacitor" to "Battery" Behavior in Electrochemical Energy Storage, *J. Electrochem. Soc.* **1991**, *138*(6), 1539–1548.

[220] Glarum, S.H.; Marshall, J.H., The A-C Response of Iridium Oxide Films, *J. Electrochem. Soc.* **1980**, *127*(7), 1467–1474.

[221] Hackwood, S.; Dautremont-Smith, W.C.; Beni, G.; Schiavone, L.M.; Shay, J.L., Volume Changes Induced By the Electrochromic Process In Sputtered Iridium Oxide-films, *J. Electrochem. Soc.* **1981**, *128*(6), 1212–1214.

[222] Vukovic, M., Voltammetric and galvanostatic studies of hydrous and anhydrous iridium oxide films, *J. Appl. Electrochem.* **1990**, *20*(6), 969–973.

[223] Yamanaka, K., The Electrochemical-behavior of Anodically Electrodeposited Iridium Oxide-films and the Reliability of Transmittance Variable Cells, *Jap. J. Appl. Phys.* **1991**, *30*(6), 1285–1289.

[224] Barisci, J.N.; Wallace, G.G.; Baughman, R.H., Electrochemical Characterization of Single-Walled Carbon Nanotube Electrodes, *J. Electrochem. Soc.* **2000**, *147*(12), 4580–4583.

[225] Frackowiak, E.; Béguin, F., Carbon materials for the electrochemical storage of energy in capacitors, *Carbon* **2001**, *39*(6), 937–950.

[226] Ndubuizu, O., Brain tissue oxygen concentration measurements, *Antioxidants & redox signaling* **2007**, *9*(8), 1207–1219.

[227] West, A.; Newman, J., Current distribution on recessed electrodes, *J. Electrochem. Soc.* **1991**, *138*(6), 1620–1625.

[228] Cole, K.S.; Cole, R.H., Dispersion and Absorption in Dielectrics I. Alternating Current Characteristics, *J. Chem. Phys.* **1941**, *9*(4), 341–351.

[229] Barsoukov, E.; Macdonald, J.R., eds., *Impedance Spectroscopy*, Wiley, New Jersey, 2nd edition, **2005**.

[230] Randles, J.E.B., Kinetics of rapid electrode reactions, *Discuss. Farad. Soc.* **1947**, *1*, 11–19.

[231] Warburg, E., Über das Verhalten sogenannter unpolarisirbarer Elektroden gegen Wechselstrom, *Ann. Phys.* **1899**, *76*, 493–499.

[232] Conway, B.; Gileadi, E., Kinetic theory of pseudo-capacitance and electrode reactions at appreciable surface coverage, *Tran. Farad. Soc.* **1962**, *58*(DEC), 2493–2509.

[233] Jackson, D.R.; Omanovic, S.; Roscoe, S.G., Electrochemical Studies of the Adsorption Behavior of Serum Proteins on Titanium, *Langmuir* **2000**, *16*(12), 5449–5457.

[234] Lasia, A., Modeling of impedance of porous electrodes, in M. Schlesinger, ed., *Modern Aspects of Electrochemistry*, Springer, volume 43, chapter 3, **2009**.

[235] McCreery, R.L., Advanced carbon electrode materials for molecular electrochemistry., *Chem Rev* **2008**, *108*(7), 2646–2687.

[236] Jacobs, C.B.; Vickrey, T.L.; Venton, B.J., Functional groups modulate the sensitivity and electron transfer kinetics of neurochemicals at carbon nanotube modified microelectrodes, *Analyst* **2011**, 3557–3565.

[237] Michael, A.C.; Borland, L.M., eds., *An Introduction to Electrochemical Methods in Neuroscience*, CRC Press, Boca Raton, **2007**.

[238] Swamy, B.E.K.; Venton, B.J., Carbon nanotube-modified microelectrodes for simultaneous detection of dopamine and serotonin in vivo, *Analyst* **2007**, *132*(9), 876–884.

[239] Whalen, J.J.; Young, J.; Weiland, J.D.; Searson, P.C., Electrochemical characterization of charge injection at electrodeposited platinum electrodes in phosphate buffered saline, *J. Electrochem. Soc.* **2006**, *153*(12), C834–C839.

[240] Cogan, S.F.; Troyk, P.R.; Ehrlich, J.; Gasbarro, C.M.; Plante, T.D., The influence of electrolyte composition on the in vitro charge-injection limits of activated iridium oxide (AIROF) stimulation electrodes, *J. Neural Eng.* **2007**, *4*(2), 79–86.

[241] Bonner, M.; Mortimer, J., The Pulse-Clamp method for analyzing neural stimulating electrodes, *Ann. Biomed. Eng.* **1992**, *20*(1), 143–144.

[242] Stefan, I.C.; Tolmachev, Y.V.; Nagy, Z.; Minkoff, M.; Merrill, D.R.; Mortimer, J.T.; Scherson, D.A., Theoretical Analysis of the Pulse-Clamp Method as Applied to Neural Stimulating Electrodes, *J. Electrochem. Soc.* **2001**, *148*, E73–E78.

[243] Merrill, D.R.; Stefan, I.C.; Scherson, D.A.; Mortimer, J.T., Electrochemistry of Gold in Aqueous Sulfuric Acid Solutions under Neural Stimulation Conditions, *J. Electrochem. Soc.* **2005**, *152*(7), E212–E221.

[244] MacDonald, D.D., *Transient Techniques in Electrochemistry*, Plenum Press, New York, **1977**.

[245] Sand, H.J.S., On the concentration at the electrodes in a solution, with special reference to the liberation of hydrogen by electrolysis of a mixture of copper sulphate and sulphuric acid., *Phil. Mag.* **1901**, *1*, 45–79.

[246] Davis, D.D., Application of chronopotentiometry to problems in analytical chemistry, in A.J. Bard, ed., *Electroanalytical chemistry*, Marcel Dekker, New York, volume 1, **1966**.

[247] Abrantes, L.M.; González, J.; Molina, A.; Saavedra, F., Application of cyclic reciprocal derivative chronopotentiometry with programmed currents to the study of the reversibility of electrode processes, *Electrochim. Acta* **1999**, *45*(3), 457 – 468.

[248] Molina, A.; González, J.; Saavedra, F.; Abrantes, L.M., Cyclic reciprocal derivative chronopotentiometry. Applications to the detection and characterisation of adsorption processes, *Electrochim. Acta* **1999**, *45*(4-5), 761–773.

[249] Wang, J.; Tian, B., Chronopotentiometric Analysis of Highly Resistive Media, *Anal. Chem.* **2000**, *72*(14), 3241–3244.

[250] Kizek, R.; Trnkova, L.; Palecek, E., Determination of metallothionein at the femtomole level by constant current stripping chronopotentiometry, *Anal. Chem.* **2001**, *73*(20), 4801–4807.

[251] Molina, A.; Gonzalez, J.; Morales, I., Steady state reciprocal derivative chronopotentiometry with programmed currents at microelectrodes, *Electroanalysis* **2005**, *17*(8), 674–684.

[252] Molina, A.; González, J.; Abenza, N., Application of chronopotentiometry and derivative chronopotentiometry with an alternating current to the study of a slow charge transfer in a surface confined redox system, *Electrochim. Acta* **2006**, *51*(21), 4358–4366.

[253] Chen, L.; Wang, Z.; Chen, J.; Bi, S., Theoretical investigation on cyclic reciprocal derivative chronopotentiometry: Kinetic study of totally irreversible electrode processes, *Electrochim. Acta* **2007**, *52*(28), 8020–8030.

[254] Chen, L.; Wang, Z.; Chen, J.; Yang, C.; Wang, Y.; Bi, S., Theoretical study of irreversible electrode reactions with Henry adsorption using symmetrical cyclic reciprocal derivative chronopotentiometry, *Electrochim. Acta* **2009**, *54*(23), 5326 – 5335.

[255] Bi, S.; Yu, J., Investigations on cyclic reciprocal derivative chronopotentiometry. Part 1. Theory for a reversible reaction, *J. Electroanal. Chem.* **1996**, *405*(1-2), 51–58.

[256] Hibbert, D.B.; Weitzner, K.; Tabor, B.; Carter, P., Mass changes and dissolution of platinum during electrical stimulation in artificial perilymph solution, *Biomaterials* **2000**, *21*(21), 2177–2182.

[257] Musa, S.; Rand, D.R.; Bartic, C.; Eberle, W.; Nuttin, B.; Borghs, G., Coulometric detection of irreversible electrochemical reactions occurring at Pt microelectrodes used for neural stimulation., *Anal Chem* **2011**, *83*(11), 4012–4022.

[258] Biesheuvel, P.M.; Bazant, M.Z., Nonlinear dynamics of capacitive charging and desalination by porous electrodes, *Phys. Rev. E* **2010**, *81*(3).

[259] Drake, K.L.; Wise, K.D.; Farraye, J.; Anderson, D.J.; Bements, S.L., Performance Of Planar Multisite Microprobes In Recording Extracellular Single-Unit Intracortical Activity, *IEEE T. Bio-Med. Eng.* **1988**, *35*(9), 719–732.

[260] McNaughton, B.L.; O'Keefe, J.; Barnes, C.A., The stereotrode: A new technique for simultaneous isolation of several single units in the central nervous system from multiple unit records, *J. Neurosci. Methods* **1983**, *8*(4), 391–397.

[261] Henze, D.A.; Borhegyi, Z.; Csicsvari, J.; Mamiya, A.; Harris, K.D.; Buzsaki, G., Intracellular features predicted by extracellular recordings in the hippocampus in vivo, *J. Neurophysiol.* **2000**, *84*(1), 390–400.

[262] Hattox, A.M.; Priest, C.A.; Keller, A., Functional circuitry involved in the regulation of whisker movements, *J. Comp. Neurol.* **2002**, *442*(3), 266–276.

[263] Trojniar, W.; Klejbor, I., Facilitatory effect of unilateral lesion of the ventral tegmental area on locomotor response to stimulation of the contralateral ventral tegmental area: involvement of GABAergic transmission, *Brain Res.* **1999**, *842*(2), 419–430.

[264] Welkenhuysen, M., *Electrical brain stimulation and microrecording: Research in animal models for psychiatric disorders and in vivo evaluation of a neural probe*, Ph.D. thesis, KU Leuven, **2011**.

[265] Paxinos, G.; Watson, C., *The rat brain in stereotactic coordinates.*, Academic Press, San Diego, **2005**.

[266] Mora López, C.; Musa, S.; Bartic, C.; Puers, R.; Gielen, G.; ; Eberle, W., Systematic Design of a Programmable Low-Noise CMOS Neural Interface for Cell Activity Recording, *Proc. Europ. Conf. DATE* **2011**.

[267] Rutishauser, U.; Schuman, E.M.; Mamelak, A.N., Online detection and sorting of extracellularly recorded action potentials in human medial temporal lobe recordings, in vivo, *J. Neurosci. Methods* **2006**, *154*(1-2), 204–224.

[268] Gligorijevic, I.; Welkenhuysen, M.; Prodanov, D.; Musa, S.; Nuttin, B.; Eberle, W.; Bartic, C.; Van Huffel, S., Neural signal analysis and artifact removal in single and multichannel invivo deep brain recordings., *Proc. IEEE EMBS Benelux* **2009**.

[269] McCreery, D.B.; Agnew, W.F.; Yuen, T.G.H.; Bullara, L., Charge-Density And Charge Per Phase As Cofactors In Neural Injury Induced By Electrical-Stimulation, *IEEE T. Bio-Med. Eng.* **1990**, *37*, 996–1001.

[270] Lassen, B.; Malmsten, M., Structure of Protein Layers during Competitive Adsorption, *J. Colloid Interface Sci.* **1996**, *180*(2), 339–349.

[271] Gong, P.; Szleifer, I., Competitive adsorption of model charged proteins: the effect of total charge and charge distribution, *J. Colloid Interface Sci.* **2004**, *278*(1), 81–90.

[272] Johnson, M.D.; Otto, K.J.; Kipke, D.R., Repeated voltage biasing improves unit recordings by reducing resistive tissue impedances, *IEEE T. Neur. Sys. Reh.* **2005**, *13*(2), 160–165.

[273] Butson, C.R.; McIntyre, C.C., Tissue and electrode capacitance reduce neural activation volumes during deep brain stimulation, *Clin. Neurophysiol.* **2005**, *116*, 2490–2500.

[274] Williams, J.C.; Hippensteel, J.A.; Dilgen, J.; Shain, W.; Kipke, D.R., Complex impedance spectroscopy for monitoring tissue responses to inserted neural implants, *J. Neural Eng.* **2007**, *4*, 410–423.

[275] Moulton, S.E.; Barisci, J.N.; Bath, A.; Stella, R.; Wallace, G.G., Investigation of Ig.G Adsorption and the Effect on Electrochemical Responses at Titanium Dioxide Electrode, *Langmuir* **2005**, *21*(1), 316–322.

[276] Latikka, J.; Kuurne, T.; Eskola, H., Conductivity of living intracranial tissues, *Phys. Med. Biol.* **2001**, *46*(6), 1611–1616.

[277] Nguyen, T.; Braeken, D.; Musa, S.; Krylychkina, O.; Bartic, C.; Gielen, G.; Eberle, W., Towards a closed-loop system for stimulation and recording: An in vitro approach with embryonic cardiomyocytes, *Proc. Annu. Int. Conf. IEEE Eng. Med. Biol. Soc.* **2010**, 2735–2738.

[278] Hu, H.; Ni, Y.C.; Montana, V.; Haddon, R.C.; Parpura, V., Chemically functionalized carbon nanotubes as substrates for neuronal growth, *Nano Lett.* **2004**, *4*(3), 507–511.

[279] Yang, K.; Zhu, L.; Xing, B., Adsorption of Polycyclic Aromatic Hydrocarbons by Carbon Nanomaterials, *Environ. Sci. Technol.* **2006**, *40*(6), 1855–1861.

[280] Pan, B.; Xing, B.S., Adsorption Mechanisms of Organic Chemicals on Carbon Nanotubes, *Environ. Sci. Technol.* **2008**, *42*(24), 9005–9013.

[281] Lin, Y.; Watson, K.A.; Fallbach, M.J.; Ghose, S.; Smith, J.G.; Delozier, D.M.; Cao, W.; Crooks, R.E.; Connell, J.W., Rapid, Solventless, Bulk Preparation of Metal Nanoparticle-Decorated Carbon Nanotubes, *ACS Nano* **2009**, *3*(4), 871–884.

[282] Magrez, A.; Kasas, S.; Salicio, V.; Pasquier, N.; Seo, J.W.; Celio, M.; Catsicas, S.; Schwaller, B.; Forró, L., Cellular Toxicity of Carbon-Based Nanomaterials, *Nano Lett.* **2006**, *6*(6), 1121–1125.

[283] Nguyen-Vu, T.D.B.; Chen, H.; Cassell, A.M.; Andrews, R.J.; Meyyappan, M.; Li, J., Vertically aligned carbon nanofiber architecture as a multifunctional 3-D neural electrical interface, *IEEE T. Bio-Med. Eng.* **2007**, *54*(6), 1121–1128.

[284] Morrell, M.J.; Investigators, R.S.P., Results of a multicenter double blinded randomized controlled pivotal investigation of the RNS angle system for treatment of intractable partial epilepsy in adults, *Epilepsia* **2009**, *50*, 490–490.

[285] Polikov, V.S.; Tresco, P.A.; Reichert, W.M., Response of brain tissue to chronically implanted neural electrodes, *J. Neurosci. Meth.* **2005**, *148*, 1–18.

[286] Biran, R.; Martin, D.C.; Tresco, P.A., Neuronal cell loss accompanies the brain tissue response to chronically implanted silicon microelectrode arrays, *Exp. Neurol.* **2005**, *195*(1), 115–126.

[287] Williams, J.C.; Holecko, M.M.; Massia, S.P.; Rousche, P.; Kipke, D.R., Multi-site incorporation of bioactive matrices into MEMS-based neural probes., *J. Neural Eng.* **2005**, *2*(4), L23–L28.

[288] Purcell, E.K.; Seymour, J.P.; Yandamuri, S.; Kipke, D.R., In vivo evaluation of a neural stem cell-seeded prosthesis., *J. Neural Eng.* **2009**, *6*(2), 026005–026014.

[289] Li, P.; Lim, X.; Zhu, Y.; Yu, T.; Ong, C.K.; Shen, Z.; Wee, A.T.S.; Sow, C.H., Tailoring wettability change on aligned and patterned carbon nanotube films for selective assembly., *J. Phys. Chem. B* **2007**, *111*(7), 1672–1678.

[290] Moon, J.S.; Alegaonkar, P.S.; Han, J.H.; Lee, T.Y.; Yoo, J.B.; Kim, J.M., Enhanced field emission properties of thin-multiwalled carbon nanotubes: Role of SiOx coating, *J. Appl. Phys.* **2006**, *100*(10), 104303–1–104303–7.

[291] Kim, U.J.; Liu, X.M.; Furtado, C.A.; Chen, G.; Saito, R.; Jiang, J.; Dresselhaus, M.S.; Eklund, P.C., Infrared-Active Vibrational Modes of Single-Walled Carbon Nanotubes, *Phys. Rev. Lett.* **2005**, *95*(15), 157402–4.

[292] Socrates, G., *Infrared and Raman Characteristic Group Frequencies*, Wiley, Chichester, **2001**.

[293] Kim, U.J.; Furtado, C.A.; Liu, X.; Chen, G.; Eklund, P.C., Raman and IR Spectroscopy of Chemically Processed Single-Walled Carbon Nanotubes, *J. Am. Chem. Soc.* **2005**, *127*(44), 15437–15445.

[294] Liu, M.; Yang, Y.; Zhu, T.; Liu, Z., Chemical modification of single-walled carbon nanotubes with peroxytrifluoroacetic acid, *Carbon* **2005**, *43*(7), 1470–1478.

[295] Liu, H.; Li, S.H.; Zhai, J.; Li, H.J.; Zheng, Q.S.; Jiang, L.; Zhu, D.B., Self-assembly of large-scale micropatterns on aligned carbon nanotube films, *Angew. Chem. - Int. Ed.* **2004**, *43*, 1146–1149.

[296] Memming, R., *Semiconductor Electrochemistry*, Wiley-VCH, Weinheim, **2001**.

[297] Silva, T.; Simões, A.; Ferreira, M.; Walls, M.; Da Cunha Belo, M., Electronic structure of iridium oxide films formed in neutral phosphate buffer solution, *J. Electroanal. Chem.* **1998**, *441*(1-2), 5–12.

[298] Mailley, S.C.; Hyland, M.; Mailley, P.; McLaughlin, J.M.; McAdams, E.T., Electrochemical and structural characterizations of electrodeposited iridium oxide thin-film electrodes applied to neuro stimulating electrical signal, *Mat. Sci. Eng. C* **2002**, *21*(1-2), 167–175.

[299] Lervik, I.A.; Tsypkin, M.; Owe, L.E.; Sunde, S., Electronic structure vs. electrocatalytic activity of iridium oxide, *J. Electroanal. Chem.* **2010**, *645*(2), 135–142.

[300] Schuettler, M.; Franke, M.; Krueger, T.B.; Stieglitz, T., A voltage-controlled current source with regulated electrode bias-voltage for safe neural stimulation., *J. Neurosci. Methods* **2008**, *171*(2), 248–252.

Short CV

Silke Musa received her Diploma degree in Applied Natural Science in 2006 from the Technical University of Freiberg, Germany. In February 2007, she started her Ph.D. at the Katholieke Universiteit Leuven in the Department of Physics and Astronomy in collaboration with imec (Belgium) on the the design, fabrication, and characterization of a neural probe for deep brain stimulation and recording. Her research interests include the development of microelectronic devices for life science and biomedical applications and electroanalytical techniques for the characterization of functional materials.

Arenberg Doctoral School of Science, Engineering & Technology
Faculty of Science
Department of Physics and Astronomy
Semiconductor Physics
Kasteelpark Arenberg 11 box 2100
B-3001 Leuven